NASA-CR-191711

SEMI-ANNUAL PROGRESS REPORT

P. 103

Period: January-June 1992

"The Effects of Cloud Inhomogeneities Upon Radiative Fluxes, and the Supply of a Cloud Truth Validation Dataset"

Submitted by

Institute of Atmospheric Sciences
South Dakota School of Mines and Technology
501 E. St. Joseph Street
Rapid City, SD 57701-3995

to

National Aeronautics and Space Administration
Goddard Space Flight Center
Contract NAS5-31718
Greenbelt, MD 20771

(NASA-CR-191711) THE EFFECTS OF CLOUD INHOMOGENEITIES UPON RADIATIVE FLUXES, AND THE SUPPLY OF A CLOUD TRUTH VALIDATION DATASET Semiannual Progress Report, 1 Jul. - 31 Dec. 1992 (South Dakota School of Mines and Technology) 103 p

N93-26492

Unclas

G3/47 0167870

Comparison Of Airborne Visible Infrared Imaging Spectrometer (AVIRIS) and Thermal Infrared Imaging Spectrometer (TIMS) Cloud Pixel Identification and the Effect of Spatial Resolution on TIMS Cloud Area Retrievals

1. Introduction

In this study, 50 m resolution TIMS imagery is registered to 20 m resolution AVIRIS imagery. The registration is accomplished first by applying panoramic corrections to both data sources, followed by the application of 2-D and 1-D cross correlations, to determine optimum resampling values and relative displacement between the imagery. Then cloud pixel identification is compared between temperature thresholded TIMS imagery and AVIRIS imagery masked by the 3-band ratio (3BR) (Gao and Goetz, 1990) technique. The optimum temperature threshold for the TIMS imagery is established based on retrieved cloud area from AVIRIS. The sensitivity of retrieved cloud area to temperature threshold is also investigated. In addition, cloud edge masks, obtained from the 3BR technique, are overlayed on the TIMS imagery to determine the temperature distribution of cloud edges. TIMS imagery is then spatially degraded progressively from 50 m to 1000 m and changes in estimates of cloud area as a function of threshold are investigated.

2. Methodology

Although the AVIRIS and TIMS were mounted in the same aircraft and collected data simultaneously, registering the imagery between the two systems cannot be accomplished through simple box averaging. The registration problem is more complex for several reasons:

(1) The nominal angular resolution of these instruments (i.e., 1 mrad for AVIRIS and 2.5 mrad for TIMS) is not necessarily the angular spacing of the image pixels. These instruments are designed to be overscanned in both the across-track and along-track directions. The across-track overscan is determined by the scanning optics while the along-track overscan is determined by the flight altitude, flight velocity, and instrument scan rate.

(2) The panoramic distortion, although minor in the AVIRIS imagery, is significant in the TIMS imagery. For example, pixels obtained at the maximum off-nadir directions can have ground instantaneous field-of-views (GIFOVs) of 102 m.

(3) Although these instruments were mounted on the same platform and collected data simultaneously, roll deviations of the ER-2 (from 0 degrees) caused the TIMS GIFOV to decrease/increase at a rate greater than that for

the AVIRIS. This resulted in relative motion of the image edge of one data source with respect to another.

(4) Although every effort was made during preflight operations to boresight the nadir view of TIMS to that of AVIRIS, the angular displacement was significant and in one scene was approximately 10°, resulting in a 3500 m displacement on the ground.

Of course, there are other potential sources of errors in the registration process, such as instrument system and signal noise, air vehicle pitch, altitude, and velocity variations, numerical and algorithmic errors, along track panoramic distortion, etc. However, the problems cited above are assumed to be the most significant and are the ones addressed in this study.

The registration methodology is basically a 5-step process and is summarized as follows:

(1) The first step in registering the AVIRIS and TIMS imagery is to extract the TIMS data that corresponds to the available AVIRIS data. The area imaged by AVIRIS only represents a small subset of the available TIMS data, both in width and length. The extracted image is larger than ultimately necessary, as subsequent steps are required to obtain the final, smaller image.

(2) Next, the AVIRIS and TIMS imagery are resampled for across-track panoramic distortion. Each type of imagery must be represented by uniformly spaced pixels (on the ground) to accomplish registration.

(3) The AVIRIS imagery is then spatially degraded to approximate the spatial resolution or IFOV of the TIMS (i.e., from 1 mrad to 2.5 mrad). Based on TIMS and AVIRIS system specifications, the AVIRIS data is then resampled to obtain an approximate TIMS equivalent image.

(4) Next, by way of an iterative process utilizing 2-D cross correlation, an optimum resampling of the TIMS imagery is determined, as well as the location of the subimage in the extracted image that best matches the resampled AVIRIS image. This process attempts to compensate for some of the undetermined sources of error mentioned above.

(5) Finally, 1-D line cross correlation between the TIMS and AVIRIS imagery is used to compensate for the roll deviations of the air vehicle platform.

The simulation of lower spatial resolution thermal sensors is performed through convolution. A set of convolution masks is generated, each of which has a width that is an integer multiple of the original image. Each mask then corresponds to the Point Spread Function (PSF) of each lower spatial resolution being simulated. For this study, ten masks are generated for simulating spatial resolutions at multiples of 2,4,6, ... ,18,20 of the original registered and resampled TIMS image. This corresponds roughly to spatial resolutions of 100, 200, 300, ... ,900, 1000 m. Each of these masks are then convolved with the original image, resulting in an image that is analogous to that imaged by the optics of a lower spatial resolution instrument. The spatially degraded images are then temperature thresholded, and cloud area is determined. As spatial resolution is degraded (or decreased), both the texture and edges of the clouds become smoother.

3. Results

3.1 Comparison of AVIRIS and TIMS Cloud Pixel Identification

After all seven TIMS images are registered to the corresponding AVIRIS images a pixel-by-pixel comparison between the thresholded TIMS imagery and the masked 0.74 μm AVIRIS image is performed. Table 1 summarizes the comparison. "Type 1" differences are those cloud pixels identified as cloud by the 3BR method and as not-cloud by thresholding of the TIMS imagery. "Type 2" differences are those cloud pixels identified as not-cloud by the 3BR method and as cloud by thresholding of the TIMS imagery. The "A" differences occur over non-shadowed background areas while "B" differences occur over shadowed background areas.

As can be seen in Table 1, for all seven scenes, the percent of "A" pixels with respect to total number of "Type 1" differences is greater than 50 percent, and on the average is 74 percent. However the "Type 2" differences are inconsistent. The results in Table 1 indicate that in three scenes, more differences are found over shadowed areas (B), and in the other four scenes, more differences are found over non-shadowed areas (A).

When examining the last column of Table 1, these results suggest that, given an optimum temperature threshold (based on the cloud area as determined by the 3BR method applied to AVIRIS imagery), thresholding of thermal imagery over continental backgrounds can produce accurate cloud pixel identification. The differences between the two methods are only 5-8

TABLE 1

Summary of Results Obtained in TIMS-AVIRIS
Cloud Pixel Identification

	DIFFERENCES				
	% of Total Type 1		% of Total Type 2		% of Total Cloud Area
Scene 1	A	B	A	B	
A	71	29	29	71	5.7
B	61	39	68	32	7.9
C	70	30	52	48	8.5
D	84	16	73	27	5.5
E	78	22	39	61	6.2
F	70	30	50	50	5.5
M	86	14	11	89	8.5
Mean	74	26	46	54	6.8

Note: Type 1 differences are regions in which 3BR identified cloud pixels and TIMS did not. Conversely, Type 2 differences are regions in which TIMS identified cloud pixels and 3BR did not. "A" differences occurred over non-shadowed background areas. "B" differences occurred over shadowed background areas.

percent, and it is certainly possible that at least half of those differences are due to deficiencies in the registration methodology.

3.2 Distribution of Cloud Edge Temperatures

The cloud edge corresponding to the 3BR mask is extracted using a morphological erosion operator. In addition, the edge just beyond the 3BR mask is extracted. This edge corresponds to the background region closest to the cloud edge. The histogram of temperatures for the two edges is depicted for all seven scenes in Fig. 1. The histogram appearing slightly to the left corresponds to the distribution of the 3BR cloud edge, and the one to the right corresponds to the distribution of background pixels close to the cloud edge. Several temperatures of interest are also indicated by vertical lines. They are: the threshold temperature as determined by the 3BR cloud mask; the peak background temperature; and the peak background temperature minus 1, 2, 3, and 4 degrees. Several observations can be made. First, the location (temperature) of the peak in the histograms for cloud

edges is inconsistent among all seven scenes, indicating that the optimum threshold temperature is scene dependent. Note that this imagery is obtained from the same geographical area on the same day. Second, in all seven scenes, the distribution of temperatures in the cloud edge is very broad, indicating that the optimum cloud temperature threshold within a given scene is not a singular value. This is further corroborated by the fact that the distribution of cloud edges significantly overlaps that of the background pixels close to the cloud edge. Third, the 3BR temperature threshold best coincides with the peak in the histogram, which is expected since the temperature threshold is determined indirectly by the 3BR method. Fourth, the background temperatures minus 2°C and 3°C are the closest to coinciding with the peak in the histogram. For this set of scenes, these results indicate that a threshold of background temperature minus 2-3°C provides for the most accurate cloud identification. However, these results may not be applicable to other scenes, as this set of seven scenes has fairly uniform background temperatures. Potentially, very different results may be obtained for less uniform temperature backgrounds. This will be explored in future investigations as additional data become available.

3.3 Spatial Degradation of TIMS Imagery vs. Cloud Area

All seven TIMS scenes are spatially degraded and cloud area is determined. The cloud area versus spatial resolution results are shown in Fig. 2. Except for Scenes B and M, cloud area increases monotonically with decreasing spatial resolution. The inconsistency of Scenes B and M are difficult to explain. Scene B initially increases in cloud area but begins to decrease at 500 m and ends with virtually no increase in area at 1000 m spatial resolution. Scene M decreases monotonically in cloud area across the entire range of spatial resolutions. One obvious difference between Scenes B and M, and the other five, is that the cloud fraction and cloud size are much smaller indicating that, for any cloud size, when progressively degrading spatial resolution, there is some resolution at which retrieved cloud area begins to decrease instead of increase

3.4 Cloud Area vs. Threshold Temperature

Cloud area is estimated using four other thresholds (other than the 3BR temperature threshold) for each of ten spatial resolutions and for all seven TIMS scenes. Those threshold temperatures are background temperature minus 1, 2, 3, and 4 degrees. The results for all seven scenes are shown in Fig. 3. They are expressed as the percent change from the cloud area as determined by the 3BR temperature threshold in the original registered 50 m spatial resolution TIMS image. It can be seen in Fig. 3 that there are large differences in the best estimate of cloud area and estimates

obtained at other thresholds and/or lower spatial resolutions. The differences can be as large as +150 percent and -55 percent.

3.5 Optimum Threshold Temperature vs. Spatial Resolution

Although background temperature does not change significantly with spatial resolution, the optimum threshold temperature required to obtain the best estimate of cloud area does change. (The best estimate of cloud area being that obtained from AVIRIS imagery, degraded to 50 m spatial resolution, using the 3BR method.) The optimum threshold temperature versus spatial resolution is depicted from four different perspectives in Fig. 4. Figure 4a shows the optimum threshold temperature as a function of spatial resolution. Figure 4b shows the difference between the optimum threshold and background temperature as a function of spatial resolution. Figure 4c shows the relative change of Fig. 4a with respect to the 50 m threshold. Figure 4d shows the relative change of Fig. 4b with respect to the 50 m threshold difference.

Figures 4a and 4c indicate that the optimum temperature threshold is a function of spatial resolution and, in general, decreases with decreasing spatial resolution. Scenes B and M are the exception. That is, if cloud area increases with decreasing spatial resolution for a given temperature threshold (i.e., the 3BR temperature threshold), then the temperature threshold must increase to maintain the same cloud area. However, the precise effect of spatial resolution on optimum threshold temperature is unknown. For example, the change in the optimum threshold temperature ranges from +0.6°C with respect to the threshold temperature at 50 m to -1.5°C at 500 m spatial resolution.

Figures 4b and 4d better portray the problem of establishing the optimum temperature threshold as a function of spatial resolution since, typically, the threshold is based on the background temperature. It is clear from Fig. 4b that there is a large variability in optimum threshold temperature, with respect to the background temperature, independent of the spatial resolution, whether it be high or low. Even if the optimum threshold temperature is known for some high spatial resolution imagery, Fig. 4d indicates that it is difficult to estimate the optimum threshold temperature at some lower spatial resolution. ___xample, these results indicate that at 500 m spatial resolution, the required adjustment in threshold temperature can range from -0.5°C to +1°C. At 1000 m spatial resolution, the range is -0.6°C to +1°C.

3.6 Temperature Thresholds

In Fig. 5, the background temperature and the 3BR temperature threshold for all seven scenes are plotted. In Fig. 5a, the actual values are plotted; and in Fig. 5b, the differences between these values is plotted. Of note is that the difference between the background temperature and the 3BR temperature is not constant for this set of images; again this reinforces the fact that the temperature threshold is scene dependent. The horizontal line in Fig. 5b indicates the average difference of 2.5°C. This result corroborates the results of section 3.2 which indicate that the optimum threshold is between 2-3°C below the background temperature.

4. Discussion and Conclusions

In this study, we implement a method for registering AVIRIS and TIMS imagery to each other, so that cloud fraction retrievals between the two sensors can be compared and the sensitivity of cloud fraction retrievals from thermal wavelength imagery to threshold and spatial resolution can be investigated. The registration is admittedly imperfect; however, a combination of visual inspection and quantitative results indicate that registration errors are the cause of less than 3 percent of differences in the comparisons between AVIRIS and TIMS imagery.

When we use the best estimate of cloud area (i.e., as determined by applying the 3BR method to AVIRIS imagery) as the criteria for establishing the optimum temperature threshold in the TIMS imagery, we find that the best threshold is generally between 2 and 3°C below the background temperature. However, for this set of seven scenes, obtained over the same geographical area and time period, the optimum temperature threshold is significantly scene dependent. The optimum temperature threshold ranges from 1.8 to 3.6°C below the background temperature. Small deviations in the temperature threshold from the optimum one (<1°C), incur significant changes in the estimate of cloud area (up to 15 percent). Estimates of cloud fraction are especially sensitive to threshold selection for these types of clouds (i.e., low-level, relatively warm FWC) since the temperature contrast between cloud and background pixels is low. In general, estimates of cloud area increase with decreasing spatial resolution. However, these results indicate that at some lower spatial resolution, estimates of cloud area begin to decrease with decreasing spatial resolution. Thermal imagery possibly manifests this characteristic at higher spatial resolutions than does solar wavelength imagery (such as from AVIRIS), since the radiance function over the cloud top is more uniform and has less contrast with the background. Current efforts are directed at attempting to identify a set of scene features that will allow one to best compensate these estimates as a function of spatial resolution.

The temperatures of cloud edges in thermal imagery are distributed over a relatively broad range of temperatures (e.g., 7°C over a total scene temperature range of 14°C) that significantly overlap the temperature distribution of background pixels. Although reasonably good agreement in cloud pixel identification is obtained between AVIRIS and TIMS in this set of scenes, potentially less satisfactory agreement will be obtained for scenes with less uniform temperature backgrounds. The best technique for accurate cloud pixel identification in the infrared region is through high spatial resolution; however, high spatial resolution imagery is not always practical. Therefore, parameterizations are needed to adjust estimates of cloud properties obtained from low spatial resolution imagery. This can only be done if we first understand which scene features (e.g., time of day and year, geographical location, cloud uniformity, height, size, and distribution, etc.) provide the key to establishing those parameterizations.

The results reported here are only for continental FWC, perhaps one of the most difficult cloud types to retrieve properties for accurately using satellite imagery. Stratiform cloud properties can be retrieved with far greater certainty. Cloud property retrievals and their sensitivity to thresholding and spatial resolution need to be studied for a more diverse set of FWC cloud scenes over a variety of backgrounds. They also need to be studied for other cloud types, including cirrus, mixed phased clouds and those resulting from the breakup of stratiform clouds.

5. Recommendations for Future Work

Recommendations for future work are summarized as follows:

1) Investigate cloud features that might resolve the large dispersion of errors in estimates of cloud area with decreasing spatial resolution.

2) Investigate retrieval of cloud area from other types of cloud fields, over various types of backgrounds (e.g., cirrus over land, stratiform over land and water, cumuliform over water, broken stratiform over water, etc.).

3) Investigate techniques for recovering emissivity from optically thin cloud regions.

6. Relation of Ultimate Objectives to the Contract Work

This work is in support of the development of cloud products for the ASTER program. Specially, this work has investigated the effect of spatial resolution on retrieved cloud area and the optimum temperature threshold for continental fair weather cumulus cloud fields.

7. References

Gao, B. C., and A. F. H. Goetz, 1990: Column atmospheric water vapor and vegetation liquid water retrievals from airborne imaging spectrometer data. *J. Geophys. Res.*, **95**, 3549-3564.

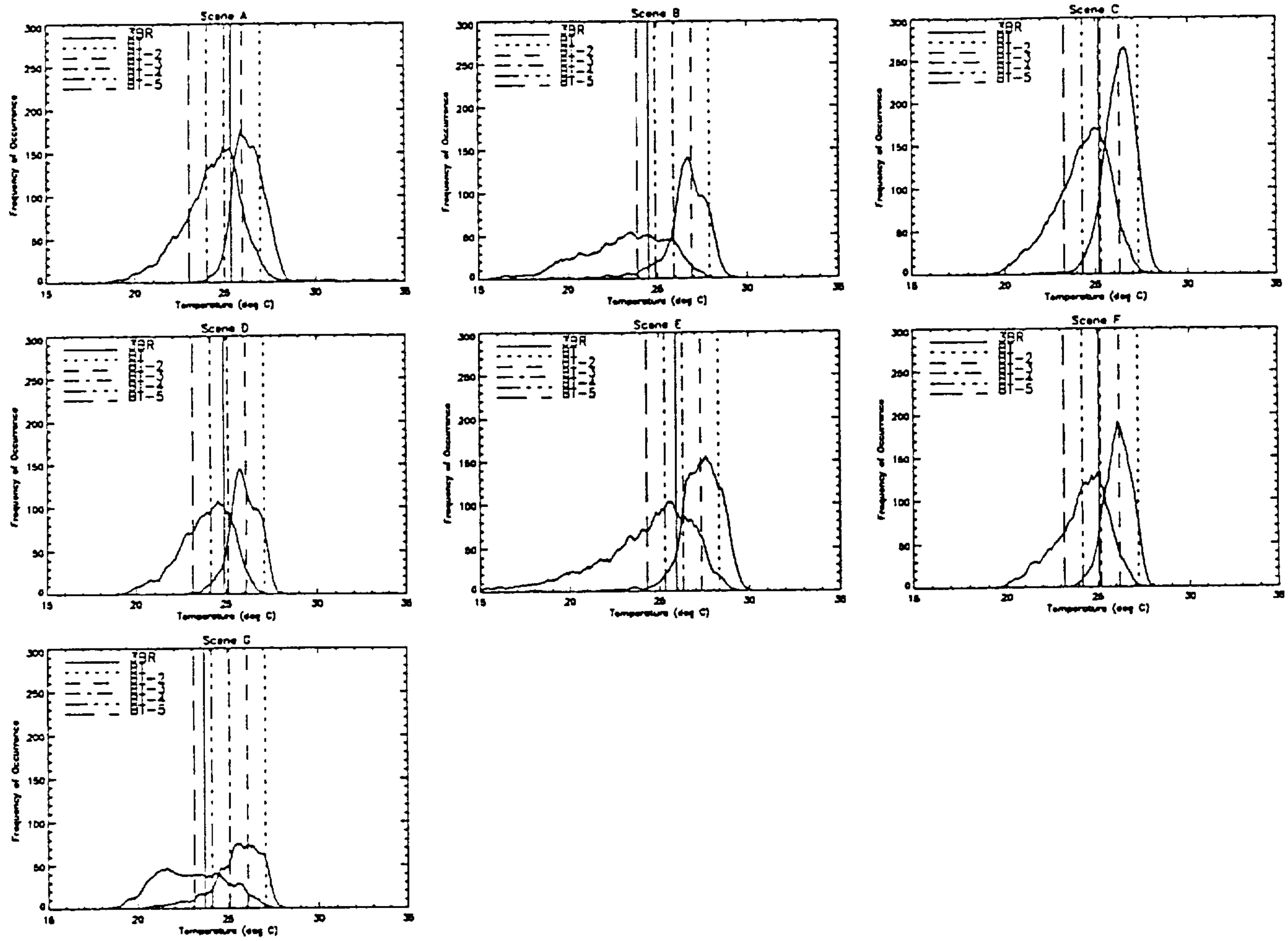

Fig. 1. Frequency distribution of temperatures for 3BR cloud edges for all seven scenes (band 5).

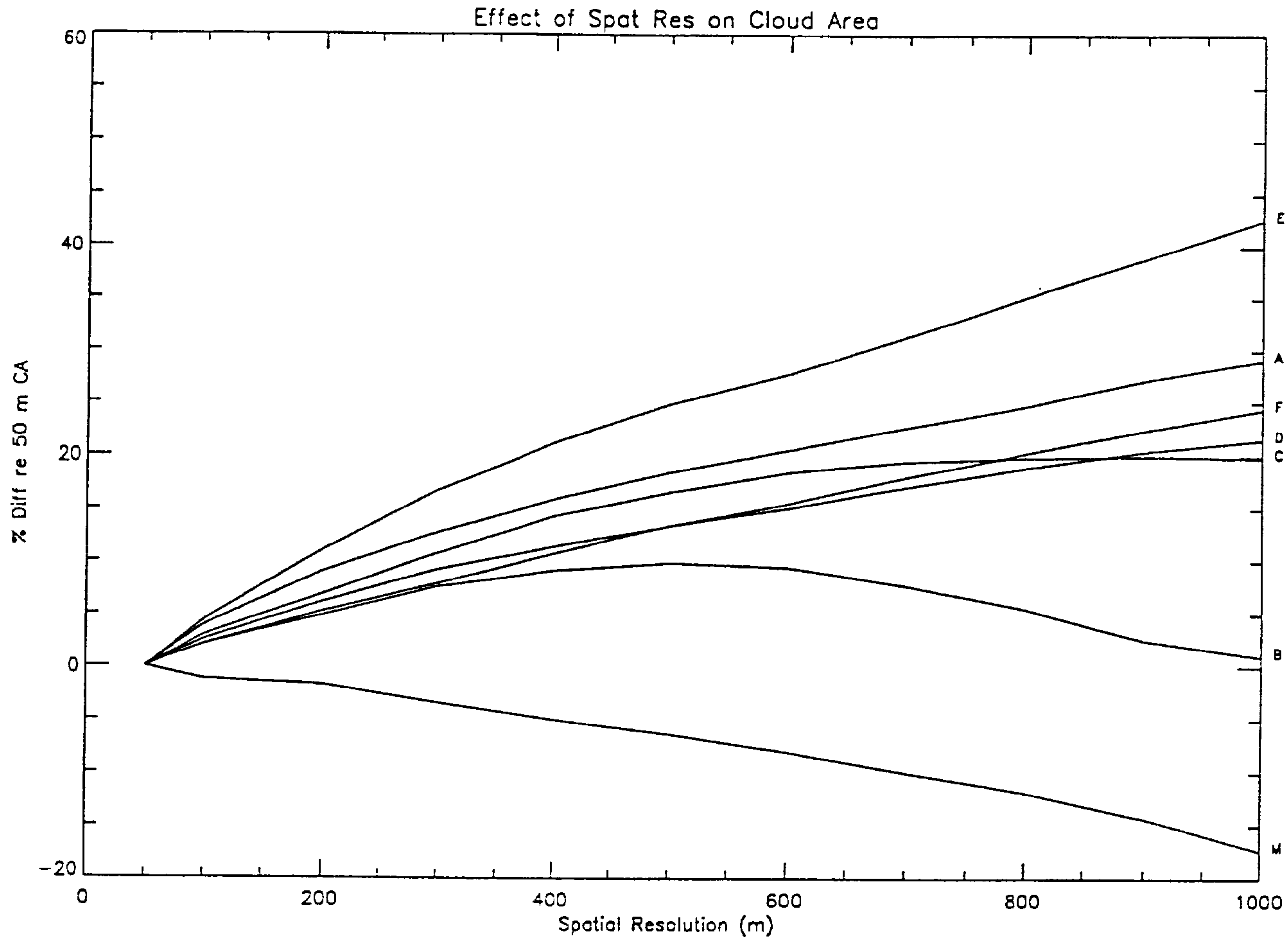

Fig. 2. Cloud area vs. spatial resolution for seven TIMS scenes. Cloud area is expressed as percent difference with respect to cloud area for the 50 m TIMS image (band 5).

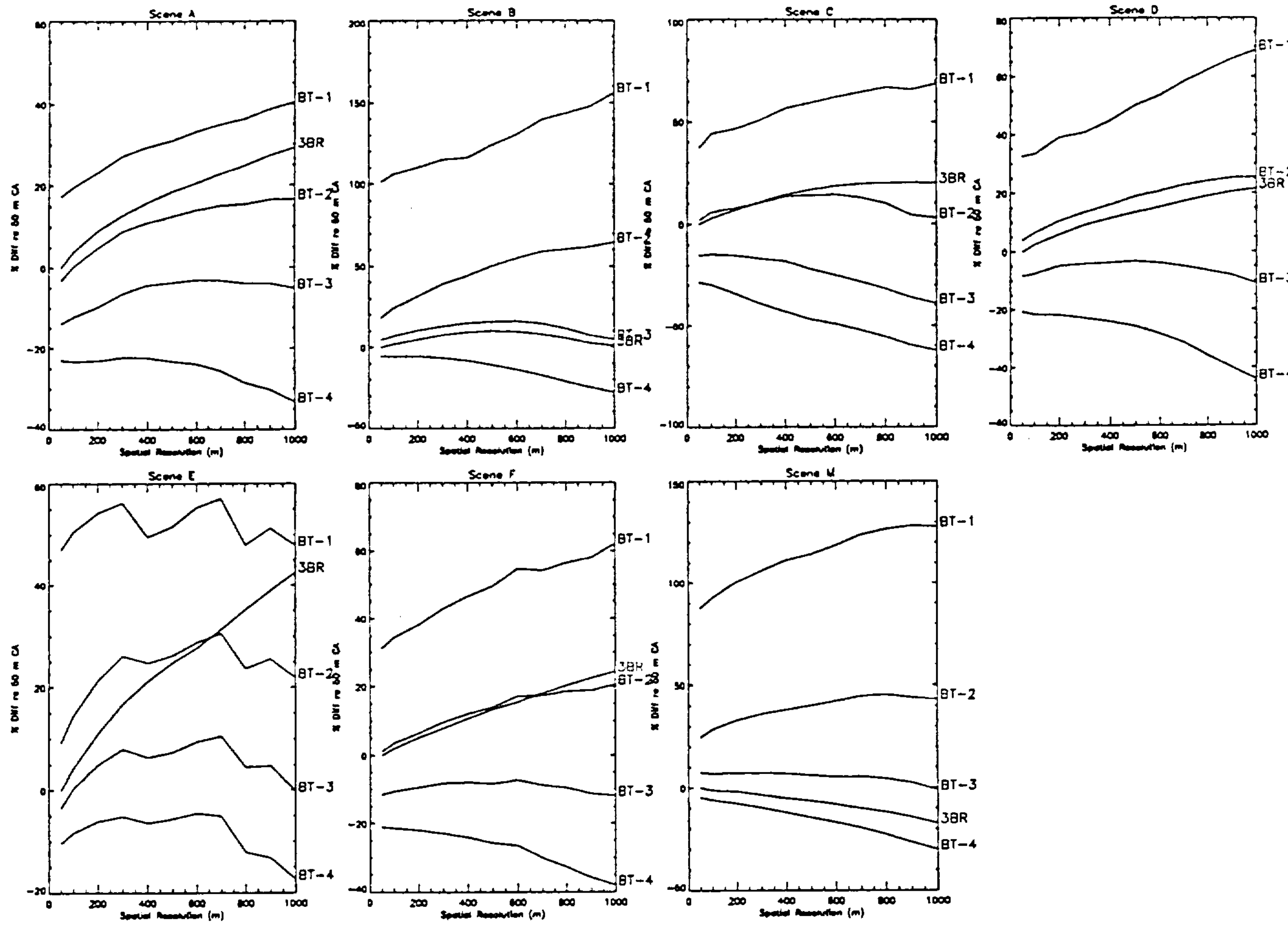

Fig. 3. Effect of temperature threshold on cloud area estimation for all seven scenes as a function of spatial resolution. Cloud area is expressed as percent difference with respect to cloud area in 50 m TIMS image (band 5).

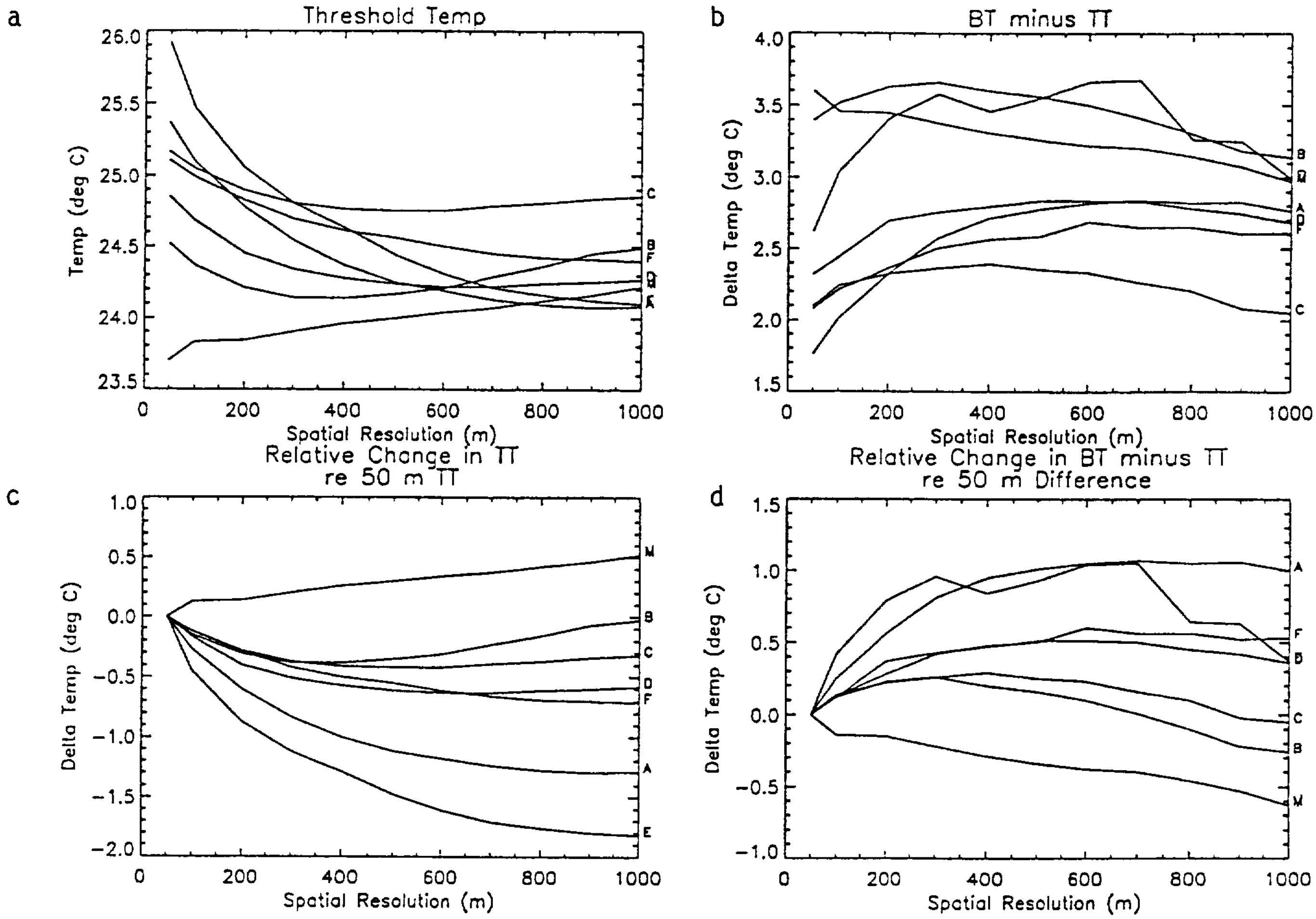

Fig. 4. Spatial resolution vs. (a) threshold temperature; (b) difference between peak background temperature and optimum threshold temperature; (c) relative change in (a) with respect to the threshold temperature for the 50 m image; (d) relative change in (b) with respect to the difference for the 50 m image vs. spatial. (Band 5 and all seven TIMS scenes.) (BT indicates background temperature and TT indicates threshold temperature.)

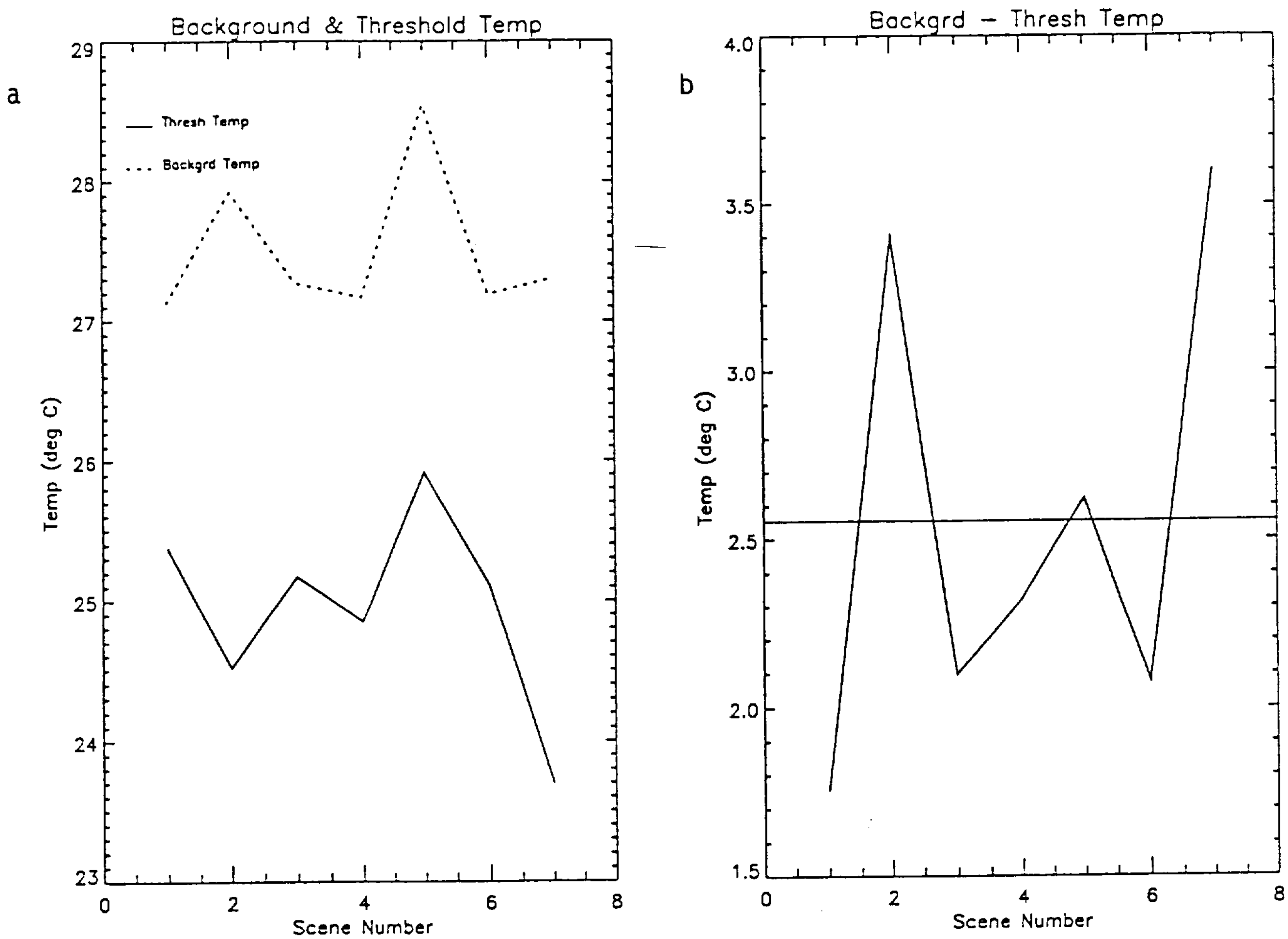

Fig. 5. For each scene (band 5): (a) the temperature threshold and peak background temperature; (b) difference between the peak background temperature and the threshold temperature.

Simultaneous Retrievals of Optical Thickness and Effective Radius from Multispectral Imagery

1. Introduction

The fundamental basis for the retrieval of optical thickness and effective radius is the comparison of measured radiance with model values. Specifically, a Mie scattering model for droplets/particles and the discrete ordinate radiative transfer model are used to generate model radiances for a range of potential microphysical properties based on some set of specific physical constraints (such as wavelength, solar zenith angle, background albedo, etc.). The model radiances are then compared with measured cloud radiances to determine which set of modeled microphysical properties provides the best match. Unfortunately, the measured radiance in one band does not unambiguously determine the microphysical conditions that manifested it. Therefore, it is necessary to utilize multispectral imagery to resolve the ambiguities as the radiative properties of cloud droplets/particles vary as a function of wavelength.

The methodology for retrieving cloud properties during the daytime is well established in comparison to the methodology for retrieving them at night. Daytime retrievals utilize solar wavelength imagery while, by necessity, nighttime retrievals can only be based on thermal IR imagery. In fact, a methodology for retrieving cloud properties using thermal IR wavelengths is still under investigation and the potential for developing a robust technique is dubious. The differences in radiative characteristics of droplets/particles at solar wavelengths as a function of microphysical properties provide a much stronger signature than at thermal IR wavelengths.

In general, optical thickness and effective radius are retrieved simultaneously, as one can be expressed as a function of the other. The retrieval of optical depth (or thickness) refers specifically to the optical depth at 0.75 μm. Optical depth is referenced to 0.75 μm as it is a non-absorbing wavelength and, therefore, the reflection function is affected only by scattering due to cloud droplets/particles and not by atmospheric gaseous absorption.

2. Methodology

2.1 Retrieval of Optical Depth and Effective Radius from Solar Wavelength Imagery (Daytime Retrievals)

A comprehensive discussion of the theoretical basis for retrieving optical depth and effective radius from solar wavelength imagery is presented in Nakajima and King [1991]. A synopsis appears as follows. The reflection function of clouds at various wavelengths of the solar spectrum is determined by the size distribution of the droplets/particles. At 0.75 μm (e.g., band 3 of ASTER), cloud reflection is largely a function of liquid water path and partially one of particle size distribution effective radius. Conversely, at near infrared wavelengths (e.g., ASTER bands 6 and 7 - 2.1 to 2.3 μm), cloud reflection is largely a function of particle size distribution effective radius and less a function of liquid water path. In fact, at large optical depths (> 12), reflectance at 0.75 μm is only a function of optical depth and reflectance at 2.16 μm is only a function of effective radius. This phenomena is observed is Fig. 1 in which the reflection function at 2.16 μm is plotted against the reflection function at 0.75 μm for lines of constant optical depth and effective radii.

For optical depth greater than 12, lines of constant optical depth and effective radii are orthogonal. As a result, at large optical depths, optical depth and effective radius can be retrieved from reflectance measured at 0.75 μm and particle size can be retrieved at or near 2.16 μm. At optical depths less than 12, optical depth and effective radius are retrieved simultaneously, as multi-solution effective radius retrievals for at a specific optical depth at 0.75 μm become conditionally unambiguous (see the following paragraph) when considering the same physical depth at 2.16 μm or 2.25 μm.

One of the major deficiencies in this retrieval methodology can be observed in Fig. 1. The curves of constant effective radii for $r_e < 4$ μm significantly overlap the curves for $r_e > 5$ μm, indicating a serious ambiguity problem. For smaller values of optical depth, there are 2 solutions for optical depth and effective radius for each pair of reflectances at 0.75 μm and 2.16 μm. The ambiguity is caused by the abrupt change in the scattering efficiency as the size parameter (i.e., $2 \pi r / \lambda$) transitions from the Mie region to the optical region. The only way to resolve this ambiguity is through a priori knowledge. For the present, it will be assumed that distributions with $r_e < 4$ are unrealistic or of very low probability and will not be considered. In the future, as more cloud scene types are tested, better a priori knowledge about potential r_e values, based on some regional, temporal, climatological factors, etc., should be available.

2.2 Retrieval of Optical Depth and Effective Radius from Thermal IR Wavelength Imagery (Nighttime Retrievals)

As indicated in the introduction, an algorithm for retrieving cloud properties from thermal IR imagery is still under investigation. A comprehensive discussion of a potential approach currently being tested appears in Prabhakara et al. [1988]. A summary of that technique follows. At solar wavelengths scattering is the dominant radiative effect and the source of the radiation (i.e., the sun) for which this effect is measured, is from the same general direction that the sensor measurements are made. At thermal IR wavelengths absorption is the dominant radiative effect and the source of the radiation is from the background (e.g., the surface), atmospheric constituents, and/or cloud droplets/particles. To retrieve cloud properties at thermal IR wavelengths some relationship between the absorptive effects of different size distributions of droplets/particles and radiance must be established. In the 8-12 μm region droplet/particle absorption is a function of wavelength wherein absorption increases with increasing wavelength (see Fig. 2).

If a cloud is sufficiently thin such that the radiance measured at the satellite sensor is comprised of contributions from both the cloud and the background (i.e., cloud emissivity < 1), then the difference in absorption of background radiation at different wavelengths can be used to estimate cloud droplet/particle size distribution and infer optical depth and effective radius. The effect is demonstrated in Figs. 3a and 3b in which temperature difference at 2 wavelengths (i.e., 8.4 μm and 11.7 μm) is plotted against effective radius and optical depth. Each curve in Fig. 3a indicates constant optical depth while each curve in Fig. 3b indicates constant effective radius.

One can see that for optically thin regions significant temperature differences correspond to different effective radii. However, for optically thicker values, cloud properties (i.e., effective radius) cannot be resolved. It appears at the present time that robust nighttime retrieval of optical properties will not be feasible. For example, retrieval of microphysical properties for thin cirrus appears likely, whereas those for a thick stratiform deck do not.

3. Results (Preliminary)

For a set of measured multispectral reflectances (i.e., from ASTER bands 3, 4, 6, and 7), corresponding to a specific cloud pixel, the Euclidean distance between each spectral set of model reflectances (wherein each one

corresponds to a specific optical depth and effective radius) and each measured reflectance, is computed as follows:

$$D(\tau,r_e) = (\Sigma(R_{m,i}^2 - R_{t,i}^2))^{0.5}$$

where,

$D(\tau,r_e)$ = Euclidean distance for a specific τ and r_e
$R_{m,i}$ = Measured reflectance in band i
$R_{t,i}$ = Table lookup value for model reflectance in band i
i = band number

The retrieved optical depth and effective radius then corresponds to the pair that have the smallest Euclidean distance. The technique is demonstrated in Fig. 4 using only 2 bands. The solid and dashed lines indicate model results for constant optical depth and effective radius. The points indicate measured reflectances from a stratocumulus over water cloud scene. The main clustering (and, consequently, minimum Euclidean distance) of measured values occurs around optical depth 11 and effective radius 8.

As can be seen in Fig. 4, the measured cloud reflectances cluster very nicely, indicating a relatively uniform distribution of droplets. However, 3-D cloud effects can manifest measured cloud reflectances which do not cluster nicely and, in fact, indicate unreasonable retrievals. This phenomena is demonstrated in Fig. 5 for a fair weather cumulus cloud scene. Hopefully, 3-D radiative models or compensating techniques will be available in the near future, so that this retrieval methodology will be more robust.

A variation of this technique, suggested by Twomey and Cocks [1989], which utilizes 0.75 µm (e.g., ASTER band 3) and the ratio of near IR bands (e.g., ASTER bands 4, 6, and 7) to 0.75 µm, is also being considered. It appears that this approach increases the orthogonality of optical depth and effective radius when optical depth is less than 12. The Euclidean distance for this technique is computed similarly and is represented mathematically as follows:

$$D(\tau,r_e) = ((R_{m,1}^2 - R_{t,1}^2) + \Sigma((R_{m,i} - R_{m,1})^2 - R_{t,i}/R_{t,1})^2))^{0.5}$$

where,

$D(\tau, r_e)$ = Euclidean distance for a specific τ and r_e
$R_{m,i}$ = Measured reflectance in band i
$R_{t,i}$ = Table lookup value for model reflectance in band i
i = band number

As before, the retrieved optical depth and effective radius correspond to the pair with the minimum Euclidean distance. The technique is demonstrated in Fig. 6 using only 2 bands. The solid and dashed lines indicate model results for constant optical depth and effective radius. The points indicate measured reflectance at 0.75 μm on the abscissa and the ratio of 2.16 μm to 0.75 μm on the ordinate.

4. Recommendations for Future Work

Recommendations for future work are summarized as follows:

1) Investigate the retrieval of optical thickness and effective radius from additional scenes containing broken cloudiness over land and water. The effects of background albedo, cloud to cloud shadowing, and the 3-D structure need to be isolated so that cumuliform cloud properties can be retrieved properly.

2) Continue to investigate methods for retrieving cloud properties from thermal IR imagery.

3) Investigate the retrieval of cirrus cloud properties.

5. Relation to Ultimate Objectives of the Contract Work

This work is in support of the development of cloud products for the ASTER program. Specifically, this work has investigated methods for retrieving optical thickness and effective radius from water clouds using solar and thermal IR imagery. These methods should be applicable to other types of cloud fields.

6. References

Ackerman, S. A., W. L. Smith, J. D. Spinhirne, and H. E. Revercomb, 1990: The 27-28 October 1986 FIRE Cirrus Case Study: Spectral properties of cirrus clouds in the 8-12μm window. *Mon. Wea. Rev.*, **118**, 2377-2388.

Nakajima, T., M. D. King, and J. D. Spinhirne, 1991: Determination of the optical thickness and effective particle ardius of clouds from reflected solar radiation measurements. Part II: Marine stratocumulus observations. *J. Atmos. Sci.*, **48**, 728-750.

Prabhkara, C., R. S. Fraser, G. Dalu, M.-L. C. Wu, and R. J. Curran, 1988: Thin cirrus clouds: Seasonal distribution over Oceans Deduced from Nimbus-4 IRIS. *J. Appl. Meteor.*, **27**, 379-399.

Twomey, S., and T. Cocks, 1989: Remote sensing of cloud parameters from spectral reflectance in the near-infrared. *Beitr. Phys. Atmos.*, **62**, 172-179.

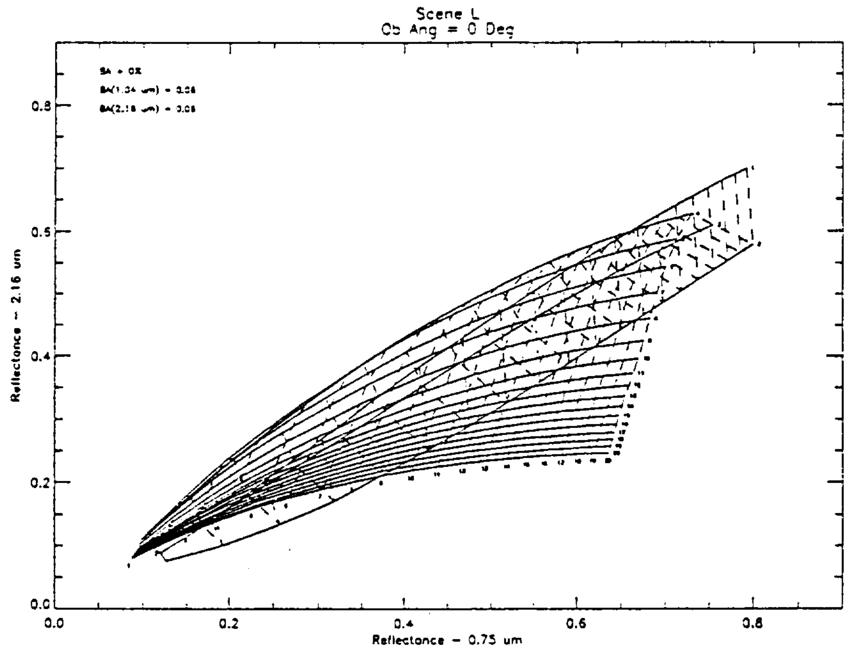

Fig. 1. Reflection function at 2.16 μm vs. 0.75 μm for solar zenith angle of 20.5 degrees. Solid lines indicate constant effective radii and dashed lines indicate constant optical depth. Based on discrete ordinate radiative transfer model results.

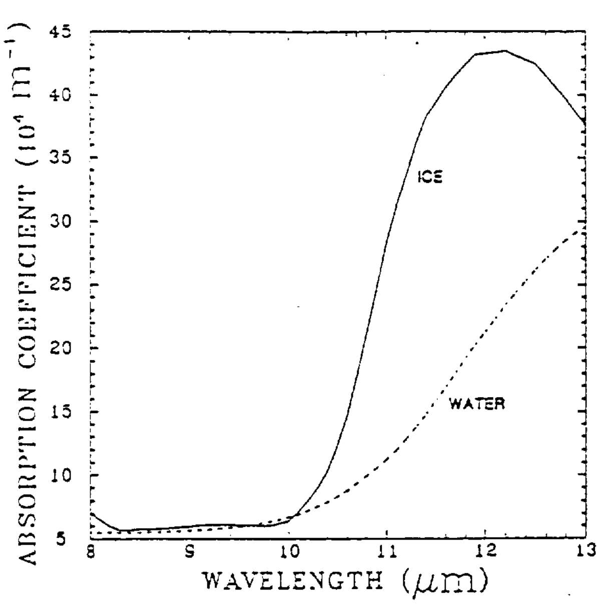

Fig. 2. Absorption coefficient of ice and water vs. wavelength. (From Ackerman et al., 1990)

a b

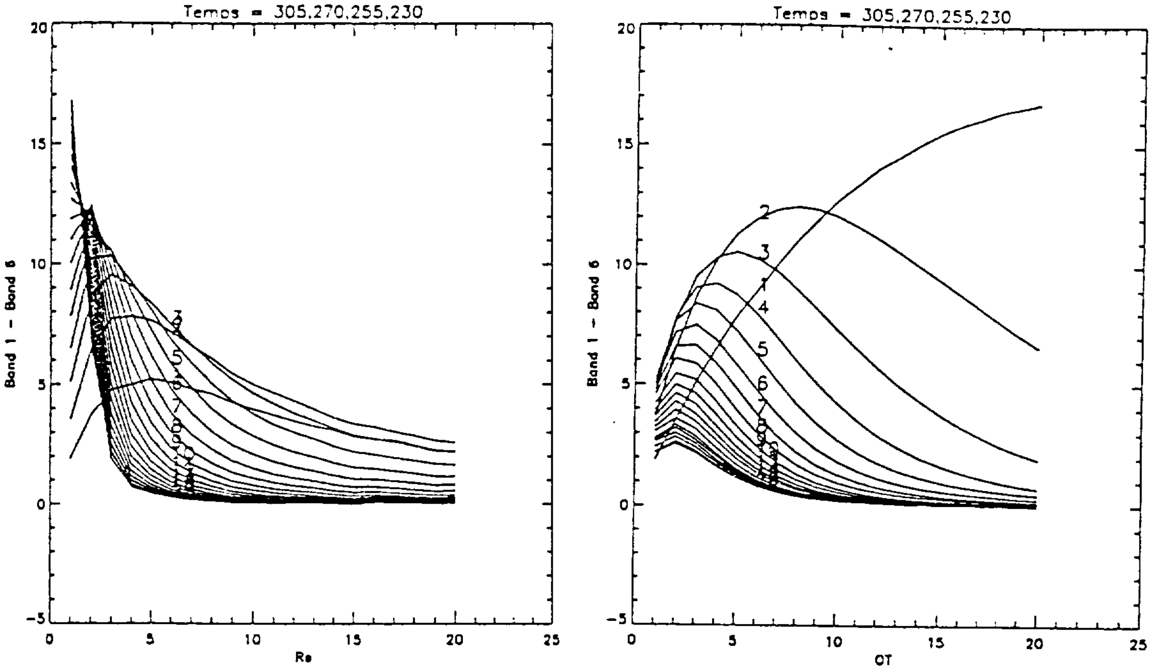

Fig. 3. Temperature difference in 2 TIMS bands (8.4 µm-11.7 µm) vs. (a) effective radius for 20 optical depths and (b) optical depth for 20 effective radii. Based on discrete ordinate radiative transfer model results for surface temperature of 305 deg K, cloud base temperature of 270 deg K, and cloud top temperature of 255 deg K.

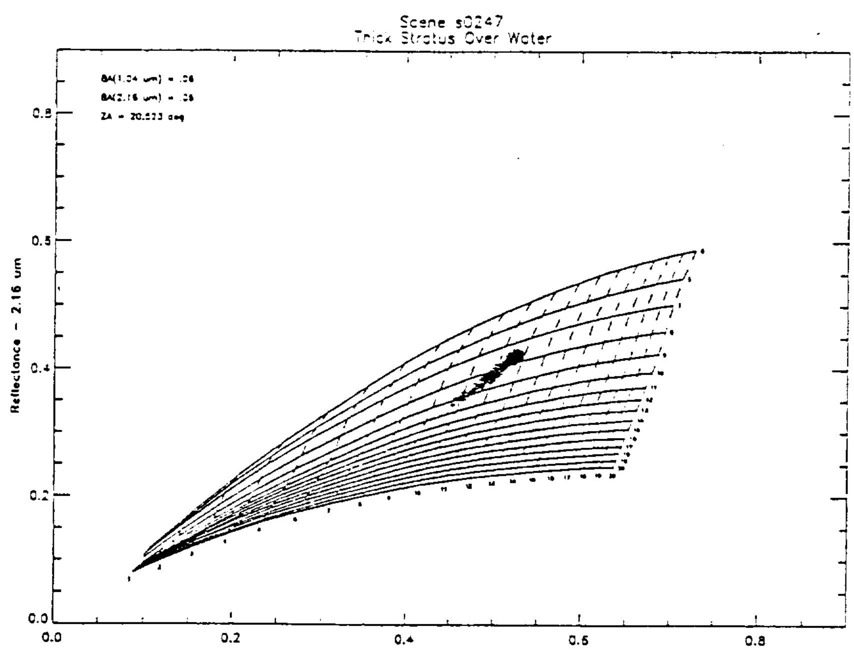

Fig. 4. Reflectance at 2.16 µm vs. 1.04 µm for model and measured results. Solid and dashed lines indicate constant optical depth and effective radius, respectively. Points indicate measured reflectances for a stratocumulus cloud scene over water. The solar zenith angle is 20.5 degrees, the observation angle is 0 degrees, and the background albedo is 0.06.

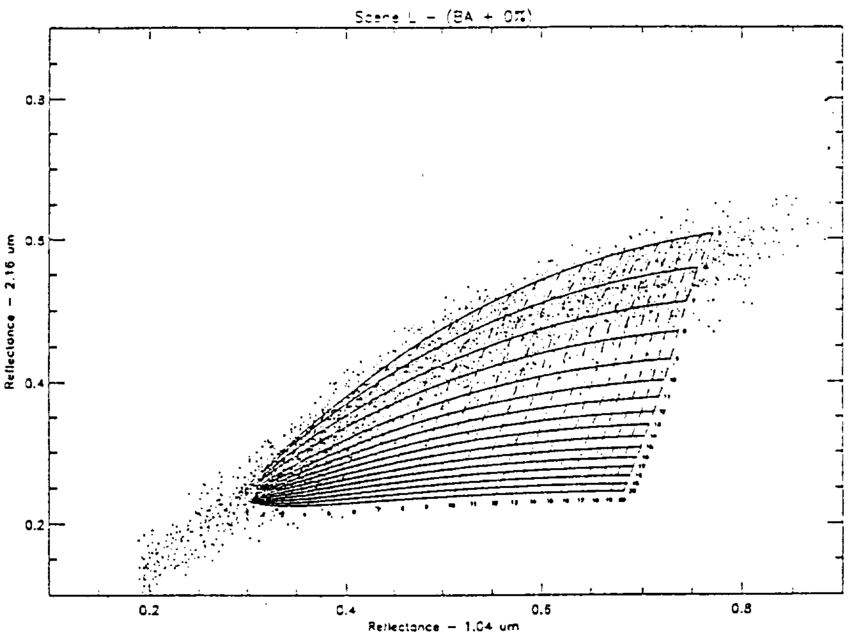

Fig. 5. Reflectance at 2.16 μm vs. 1.04 μm for model and measured values. Solid and dashed lines indicate constant optical depth and effective radius, respectively. Points indicate measured reflectances from a fair weather cumulus over land cloud scene. The solar zenith angle is 19.3 degrees, the observation angle is 0 degrees, and the background albedo is 0.3.

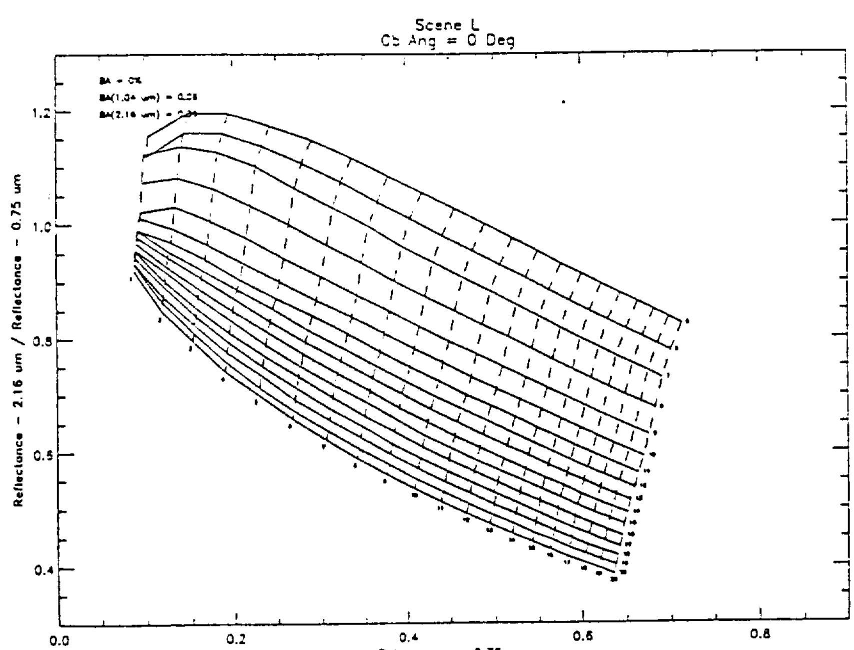

Fig. 6. Radio of reflectance at 2.16 μm to 0.75 μm vs. reflectance at 0.75 μm for model results. Solid and dashed lines indicate constant optical depth and effective radius, respectively. The solar zenith angle is 20.5 degrees, the observation angle is 0 degrees, and the background albedo is 0.06.

Software Development

The methodology for the development of software (S/W) follows the guidelines prepared by the ASTER team leader (TL) and described in the Team Member Algorithm S/W Development Document [Voge, C. and S. Larson, 1992].

The production of S/W by the team members (TMs) follow three different methodology and S/W life cycles:

- Value added - The TM develops an algorithm and prototype S/W.
- Turn Key - The TM develops the algorithm, prototype and implement the algorithm.
- Specification only - The TM generates only detailed specifications for an algorithm.

In all three methods, the TM provides supporting and adequate documentation to the TL. Our group will use the turn key method to implement several cloud and sea-ice algorithms. The cloud products that will allow to have a better understanding of the earth's climate system are listed below:

Prod. number	level	Product name
2080	2C1	Cloud fractional area
1763	2C1	Cloud phase
1391	2C1	Cloud base height
1427	2C1	Cloud top height
3625	2C1	Cloud thickness
2310	2C1	Cloud optical thickness
1779	2C1	Cloud effective particle size
3626	2C1	Cloud liquid water content
2465	2C1	Cloud top temperature
2115	2C1	Cloud emissivity
1409	2C1	Cloud 3D structure
2093	2C1	Cloud field size distribution
3628	2C1	Cloud field scales of organization
3152	2C2	Sea ice fractional area

Sea-ice products are important to monitor the sea-ice changes and the effect of the polar regions in the global warming. The sea-ice products that will be implemented by our team are:

Prod. number	level	Product name
3616	2C2	Meltpond fractional area
3617	2C2	Lead fractional area
3618	2C2	New ice fractional area
3619	2C2	Polar sea ice temperature
3620	2C2	Polar sea surface temperature
3621	2C2	Sea ice size distribution
3627	2C2	Sea ice lead size distribution
3624	2C2	Sea ice albedo

The S/W development process consists of two life cycles (LC) : an algorithm prototype LC

and a production S/W LC. The prototype LC corresponds to the production of a prototype for each algorithm. The phases for the algorithm LC consists of the generation of an algorithm theoretical document, the implementation of a prototype for each algorithm, and the algorithm acceptance testing. So far, the first phase has been completed and it is under review by the TM. Copies of the algorithm documents are given in appendix A.

The production S/W LC phases are interleaved with the algorithm LC. It consists of a S/W management plan, a S/W integration management plan, user's guide and operators manual, system requirements analysis, system design analysis, S/W requirement analysis, a S/W architectural design, S/W code and unit test, S/W acceptance testing, integration and system acceptance test, and the S/W delivery review. Currently, we are writing the S/W management plan and the S/W integration management plan.

Object-Oriented Paradigm

We expect to implement some of the algorithms using the new object-oriented (OO) S/W development approach. C++ and C are the deliverable programming languages. However, for the algorithm prototypes we will deliver some of the code in the Interactive Data Language (IDL).

OO technology presents four basic principles which either does not exist or are not clear defined in the conventional S/W development approach. These four basic principles are:

- Abstraction - It allows a concise representation of concepts and ideas into objects.
- Encapsulation - Implementation details of an abstraction are collected into a protected entity.
- Inheritance - It is the ability of an object to inherit properties from one or more objects.
- Polymorphism - It is the ability of heterogenous objects to respond to the same message.

The OO LC will have similar phases as the conventional approach. The analysis and design phases have different outcomes. The OO notation that will be used will be a combination of Schlaer/Mellor methodology [Schlaer, S. and S. Mellor, 1989] for the analysis phase and Booch [Booch, G., 1991] methodology for the design phase.

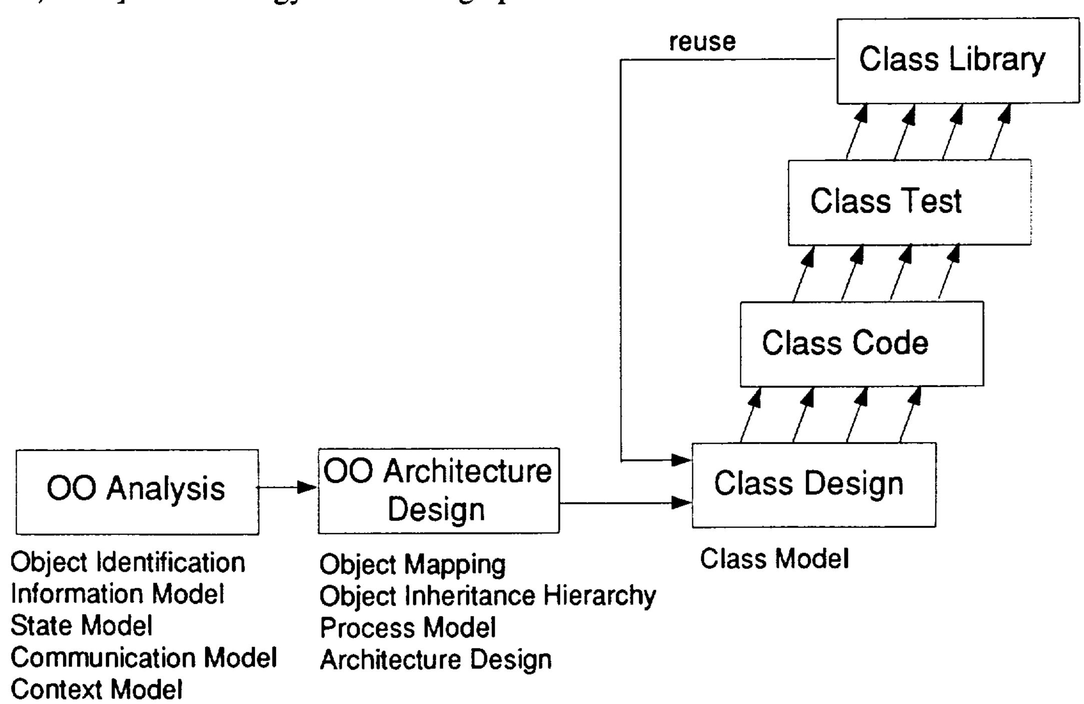

Figure 1. Analysis/Design Phases in the Object-Oriented Life Cycle Approach

Schlaer/Mellor notation includes the context diagram, information model diagram, object state model represented by state transition diagrams, and the communication model diagram. Booch notation includes the class diagram and the module/process diagram. The analysis and design phases along with the outcomes are illustrated in Figure 1.

Acronyms

IDL	Interactive data language
LC	Life cycle
OO	Object-Oriented
S/W	Software
TL	Team Leader
TM	Team member

References

Booch, G., 1991: Object-Oriented Design with Applications. Benjamin/Cummings.

Schlaer, S. and S. Mellor, 1989: Object-Oriented System Analysis: Modeling the World with Data. Prentice Hall, Englewood Cliffs, NJ.

Voge, C. and S. Larson, 1992: ASTER Team Member Algorithm Software Development Guidelines, Version 1.0, October 29, U.S. Science Meeeting, Tucson, Arizona.

APPENDIX A

Algorithm Theoretical Basis Document
for ASTER Products

Algorithm Theoretical Basis Document
for ASTER Products:

Product #	Level	Product
2310	2C1	Cloud Optical Thickness
1779	2C1	Cloud Effective Radius
3626	2C1	Cloud Liquid Water Content

Version 1

December 1992

Team Member:
Dr. Ronald M. Welch
Institute of Atmospheric Sciences
South Dakota School of Mines and Technology
501 E. St. Joe St.
Rapid City, SD 57701

Table of Contents

1.0 Introduction

This Algorithm Theoretical Basis Document describes the methodology (as currently envisioned) necessary to retrieve the following level 2C1 cloud microphysical properties:

2310	Cloud Optical Thickness (τ)
1779	Cloud Particle Effective Radius (r_e)
3626	Cloud Liquid Water Content (LWC)

A description of the theoretical basis for the retrievals is provided as well as a description of the algorithmic implementation. The algorithm for these cloud property retrievals is currently under development and, consequently, variations of the algorithm are still being tested. As a result, the algorithm is presently fluid and, in the future, some aspects of the algorithm will be modified, deleted, augmented, and/or replaced.

The fundamental basis for this methodology is the comparison of measured radiance with model values. Specifically, a Mie scattering model for droplets/particles and the discrete ordinate radiative transfer model are used to generate model radiances for a range of potential microphysical properties based on some set of specific physical constraints (such as wavelength, solar zenith angle, background albedo, etc.). The model radiances are then compared with measured cloud radiances to determine which set of modeled microphysical properties provides the best match. Unfortunately, the measured radiance in one band does not unambiguously determine the microphysical conditions that mainfested it. Therefore, it is necessary to utilize multispectral imagery to resolve the ambiguities as the radiative properties of cloud droplets/particles vary as a function of wavelength.

The methodology for retrieving cloud properties during the daytime is well established in comparison to the methodology for retrieving them at night. Daytime retrievals utilize solar wavelength imagery while, by necessity, nightime retrievals can only be be based on thermal IR imagery. In fact, a methodology for retrieving cloud properties using thermal IR wavelengths is still under investigation and the potential for developing a robust technique is dubious. The differences in radiative characteristics of droplets/particles at solar wavelengths as a function of microphysical properties provide a much stronger signature than at thermal IR wavelengths.

In general, optical thickness and effective radius are retrieved simultaneously, as one can be expressed as a function of the other. LWC is then computed directly from the retrieved optical depth and effective radius. In this document, numerous wavelengths/bands are cited in the methodology for retrieving cloud properties; however, the retrieval of optical

depth (or thickness) refers specifically to the optical depth at 0.75 um. Optical depth is referenced to 0.75 um as it is a nonabsorbing wavelength and, therefore, the reflection function is affected only by scattering due to cloud droplets/particles and not by atmospheric gaseous absorption.

A list of references for this document is provided as an attachment.

2.0 Overview and Background Information

Clouds are one of the most important modulators of the Earth's radiation budget. They reflect the incoming solar radiation and absorb the longwave radiation emitted by the Earth. Cloud optical properties (e.g., optical thickness, effective radii, LWC) influence the reflection, transmission, and absorption of radiation in a cloudy atmosphere. An intercomparison of 14 global circulation models (GCMs) by Cess et al. [1989] shows that a threefold variation in climate sensitivity among the models is largely due to the differences in the modeled cloud-climate feedback. Recent GCM simulations by Roeckner et al. [1987] show that cloud LWC and optical depth increase in response to the doubling of carbon dioxide concentration, indicating the importance of including cloud microphysical properties in model simulations. Accurate determination of cloud optical properties is paramount to the understanding of cloud-climate feedback and, consequently, their effect on climate.

2.1 Experimental Objective

Since ASTER is a high spatial resolution instrument, it is not feasible to retrieve the aforementioned cloud microphysical properties on a global scale, such as is needed by global climate modelers. The global retrievals of these properties is to be accomplished through the use of the lower spatial resolution imagery obtained from the Moderate Resolution Imaging Spectrometer (MODIS). However, cloud properties retrieved through the use of MODIS imagery will manifest a presently unquantifiable bias due to the effects of relatively large scale spatial averaging of the cloud radiance function. Some small scale cloudiness will not even be detected. A recent study by Wielicki and Parker [1991] shows that large differences in estimates of cloud cover are due to spatial resolution. In another study, Feind et al. [1992 - in press] show that estimates of retrieved optical depth decrease with decreasing spatial resolution. Cloud property retrievals from ASTER will augment (i.e., not supplant) MODIS retrievals. ASTER and MODIS retrievals will be directly comparable since the ASTER will obtain subsets of temporally and spatially similar MODIS imagery. Retrievals from ASTER will also serve to validate and/or augment retrievals from other

lower spatial resolution instruments (e.g., AVHRR, GOES).

2.2 Historical Perspective

The methodology described in this document is currently being tested on AVIRIS, TIMS, and LANDSAT TM imagery. This methodology has also been applied by Twomey and Cocks [1989] and Nakajima et al. [1991]. Twomey and Cocks retrieved stratocumulus cloud properties from an aircraft multispectral radiometer and compared the retrievals to aircraft in situ measurements. Nakajima et al. did the same using measurements from the Multispectral Cloud Radiometer. The current archive for high spatial resolution (less than 100 m), mutispectral imagery is currently very limited and in-house testing has only been conducted on a relatively few cloud types (e.g., stratocumulus over water and tropical fair weather cumulus over land). As more datasets become available, the algorithm will be tested on a more diverse set of cloud scenes.

2.3 Instrument Characteristics

As indicated in the introduction, daytime retrievals rely on imagery obtained at visible and near IR wavelengths. Therefore, ASTER VNIR band 3 and SWIR bands 4, 6, and 7 are necessary for daytime retrievals. Although a methodology for nightime retrievals is not yet established, it appears that any viable technique will require the use of the TIR bands 10, 11, 13, and 14.

3.0 Algorithm Description

This section is subdivided into two main sections - Theoretical Description (3.1) and Practical Considerations (3.2). Section 3.1 is subdivided into the following 3 subsections: 3.1.1- Physics of the Problem, 3.1.2 - Mathematical Description of Algorithm - Daytime Retrievals, and 3.1.3 - Variance or Uncertainty Estimates. Section 3.1.1 is further subdivided into the following 4 subsections: 3.1.1.1 - Definition of Optical Depth, Effective Radius, and LWC, 3.1.1.2 - Retrieval of Optical Depth and Effective Radius from Solar Wavelengths (Daytime Retrievals), 3.1.1.3 - Retrieval of Optical Depth and Effective Radius from Thermal IR Wavelengths (Nightime Retrievals), and 3.1.1.4 - Mie Scattering and Discrete Ordinate Radiative Transfer Models. Section 3.2 is subdivided into the following 5 subsections: 3.2.1 - Numerical Computation Considerations, 3.2.2 - Programming/Procedural Considerations, 3.2.3 - Calibration and Validation, 3.2.4 - Quality Control and Diagnostics,

and 3.2.5 - Exception Handling.

3.1 Theoretical Description

3.1.1 Physics of the Problem

3.1.1.1 Definition of Optical Depth, Effective Radius, and LWC

Optical depth, effective radius, and LWC are three cloud microphysical parameters that are essential in determining cloud radiative effects and cloud-climate feedback. They are strictly a function of the size distribution of the droplets/particles that makeup the cloud. (Optical depth is also a function of wavelength). Mathematically optical depth, effective radius, and LWC are defined as follows:

$$\tau = \int\int \pi r^2 Q_e (r,\lambda)\, n(r,s)\, dr\, ds$$

$$r_e = \frac{\int r^3 n(r)\, dr}{\int r^2 n(r)\, dr}$$

$$LWC = \int \rho(r)\, \pi\, 4/3\, r^3 n(r)\, dr$$

where,

r = droplet/particle size
s = depth of the scattering medium
$n(r)$ = size distribution
$Q_e(r,\lambda)$ = volumetric extinction efficiency
$\rho(r)$ = density of droplet/particle

Optical depth is a measure of the opacity of the cloud or the fraction of radiation that is transmitted through it. Effective radius is a measure of the average scattering radius of the cloud droplets/particles. LWC is self explanatory.

3.1.1.2 Retrieval of Optical Depth and Effective Radius from Solar Wavelength Imagery (Daytime Retrievals)

A comprehensive discussion of the theoretical basis for retrieving optical depth and effective radius from solar wavelength imagery is presented in Nakajima and King [1991]. A synopsis appears as follows. The reflection function of clouds at various wavelengths of the solar spectrum is determined by the size distribution of the droplets/particles. At 0.75 um (e.g., band 3 of ASTER), cloud reflection is largely a function of liquid water path and partially one of particle size distribution effective radius. Conversely, at near infrared wavelengths (e.g., ASTER bands 6 and 7 - 2.1 to 2.3 um), cloud reflection is largely a function of particle size distribution effective radius and less a function of liquid water path. In fact, at large optical depths (> 12), reflectance at 0.75 um is only a function of optical depth and reflectance at 2.16 um is only a function of effective radius. This phenomena is observed is Figure 1 in which the reflection function at 2.16 um is plotted against the reflection function at 0.75 um for lines of constant optical depth and effective radii.

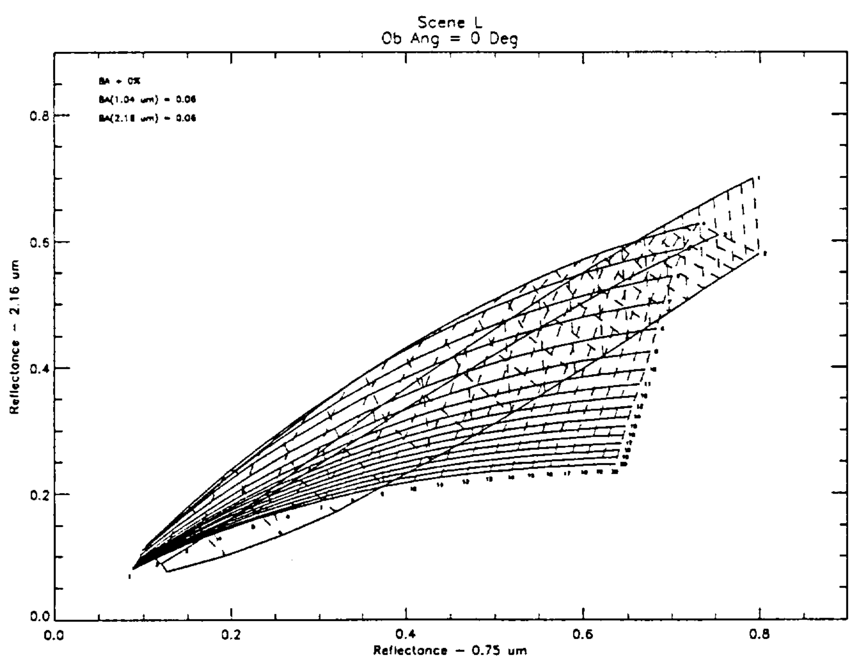

Figure 1. Reflection function at 2.16 um vs. 0.75 um for solar zenith angle of 20.5 degrees. Solid lines indicate constant effective radii and dashed lines indicate constant optical delpth. Based on discrete ordinate radiative transfer model results.

For optical depth greater than 12, lines of constant optical depth and effective radii are orthogonal. As a result, at large optical depths, optical depth and effective radius can be retrieved from reflectance measured at 0.75 um and particle size can be retrieved at or near 2.16 um. At optical depths less than 12, optical depth and effective radius are retrieved simultaneously, as multi-solution effective radius retrievals for at a specific optical depth at 0.75 um become conditionally unambiguous (see the following paragraph) when considering the same optical depth at 2.16 um or 2.25 um.

One of the major deficiencies in this retrieval methodology can be observed in Figure 1. The curves of constant effective radii for $r_e < 4$ um significantly overlap the curves for $r_e > 5$ um, indicating a serious ambiguity problem. For smaller values of optical depth, there are 2 solutions for optical depth and effective radius for each pair of reflectances at 0.75 um and 2.16 um. The ambiguity is caused by the abrupt change in the scattering efficiency as the size parameter (i.e., $2 \pi r / \lambda$) transitions from the Mie region to the optical region. The only way to resolve this ambiguity is through a priori knowledge. For the present, it will be assumed that distributions with $r_e < 4$ are unrealistic or of very low probability and will not be considered. In the future, as more cloud scene types are tested, better a priori knowledge about potential r_e values, based on some regional, temporal, climatological factors, etc., should be available.

3.1.1.3 Retrieval of Optical Depth and Efective Radius from Thermal IR Wavelength Imagery (Nightime Retrievals)

As indicated in the introduction, an algorithm for retrieving cloud properties from thermal IR imagery is still under investigation. A comprehensive discussion of a potential approach currently being tested appears in Prabhakara et al. [1988]. A summary of that technique follows. At solar wavelengths scattering is the dominant radiative effect and the source of the radiation (i.e., the sun) for which this effect is measured, is from the same general direction that the sensor measurements are made. At thermal IR wavelengths absorption is the dominant radiative effect and the source of the radiation is from the background (e.g., the surface), atmospheric constituents, and/or cloud droplets/particles. To retrieve cloud properties at thermal IR wavelengths some relationship between the absorptive effects of different size distributions of droplets/particles and radiance must be established. In the 8-12 um region droplet/particle absorption is a function of wavelength wherein absorption increases with increasing wavelength (see Figure 2).

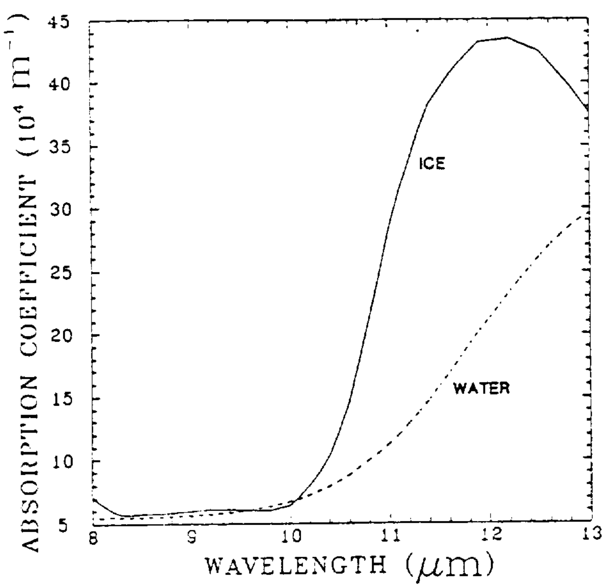

FIG. 2. The absorption coefficient of ice over the spectral range 8–13 μm.

Figure 2. Absorption coefficient of ice and water vs. wavelength. (From Ackerman et al. [1990].

If a cloud is sufficiently thin such that the radiance measured at the satellite sensor is comprised of contributions from both the cloud and the background (i.e., cloud emissivity < 1), then the difference in absorption of background radiation at different wavelengths can be used to estimate cloud droplet/particle size distribution and infer optical depth and effective radius. The effect is demonstrated in Figure 3a and 3b in which temperature difference at 2 wavelengths (i.e., 8.4 um and 11.7 um) is plotted against effective radius and optical depth. Each curve in Figure 3a indicates constant optical depth while each curve in Figure 3b indicates constant effective radius.

One can see that for optically thin regions significant temperature differences correspond to different effective radii. However, for optically thicker values cloud properties (i.e., effective radius) cannot be resolved. It appears at the present time that robust nightime retrieval of optical properties will not be feasible. For example, retrieval of microphysical properties for thin cirrus appears likely, whereas those for a thick stratiform deck do not.

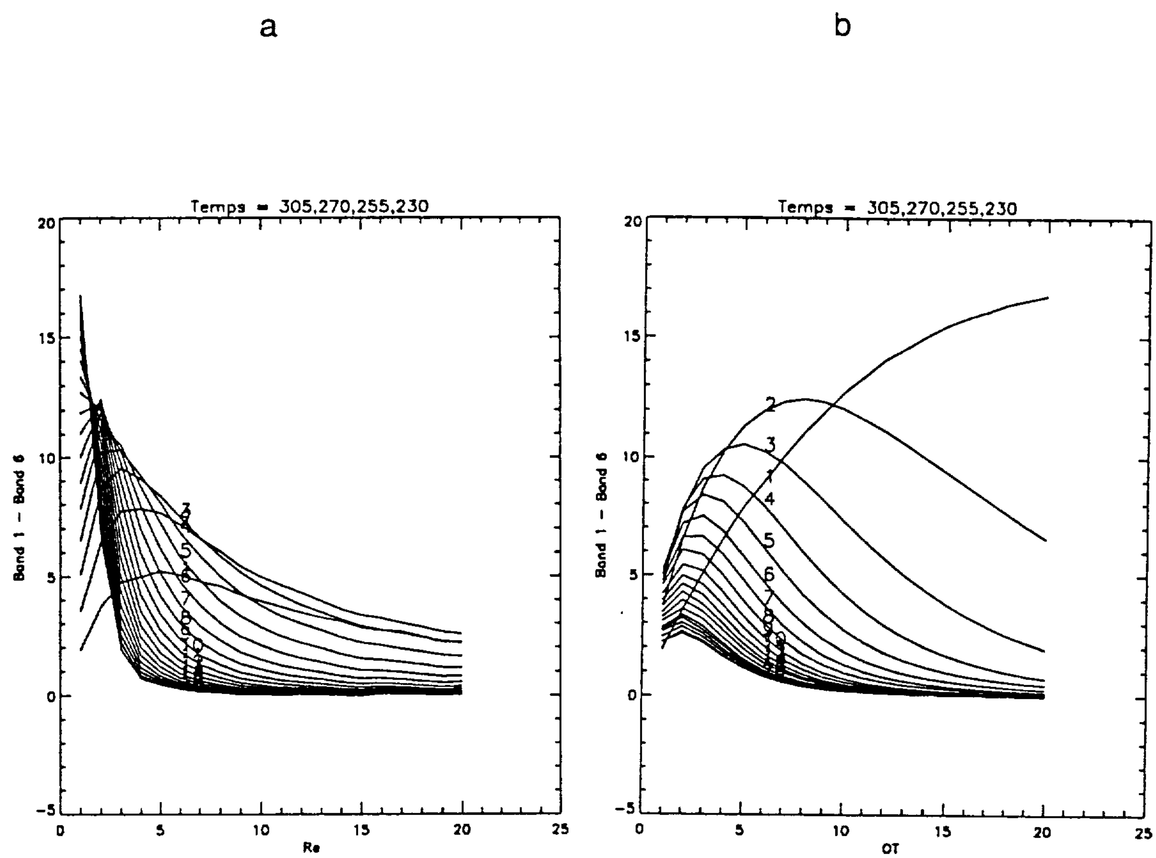

Figure 3. Temperature difference in 2 TIMS bands (8.4 um - 11.7 um) vs. (a) effective radius for 20 optical depths and (b) optical depth for 20 effective radii. Based on discrete ordinate radiative transfer model results for surface temperature of 305 deg K, cloud base temperature of 270 deg K, and cloud top temperature of 255 deg K.

3.1.1.4 Mie Scattering and Discrete Ordinate Radiative Transfer Models

A comprehensive discussion of the theory behind or the implementation of the Mie scattering and discrete ordinate radiative transfer models is much too complex and extensive to be included in this document. However, such discussions can be found in Diermendjian [1969], Stamnes and Dale [1981], Stamnes et al.[1988], Stamnes and Swanson [1981], Stamnes [1982], Stamnes and Conklin [1984], Lenoble [1985], and Wiscombe [1977]. The intent herein is to describe the application of their results in the retrieval of cloud microphysical properties and some of the inherent assumptions.

The Mie scattering model is used to determine the single scattering albedo and the phase function for an assumed droplet/particle size distribution. The size distribution

currently being used is the modified gamma distribution and is defined as follows:

$$n(r) = a\, r^{\alpha} \exp(-b\, r^{\gamma})$$

where,

r = droplet/particle size
a = scaling factor
b, α, γ = parameters that determine peakedness and kurtosis of the distribution
$n(r)$ = size distribution

Through appropriate choices of the **a**, α, and γ parameters, the modified gamma distribution can be tailored to fit most any reasonable size distribution. Currently α and γ are fixed at 2 and 4, respectively; however, in the future, as the algorithm is tested on a more diverse set of cloud scenes, it is expected that the selection of these parameters can be optimized for regional and/or climatological factors. The **a** parameter is used to scale the distribution so that a constant volumetric scattering coefficient is maintained over the entire range of optical depths being modeled and thereby making physical depth consistent among each of the size distributions. As currently configured, the Mie scattering model is only appropriate for modeling spherical droplets/particles. To date, this algorithm has only been tested on water clouds, an environment in which the spherical assumption is valid. However, the ice or mixed phase cloud environment is much more complex. Initially, when testing the algorithm on these types of clouds, as a first order approximation, equivalent spheres will be assumed. However, in the future, it should be possible to model scattering and absorption in ice/mixed phase clouds more accurately using a ray tracing model.

The discrete ordinate radiative transfer model provides estimates of cloud radiance vs. optical depth for the specific phase function and single scattering albedo computed by the Mie scattering model, at a given solar zenith angle, observation angle, and background albedo. The most important simplyfying assumptions in this model are that the clouds are plane parallel, the background albedo is uniform, and background scattering is Lambertian. These assumptions are valid for large scale stratiform decks that are more or less uniformly thick across their extent. However, in cumuliform clouds with significant 3-D structure or in broken clouds over a terrestrial background, 3-D cloud effects and/or highly variable background albedo alter the reflection function significantly from the modeled one. Three-D cloud effects include those due to cloud to cloud shadowing, variable solar zenith angle,

and cloud to cloud edge scattering. Currently, techniques are being investigated for detecting cloud regions in which model results are invalid so that retrievals from those regions can be flagged as suspect. However, current in-house efforts are directed at simulating 3-D cloud effects appropriately and in 2-3 years it should be possible to retrieve cloud properties adequately for most types of clouds and backgrounds.

Using the two aformentioned models, estimates of radiance are obtained for any selected size distribution, at any wavelength, solar zenith angle, observation zenith, background albedo, and optical depth. The effective radius and optical depth are then inferred for a multispectral set of radiance measurements associated with a specific pixel.

3.1.2 Mathematical Description of Algorithm - Daytime Retrievals

Before any cloud properties can be retrieved, an extensive set of lookup tables (see section 3.2.1) must be prepared for all possible combinations of wavelength (each band), solar zenith angle, observation angle, and background albedo, such that each table contains model reflectance values for all possible combinations of optical depth and effective radius for a specific band, solar zenith angle, observation angle, and background albedo. The lookup tables are then indexed by their corresponding band, solar zenith angle, observation angle, and background albedo. The solar zenith angle and observation angle are inputs provided by the platform navigation system. Background albedo is computed as the mean reflectance for non-cloud image pixels and is unique for each band.

For a set of measured multispectral reflectances (i.e., from ASTER bands 3, 4, 6, and 7), corresponding to a specific cloud pixel, the Euclidean distance between each spectral set of model reflectances (wherein each one corresponds to a specific optical depth and effective radius) and each measured reflectance, is computed as follows:

$$D(\tau, r_e) = \left(\sum_i \left(R_{m,i}^2 - R_{t,i}^2 \right) \right)^{0.5}$$

where,

$D(\tau, r_e)$ = Euclidean distance for a specific τ and r_e

$R_{m,i}$ = Measured reflectance in band i

$R_{t,i}$ = Table lookup value for model reflectance in band i

i = band number

The retrieved optical depth and effective radius then corresponds to the pair that

have the smallest Euclidean distance. The technique is demonstrated in Figure 4 using only 2 bands. The solid and dashed lines indicate model results for constant optical depth and effective radius. The points indicate measured reflectances from a stratocumulus over water cloud scene. The main clustering (and, consequently, minimum Euclidean distance) of measured values occurs around optical depth 11 and effective radius 8.

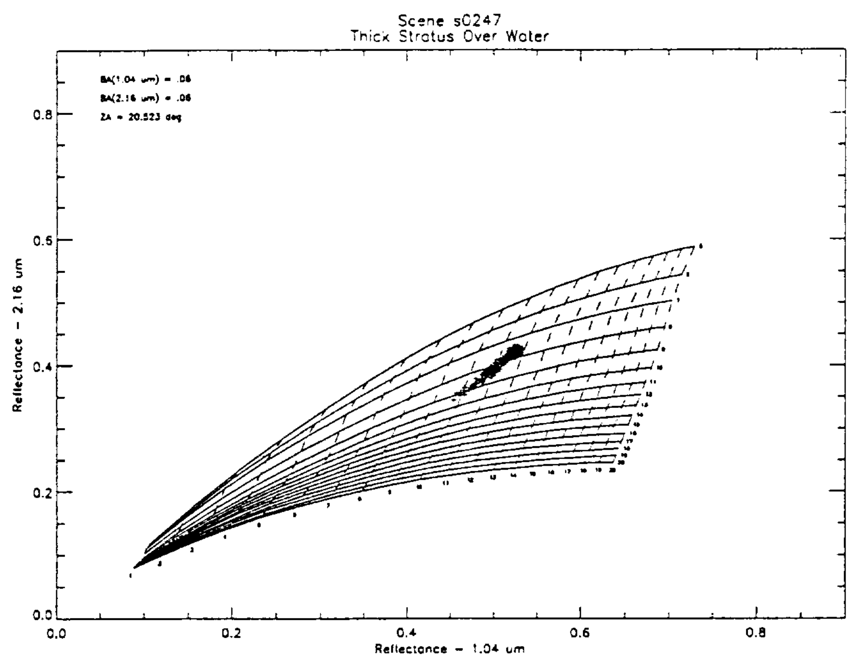

Figure 4. Reflectance at 2.16 um vs. 1.04 um for model and measured results. Solid and dashed lines indicate constant optical depth and effective radius, respectively. Points indicate measured reflectances from a stratocumulus cloud scene over water. The solar zenith angle is 20.5 degrees, the observation angle is 0 degrees, and the background albedo is 0.06.

As can be seen in Figure 4, the measured cloud reflectances cluster very nicely,

indicating a relatively uniform distribution of droplets. However, as suggested in section 3.1.1, 3-D cloud effects can manifest measured cloud reflectances which do not cluster nicely and, in fact, indicate unreasonable retrievals. This phenomena is demonstrated in Figure 5 for a fair weather cumulus cloud scene. Potential techniques for detecting this phenomena are addressed in section 3.2.4. Hopefully, as suggested in section 3.1.1, 3-D radiative models or compensating techniques will be available in the near future, so that this retrieval methodology will be more robust.

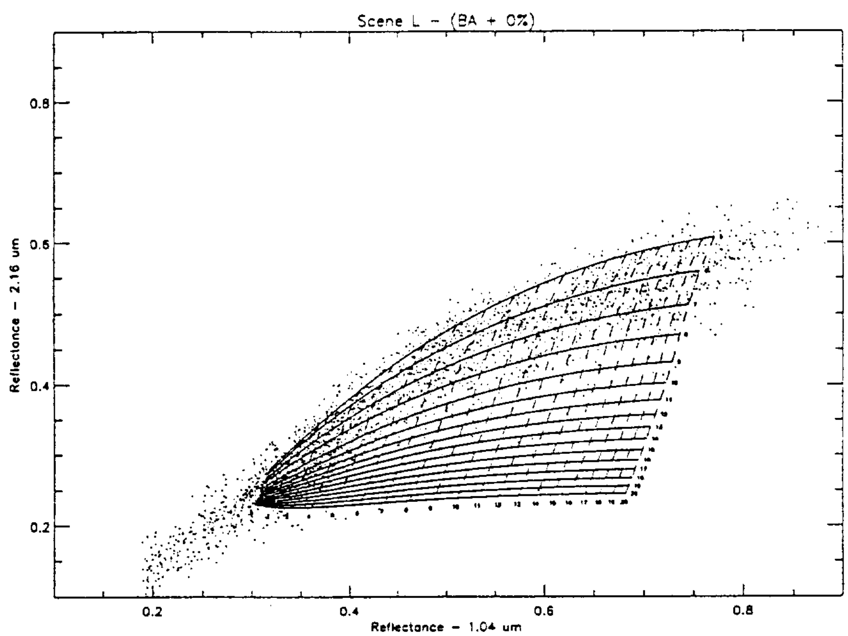

Figure 5. Reflectance at 2.16 um vs. 1.04 um for model and measured values. Solid and dashed lines indicate constant optical depth and effective radius, respectively. Points indicate measured reflectances from a fair weather cumulus over land cloud scene. The solar zenith angle is 19.3 degrees, the observation angle is 0 degrees, and the background albedo is 0.3.

A variation of this technique, suggested by Twomey and Cocks [1989], utilizes 0.75 um (e.g., ASTER band 3) and the ratio of near IR bands (e.g., ASTER bands 4, 6, and 7) to 0.75 um, is also being considered. It appears that this approach increases the orthogonality of optical depth and effective radius when optical depth is less than 12. The Euclidean distance for this technique is computed similarly and is represented mathematically as follows:

$$D(\tau, r_e) = \left((R_{m,1}^2 - R_{t,1}^2) + \sum_i \left((R_{m,i} / R_{m,1})^2 - (R_{t,i} / R_{t,1})^2 \right) \right)^{0.5}$$

where,

$D(\tau, r_e)$ = Euclidean distance for a specific τ and r_e

$R_{m,i}$ = Measured reflectance in band i

$R_{t,i}$ = Table lookup value for model reflectance in band i

i = band number

As before, the retrieved optical depth and effective radius correspond to the pair with the minimum Euclidean distance. The technique is demonstrated in Figure 6 using only 2 bands. The solid and dashed lines indicate model results for constant optical depth and effective radius. The points indicate measured reflectance at 0.75 um on the abscissa and the ratio of 2.16 um to 0.75 um on the ordinate.

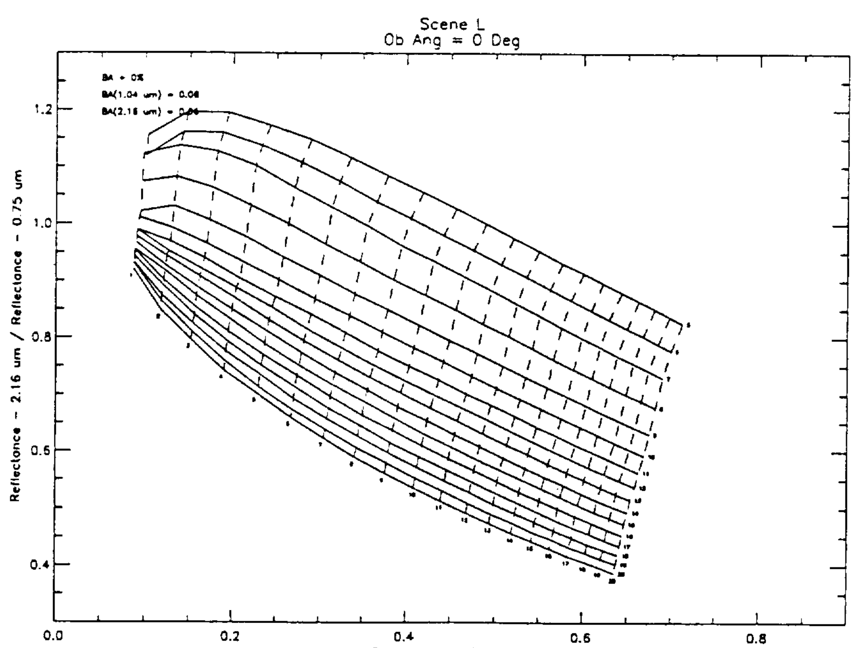

Figure 6. Ratio of reflectance at 2.16 um to 0.75 um vs. reflectance at 0.75 um for model results. Solid and dashed lines indicate constant optical depth and effective radius, respectively. The solar zenith angle is 20.5 degrees, the observation angle is 0 degrees, and the background albedo is 0.06.

Finally, LWC is derived directly using one of two methods. First, it can be computed by way of numerical integration of the basic mathematical definition (see section 3.1.1). The size distribution n (r) is inferred based on the gamma distribution assumption and the retrieved effective radius. Alternatively, if Q_e is assumed to be 2 (which valid for size parameters > 50 or $r_e > 5$ um), then the following mathematical formula is used:

$$LWC = \frac{2 \tau \rho r_e}{3 z}$$

where,

ρ = density of droplet/particle

z = physical depth (methodology for retrieving this property appears in another document)

3.2 Practical Considerations

3.2.1 Lookup Tables

Neither the Mie scattering model nor the discrete ordinate radiative transfer model is native to the algorithm for retrieving cloud properties. Both models are computationally intensive and algorithmically complex. The most efficient approach for finding optical depth and effective radius based on these 2 models is to compile, beforehand, extensive sets of tabulated values for reflectance vs. optical depth for numerous size distributions, wavelengths (e.g., bands 3, 4, 6, 7, 10, and 13 of ASTER), zenith angles, observation angles, and background albedos. The exact combinations for each one of these variables has yet to be determined. Sensitivity analyses need to be conducted first to determine an optimum set. The combinations of variables chosen will be such that lookup table errors will be at least an order of magnitude less than errors due uncertainties in the retrieval scheme (such as, errors due to modeling assumptions). However, as a rough approximation, if 20 values of optical depth are compiled for each of 20 size distributions, 10 zenith angles, 10 observation angles,10 background albedos, and 6 wavelengths, then the total number of tables required is 10 x 10 x 10 = 1,000. The total number of 4 byte floating point values stored in those tables is then 1,000 x 20 x 20 x 2 x 6 = 4,800,000 (or approximately 20 mbytes).

Although executing either one of these models will not be part of the day to day operations for retrieving cloud properties, a substantial effort is required to generate the tables initially and update them periodically, if necessary. It is not clear at this time how this is to be accomplished.

Aside from the numerical computations intrinsic to generating the table lookup values, the computational burden for this algorithm is small and numerical stability and round-off error are orders of magnitude smaller than any retrieved cloud property values.

The algorithm currently computes a Euclidean distance for each image pixel at every possible combination of optical depth and effective radius. The squared Euclidean distance and city block distance require less computation than the Euclidean distance are being investigated as alternative measures of distance.

3.2.2 Preprocessing Requirements

This retrieval methodology requires that the multispectral ASTER imagery has been preprocessed such that the radiance for each image pixel has been:

- identified as cloud/not cloud
- converted to reflectance and normalized for observation angle (solar wavelengths only)
- coregistered across all bands (i.e., VNIR, SWIR, and TIR)

It is critical that each pixel be coregistered across all 6 bands. The same pixel locations from bands within the same telescope (e.g., 6 and 7, or 10 and 13) should be coregistered to within 1 pixel. An array of 2 x 2 pixels in band 3 should be coregistered to within a single pixel in band 6 or 7. Likewise, an array of 2 x 2 pixels in band 6 or 7 should be coregistered to within 1 pixel in band 10 or 14. In addition, an array of 4 x 4 pixels in band 3 should be coregistered to within 1 pixel in band 10 or 14. In other words, the radiance measured in one band must correspond spatially to the radiance measured in any other band. Registration of the pixels to the Earth is only required to within a few hundred meters. Geolocations are not used in the computation of cloud properties but will potentially be used to augment size distribution selection, background albedo estimates, etc.

The following values, for each cloud pixel, are also required for these cloud property retrievals:

- solar zenith angle
- observation angle
- cloud physical depth (for LWC computations)

3.2.3 Calibration and Validation

Validation of cloud property retrievals is very difficult. Cloud microphysics are temporally and spatially very dynamic. It is logistically very difficult to obtain temporally and spatially coincident aircraft in situ measurements and satellite measurements. Even then, state of the art aircraft probes have their own set of problems and limit the veracity of their measurements. In addition, aircraft in situ measurements are obtained at a specific 3-D point location within a cloud while a satellite sensor obtains a spatially integrated measure (both vertically and horizontally) of microphysical effects. The validation or comparison is at best qualitative.

3.2.4 Quality Control and Diagnostics

Measures of the quality of the retrievals is currently under investigation. A wider variety of scene types need to be processed before these measures can be established. Some simple measures under consideration include setting bounds on, or performing contingency or hypothesis testing on retrieved values based on climatology, geolocation, spatial measures of smoothness or uniformity (such as statistical variance), etc.

Another measure under consideration is based on an extrapolation of the minimum distance criterion discussed in section 3.1.2. Up to 4 bands are used to simultaneously to retrieve optical depth and effective radius, wherein minimum Euclidean distance is the criterion for the solution. All combinations of 2 bands also can be used to determine a set of minimum Euclidean distances from which a variance could be computed. This variance is potentially a measure of the goodness of the retrieval.

3.2.5 Exception Handling

This methodology assumes that the preprocessing of the image data includes identification of cloud pixels and flagging of line dropouts. Cloud properties will not be retrieved for non-cloud pixels or line dropouts.

If some threshold for the quality of a retrieval (as to be defined in section 3.2.4) is exceeded, the retrieval wil be flagged as suspect.

4.0 Constraints, Limitations, Assumptions

Assumptions, and known constraints and limitations are described in section 3.

References

Ackerman, S. A., W. L. Smith, J. D. Spinhirne, and H. E. Revercomb, The 27-28 October 1986 FIRE Cirrus Case Study: Spectral Properties of Cirrus Clouds in the 8-12 um Window, Monthly Weather Review, 118, 2377-2388, 1990.

Diermendjian, D., Electromagnetic Scattering on Spherical Polydispersions, American Elsevier Publishing Company, New York, 260 pp., 1969.

Feind, R. E., R. M. Welch, S. A. Christopher, The Effect of Spatial Resolution Upon Cloud Optical Property Retrievals. Part I: Optical Thickness, J. Geophys. Res.-Atmos., in press.

King, M. D., Determination of Scaled Optical Thickness of Clouds from Reflected Solar Radiation Measurements, Journal of the Atmospheric Sciences, 44, 1734-1751, 1987.

Lenoble, J., ed., Radiative Transfer in Absorbing and Scattering Atmospheres: Standard Computational Procedures, Deepack Publishing, Hampton, VA, 1985.

Nakajima, T., M. D. King, and J. D. Spinhirne, Determination of the Optical Thickness and Effective Particle Radius of Clouds from Reflected Solar Radiation Measurements. Part II: Marine Stratocumulus Observations, Journal of the Atmospheric Sciences, 48, 728-750, 1991.

Stamnes, K., and H. Dale, New Look at the Discrete Ordinate Method for Radiative Transfer Calculations in Anisotropically Scattering Atmospheres. Part 2: Intensity Computations, J. Atmos. Sci., 38, 2696-2706, 1981.

Stamnes, K., S. C. Tsay, W. Wiscombe, and J. Jayaweera, A Numerically Stable Algorithm for Discrete-Ordinate-Method Radiative Transfer in Multiple Scattering and Emitting Layered Media, Appl. Opt., 27, 2502-2509, 1988.

Stamnes, K., and R. Swanson, A New Look at the Discrete Ordinate Method for Radiative Transfer Calculations in Anisotropically Scattering Atmospheres, J. Atmos. Sci., 38, 387-399, 1981.

Stamnes, K., On the Computation of Angular Distributions of Radiation in Planetary Atmospheres, J. Q. S. R. T., 28, 47-51, 1982.

Stamnes, K., Reflection and Transmission by a Vertically Inhomogeneous Planetary Atmosphere, Planet. Space Sci., 30, 727-732, 1982.

Stamnes, K., and P. Conklin, A New Multi-Layer Discrete Ordinate Method Approach to Radiative Transfer in Vertically Inhomogeneous Atmospheres, J. Q. S. R. T., 31, 273-282, 1984.

Twomey, S., and T. Cocks, Remote Sensing of Cloud Parameters from Spectral Reflectance in the Near-Infrared, Beitr. Phys. Atmosph., 62, 172-179, 1989.

Wielicki, B. A., and L. Parker, On the Determination of Cloud Cover from Satellite Sensors: The Effect of Sensor Spatial Resolution, J. Geophys. Res., 97, 12799-12823, 1992.

Wiscombe, W., The Delta-M Method: Rapid Yet Accurate Radiative Flux Calculations, J. Atmos. Sci., 34, 1408-1422, 1977.

Algorithm Theoretical Document

for the ASTER products:

Product #	Level	Product
1763	2C1	Cloud Phase
2080	2C1	Cloud Fractional Area

Version 1

December 1992

Team Member: Dr. Ronald Welch
IAS, South Dakota School of Mines and Technology

Table of Contents

1.0 Introduction

This document describes the theoretical basis for the fractional area and cloud phase algorithms. These ASTER products are:

EOS Product #	Level	Product name
2080	2C1	Fractional Area
1763	2C1	Cloud phase

These two products are produced as a result of the identification and classification of clouds for ASTER scenes. The classification algorithm is an interactive hybrid neural network and fuzzy expert system. Expert systems (ESs) and neural networks (NNs) are two different approaches to problem solving. Expert knowledge acquisition and an explanation facility to trace a conclusion are the main advantage of ESs. On the other hand, NNs have the capability of learning patterns whose complexity makes difficult to define expert system rules and to incorporate new characteristics without degrading any prior learning.

The hybrid system's knowledge base is based on spectral and features data derived from the data collected from the different channels of an instrument. Calibration of pixel brightness to albedos and to brightness temperatures are made according to the data collected from a particular instrument. The accurate cloud identification is crucial for the retrieval of the other ASTER cloud products which are described separately.

2.0 Overview and Background Information

Clouds are by far the most important modulators of radiative energy with the earth's atmosphere. The presence of clouds directly impact the spectral distribution of radiative energy at the top of the atmosphere. Reflection of solar radiation has a cooling effect on climate, whereas absorption of surface infrared radiation by clouds and re-emission to space at a lower cloud top temperature has a warming effect on climate.

Standard cloud retrieval algorithms typically rely on multispectral signatures. However, spectral signatures alone appear to be inadequate for polar scene identification [McGufiie et. al., 1988; Rossow et. al., 1988; Stowe et. al., 1989]. Combinations of spectral and textural signatures have been used successfully to classify clouds over various surfaces, including sea ice [Ebert, 1987, 1989; Key, 1990; Welch et. al., 1992; Rabindra et. al., 1992; Tovinkere, 1992]. A large number of textural features will be investigated, including the Gray Level Difference Vector (GLDV) Haralick et. al., 1973; Weszka et. al., 1976], and Sum and Difference Histogram (SADH) approaches, and spectral histogram measures. Principal component analysis of textural measures will be used to eliminate those measures which contribute little to class separability.

Artificial Intelligence (AI) increasingly is being used for classification [Key et. al., 1989,

Tovinkere, 1992]. Expert systems (ES) and neural networks (NN) are AI approaches to problem solving which have no predefined solution path; rather, the system uses its knowledge about the subject, along with the input, to define the procedure which determines the answer [Moninger, 1988; Peak and Tag, 1989]. The cloud-radiative interactions are not well understood. ES and NN are flexible enough to respond to our increased understanding of the cloud properties.

2.1 Expert Systems

ES perform inferences based upon collected expertise and a set of known facts. Problems are solved using deductive reasoning rather than by defined procedures. An essential ingredient of the ES is the ability to produce a result even with incomplete data. An ES consists of two main components: the knowledge base and the inference engine. The knowledge base consists of knowledge represented typically in the form of IF-conditions-THEN-action- rules that will be used by the inference engine to draw conclusions. An example of an IF-THEN rule is:

IF temperature is less than -32°C THEN Class Cirrus

Depending on the inference engine there are two basic type of ES: data-driven and goal-driven [Luger, 1989]. In data-driven ESs, most of the data for the problem are initially given and the inference uses a forward reasoning, starting from facts and reaching a final conclusion. In goal-driven ESs, the systems work backward from an original hypothesis or goal to facts or subgoals satisfying the original hypothesis. In the latter type of ESs, subgoals are satisfied by asking the user for facts.

2.1.1 Uncertainties in Expert Systems

Some degree of uncertainty can be incorporated in the rules whenever there exist some unreliable data or there is a need for assigning some degree of confidence to a conclusion. For example, assigning a confidence of 0.9 to the above rule will represent either the case that the instrument that measures the temperature is not always correct or that we are not completely sure about the conclusion. The above rule having a 0.9 confidence level may be expressed as:

IF temperature is less than -32°C THEN Class Cirrus (0.9)

2.1.2 Fuzzy logic

Another approach to modeling uncertainty is by using fuzzy logic. Using the above rule, fuzzy logic deals with situations on which some uncertainty is assigned to the rule based on the value of the temperature rather than in the logical value of the condition. Suppose the temperature is -28°C, the condition "temperature > -32°C" is false, therefore the above rule is not satisfied. That is, in classical logic, the value of temperature determines that the cloud being sampled is a member of the set of

cirrus clouds or not. In the case of fuzzy logic, there is some degree of membership associated with the conclusion based on the condition variables. In the case of a temperature of -28°C, the membership function for the class Cirrus might generate a membership value of 0.95. In classical logic, the degree of membership of a cloud in the set of cirrus clouds is represented by the set {0,1}. In fuzzy logic, the degree of membership of a cloud within the set of cirrus clouds is represented by the range [0,1]. The above rule is a fuzzy rule whenever the fuzzy variable "temperature" in the fuzzy condition or fuzzy predicate is represented by a membership function. The term linguistic variable is also used instead of fuzzy variable. A linguistic variable may be expressed by several terms, each one with an associated membership function. Suppose that temperature could be expressed by the terms: "very low", "low", "medium", "high", and "very high". The membership functions for these terms are shown in figure 1.

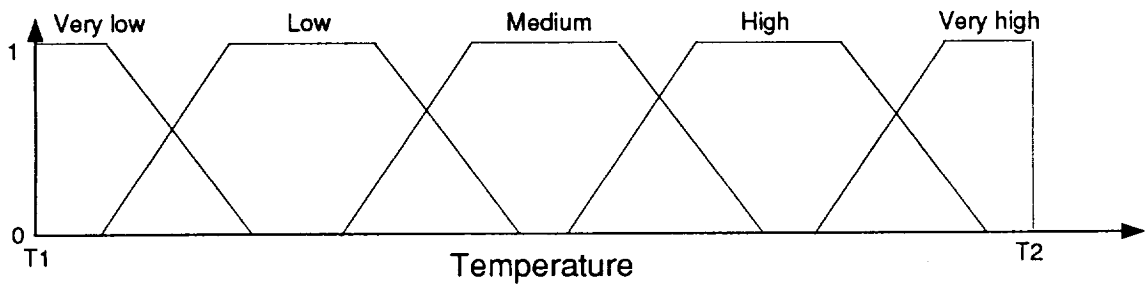

Figure 1. Set of membership functions for temperature terms

Fuzzy logic is concerned with formal principles of approximate reasoning; i.e., it aims at modeling imprecise modes of reasoning to make decisions in an environment of uncertainty. The greater expressive power of fuzzy logic derives from the fact that it contains, as special cases, not only the classical two-valued and multivalued logical systems but also probability theory and probabilistic logic. The main features of fuzzy logic that differentiate it from traditional logical systems are the following:

1. In two-valued logic, a condition or proposition p is either true or false. In multivalued logic, may have several truth values, including true and false. In fuzzy logic, truth values are allowed to be within the range [0,1], where 0(1) is false(true).
2. Two-valued and multivalued logics allow only two quantifiers: "all" and "some". By contrast, fuzzy logic allows in addition, the use of fuzzy quantifiers exemplified by "most", "many", "several", and so on. Fuzzy quantifiers may be viewed as a second-order fuzzy predicate.

2.2 Neural Networks

Neural networks learn and generate solutions to problems that are difficult to define and solve using formal approach. NN have the ability to learn new features and facts without degrading the prior learning [Lee et. al., 1990].

A NN consists of objects called nodes and weighted paths connecting those nodes. Each node has an activity represented by a real number. This activity value is computed as a non-linear bounded

monotone increasing function of a weighted sum of the activities of other nodes that are directly connected to it.

The NN has three or more processing layers: an input layer, several hidden layers, and an output layer. The activity on a node K is denoted by V_K, and the weight on a path from node L to node K is denoted by W_{KL}. Then

$$V_K = f\left(\sum_L W_{KL} V_L\right)$$

where f is a nonlinear function.

The determination of the appropriate weights W_{KL} is referred to as learning. Learning algorithms may be classified as supervised or unsupervised. A neural network may be viewed as a nonlinear vector-valued function:

$$\mathbf{O} = \mathbf{F}(\mathbf{I})$$

where **O** is a vector with one component for each activity of an output node, and **I** is a vector with one component for the activity for each input node. In the supervised learning mode, for each possible input vector **I**, an associated output vector **O** is specified. The function of the learning algorithm is to choose the value of the weights so that **F(I)** is a good approximation of **O** [Lee et. al., 1990].

There exists several types of NNs depending on the topology of the network. Figure 2 shows a three-layer feed forward back propagation NN. In this network the paths form a loop-free directed graph. Back propagation [Rumelhart et. al., 1986] refers to the process of iteratively determining the weights W_{KL} that locally minimize the global error E:

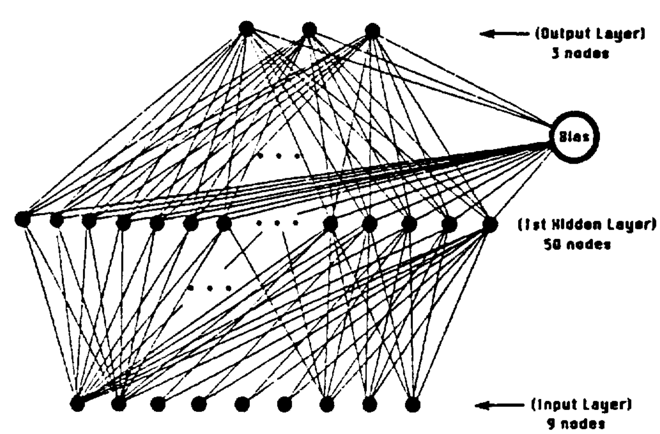

Figure 2. A feed forward neural network

The algorithm is a special case of gradient search in which the weights are initialized as small random numbers and are repeatedly updated at the nth iteration according to the rule

$$\Delta \mathbf{W} = - \eta \nabla \mathbf{E} , \quad \mathbf{W}_{n+1} = \mathbf{W}_n + \Delta \mathbf{W} ,$$

where **W** is a vector composed of the weights, ∇**E** is the gradient of the global error, and n is the learning rate. Additional details are given by Lee [Lee et. al., 1990] and Hecht-Nielsen [Hecht-N ielsen, 1990].

Traditional parametric classification schemes are constructed using linear hyperplanes. On the other hand, the NN approach consists of treating those hyperplanes as nonlinear rubber sheets. For example, the hidden layer in a NN serves to provide the "bending" of the sheet. Addition of a second hidden layer allows higher order deformations of the hyperplanes. It is this capability that allows the NNs to outperform the traditional, linear, parametric approaches. Other types of neural networks are: a) the probabilistic NN, b) hybrid NN, c) "don't care" perceptron, and d) "don't care" feed forward back propagation NN [Tovinkere et. al., 1992].

3.0 Algorithm Description

The cloud classification algorithms will be implemented by a hybrid system consisting of an ES and a NN. Our initial alternative consists in using concurrently both artificial intelligence approaches, and the output from the ES will be compared against the output from the NN. The NN will serve as a feedback to the ES. A significant difference between these two approaches will indicate that the rules need to evolve or tune due to global change processes. The next subsections will describe in detail the data, features, classes, region labeling, the fuzzy ES and the type of NN used for the classification.

3.1 Data

Initially, the hybrid system will be trained and tested using Advanced Very High Resolution Radiometer. (AVHRR) Local Area Coverage (LAC). For the case of AVHRR data the albedos are normalized by the cosine of the solar zenith angle at each pixel and then scaled to gray level 0-255, representing 0% - 100% respectively. The normalized albedo ρ3 in channel 3, which contains both reflected solar and emitted thermal radiation, is computed as

$$\rho_3 = (I_3 - B_3(T_4)) / [F_3 \cos \Theta_0 - B_3(T_4)] \cos \Theta_0$$

where I_3 is the pixel radiance in channel 3, $B_3(T_4)$ is the blackbody radiance in channel 3 evaluated from the brightness temperature of channel 4, F_3 is the incidence solar irradiance in channel 3, and Θ_0 is the local solar zenith angle. Note that this is only a rough approximation to the true channel 3 albedo and does not account for bidirectional reflectance.

3.2 Region Labeling

Each image is divided into numerous 32x32 pixel subregions for classification. At nadir, these subregions are approximately 35km x 35km in extent. Spectral and textural measures are computed for each of these regions for use as features. For accurate classification, an expert selects several regions as the trained data using an interactive visual image classification system (IVICS) which displays three-band color overlays [Berendes and Welch, 1993]. The red color displays the thermal channel 4, which is gray flipped so that colder portions of the image are brighter red; the blue color displays channel 1; and the green color displays channel 3. IVICS includes a series of pull-down menus which allow a wide variety of channel displays and image processing functions.

3.3 Features and Classes

Several textural and spectral measures are used for classification. The selection of these textural and spectral features will be based on the Sequential Forward Selection (SFS) procedures; SFS is a simple bottom-up search procedure where one measurement at a time is added to the current feature set. The textural features are computed using the Gray Level Difference Vector (GLDV) approach [Haralick et. al., 1973, Weszka et. al., 1976]. This method has been shown to produce reliable textural measures, and requires less storage and CPU time than other techniques [Welch et. al, 1988, 1990; Kuo et. al., 1988; Chen et. al., 1989]. The GLDV method is based upon the absolute differences between pairs of gray levels I and J found at a distance d apart at a fixed angle ϕ. The difference vector probability density function $P(m)_{d,\phi}$ is defined for m=I-J; it is obtained by normalizing the gray level frequencies of occurrence by the total number of values using the density function. The following textural measures will be used:

angular second moment : $\mathrm{ASM} = \sum_m P(m)^2_{d,\phi}$

entropy : $\mathrm{ENT} = -\sum_m P(m)_{d,\phi} \log P(m)_{d,\phi}$

Among others, the following spectral and textures measures will be used in the classification:

Alb1 - Alb2	The albedo difference between channels 1 and 2.
Low 3	The percentage of pixels in channel 3 that have an albedo less than 10%.
Mean ASM3	Mean of the angular second moment of channel 3.
Mean1	Mean albedo of channel 1.
Max Ent4	Entropy measure of the region in channel 4.

The mean and standard deviations are computed for the complete training data set. The feature vectors from an image being classified will be facts that will input to both, the NN and the ES.

3.4 Fuzzy Expert System

Initially, the fuzzy logic ES uses the C Language Integrated Production System (CLIPS) ES shell to build the ES. In the prototype we expect to implement a fuzzy ES shell. CLIPS is a forward chaining rule-based language that has inferencing and representation characteristics. Forward chaining inferencing is reasoning from facts to conclusions resulting from these facts. Functions to allow fuzzy sets are added to the CLIPS code. The number of rules depends on the number of features and the number of classes. Each feature associated with each class is represented by a fuzzy membership function. Each feature distribution closely approximates a Gaussian distribution. Therefore, the Π-function is used to represent the fuzzy sets. Other functions will be investigated, including a multi-dimensional gaussian distribution. The Π-function is defined as follows:

$$\Pi(x;\beta,\gamma) \Rightarrow \begin{cases} S(x;\gamma-\beta,\gamma-\beta/2,\gamma) & \text{for } x \le \gamma \\ 1 - S(x;\gamma,\gamma+\beta/2,\gamma+\beta) & \text{for } x \ge \gamma \end{cases}$$

Where S is the S-function. The S-function is defined as follows:

$$S(x;\alpha,\beta,\gamma) \Rightarrow \begin{cases} 0 & \text{for } x \le \alpha \\ 2\left(\dfrac{x-\alpha}{\gamma-\alpha}\right)^2 & \text{for } \alpha \le x \le \beta \\ 1-2\left(\dfrac{x-\gamma}{\gamma-\alpha}\right)^2 & \text{for } \beta \le x \le \gamma \\ 1 & \text{for } x \ge \gamma \end{cases}$$

The main program of the expert system reads in the file positions of the training samples and generates the feature set for all the samples. The means and standard deviations of all the features for each class are calculated. Finally the program generates the CLIPS rules which can be run on the expert system shell. This process is completely automated and does not require any user intervention. However, the input data files to the program must be in a particular format. Once the CLIPS rules are generated, the system is trained for future use. The fuzzy functions of the expert system must be tuned to produce accurate results. This step will involve a) to try the system with different shapes of fuzzy functions, and b) to select representative samples in the training set.

The expert system is divided into three phases:

- Initialization phase: In this phase, the fuzzy sets are defined. The member of the fuzzy sets are formed from the means and the standard deviations of the feature for all classes.

- Decision phase: This phase loads the feature vector for the selected sample. The values of each feature are evaluated by the corresponding fuzzy sets, and the membership values of all the class functions in the fuzzy set fro that feature are loaded into the working memory of the ES. These facts fire a rule depending upon the closest class.
- Cleanup and result phase: In this phase, the membership strengths of each class are normalized to give an estimate of how much of a class or of several classes are present in a sample.

3.5 Neural Network

The type of neural network for cloud classification will be the "don't care" back propagation NN. This network provides the best results for classification [Tovinkere et. al., 1992]. The decision surfaces are nonlinear, as in all NNs. However, a "don't care" NN only requires pairwise linear separability, rather than true linear separability.

By analogy with the technique employed in simplifying combinational logic circuits, the value of the linear function separating classes C_i and C_j is specified as "don't care" (x) on all other classes. For an acceptable "don't care" encoding, it is only necessary that no output vector belong to two distinct classes and that every output belongs to one of the classes encodings. Given N pairwise separable classes, C_i, i=1,2, ..., N, there are N(N-1)/2 separating hyperplanes. These are denoted as C_1/C_2, C_2/C_3,, ..., C_{N-1}/C_N. For any class C_m,, the linear function corresponding to the separating hyperplane C_i/C_k, will have a value of 1 if m=i, 0 if m=k, and X "don't care" otherwise.

To couple the "don't care" encoding to back propagation requires only one simple modification. Normally, the error at the output is taken to be the difference between the desired value of the output node and its computed value. In a "don't care" back propagation NN, this rule for a given input vector applies only to those output nodes whose encoding is determinant, and is taken as zero for "don't care" outputs. The number of input nodes is equal to the number of spectral and textural features, the number of hidden layers depends on the number of classes, and the number of output nodes is N(N-1)/2, where N is the number of classes.

The training of the network proceeds as follows:

1) Desired outputs are defined for each class.
2) Patterns are presented to the network and the error is calculated.
3) The weight updates are calculated for connections between the inputs and outputs which do not have "don't care" outputs.

The network processing is divided into three phases:

- Initialization phase. It consists of setting all node values to zero, and all weights are randomized between set values.
- Training phase. It is done as explained above.
- Recall phase. After the network is trained, the recall phase is initiated by running the data from the samples.

3.6 Pseudo code

The high-level pseudocode for running the hybrid system is as follows:

```
Select training samples
Compute features
Select features and classes
While there are more samples to classify do
parbegin                              /* Do concurrently
   Initialize neural network
   Initialize expert system
   Train the neural network
   Load feature vector in the expert system
   Execute recall phase of the neural network
   Perform result phase of the expert system
parend
Compute difference between both, neural network and expert system
If significant difference exits
then
  Determine if the expert system must be tuned
Endif
Save result in the database
```

4.0 Constraints, Limitations, Assumptions

One of the limitation to the system is the unavailability of real data from the ASTER instruments. A solution to this problem would be to generate prototype or simulated ASTER data. Beside AVHRR, we will use extensive use of other datasets such as the AVIRIS data, for simulating ITIR, VNIR, and SWIR channels. Post-launch tuning will be required in order to generate accurate cloud and sea ice products.

References:

Berendes, Todd A, and R. M. Welch, 1993: Interactive Visual Image Classification System (IVICS). *Ninth Intl. Conf. on Interactive Information and Processing System for Meteorology, Oceanography and Hydrology*, 73rd AMS Annual Meeting, 17-22 Jan. 1993, Anaheim, CA.

Chen, D. W., S. K. Sengupta, and R. M. Welch, 1989: Cloud field classification based upon high spatial resolution textural features, Part 2: Simplified vector approaches, J. Geophys. Res., 94, 14749-14765.

Ebert, E., 1987: A pattern recognition technique for distinguishing surface and cloud types in the polar regions, *J. Clim. Appl. Meteor.*, 26, 1412-1427.

Ebert, E., 1989: Analysis of polar clouds from satellite imagery using pattern recognition and a sta-

tistical cloud analysis scheme, *J. Appl. Meteor.*, 28, 382-399.

Glover, C. W., M. Silliman, M. Walker, and P. Spelt, 1990: Hibrid neural network and rule-based pattern recognition system capable of self-modification. *Applications of Artificial Intelligence VIII*, SPIE Vol. 1293, 290-299.

Haralick, R. M., K. S. Shammugam, and I. Dinstein, 1973: Textural features for image classification, *IEEE Trans. on Systems, Man, and Cybernetics*, vol. SMC-3, No. 6, 610-621.

Hecht-Nielsen, R., 1990: *Neurocomputing*, Addison-Wesley, Reading, MA, 430 pp.

Key, J., J. A. Maslanik, and A. J. Schweiger, 1989: Classification of merged AVHRR and SMMR artic data with neural networks, *Photogram Eng. Rem. Sens.*, 55, 1331-1338.

Key, J., 1990: Cloud cover analysis with artic AVHRR data, Part II: Classification with spectral and textural measures, *J. Geophys. Res.*, 95, 7661-7675.

Kuo, K-S, R. M. Welch, and S. K. Sengupta, 1988: Structural and textural characteristics of cirrus clouds observed using high spatial resolution LANDSAT imagery, J. Appl. Meteor., 27, 1242-1260.

Lee, J, R. Weger, S. K. Sengupta, and R. M. Welch, 1990: A neural network approach to cloud classification, *IEEE Trans. Geosci. and Remote Sensing*, 28, 846-855.

Luger, George and William Stubblefield, 1989: *Artificial Intelligence and the Design of Expert Systems*. Benjamin Cummings Publishing Company, Inc., 660 pp.

McGuffie, K., R. G. Barry, A. Schweiger, D. A. Robinson, and J. Newell, 1988: Intercomparison of satellite derived cloud analyses for the artic ocean in Spring and Summer, *Inter. J. Rem. Sens.* 9, 447-467.

Moninger, W. R., 1988: ARCHER: A prototype expert system for identifying some meteorological phenomena, J. Atmos. Ocean Tech., 5, 144-148.

Peak, J. E., and P. M. Tag, 1989: An expert system approach for prediction of maritime visibility obscuration, *Mon. Wea. Rev.*, 117, 2641-2653.

Rabindra P, S. K. Sengupta, and R. M. Welch, 1992: An interactive hybrid expert system for polar cloud and surface classification. *Environmetrics*, 3(2), 121-148.

Rossow, W. B., L. C. Gardner, and A. A. Lacis, 1988: Global, seasonal cloud variations from satellite radiance measurements. Part I: Sensitivity of analysis, *J. Climate*, 2, 419-458.

Rumelhart, D., G. Hinton, and R. Williams, 1986: Learning internal representations by error propagation, *in Parallel Distributed Processing: Exploration in the Microstructure of Cognition*, D. Rumelhart and J. McCelland, eds., MIT Press, 318-362.

Stowe, L. L., H. Y. M. Yeh, T. F. Eck, C. G. Wellemeyer, H. L. Kyle, and the Nimbus-7 Cloud Data Processing Team, 1989: Nimbus-7 global cloud climatology, Part I: First-year results, *J. Climate*, 2, 671-709.

Tovinkere, V. R., 1992: *Fuzzy Logic Expert System for Classification of Polar Regions*, M.S. Thesis, Department of Mathematics and Computer Science, South Dakota School of Mines and Technology, Rapid City, SD, 69 pp.

Tovinkere, V. R., M. Penaloza, A. Logar, J. Lee, R. C. Weger, T. A. Berendes, and R. M. Welch, 1992: An intercomparison of artificial intelligence approaches for polar scene identification. *J. Geophys. Res. - Atmospheres* [Accepted for publication].

Welch, R. M., S. K. Sengupta, and D. W. Chen, 1988: Cloud field classification based upon high spatial resolution textural features. Part I: Gray level cooccurrence matrix approach, J. Geophys. Res., 93, 12663-12681.

Welch, R. M., S. K. Sengupta, A. K. Gorock, P. Rabindra, N. Rangaraj, and M. S. Navar, 1992: Polar

cloud and surface classification using AVHRR imagery: An intercomparison of methods, *J. Appl. Meteor.*, 31, 405-420.

Weszka, J. S., C. R. Dyer, and A. Rosenfeld, 1976: A comparative study of texture measures for terrain classification, IEEE Trans. on Systems, Man, and Cybernetics, vol. SMC-6, No. 4, 2269-2285.

Algorithm Theoretical Document

for the ASTER product:

Product Number	Product
3152	Sea ice fractional area
3616	Meltpond fractional area
3617	Lead fractional area
3618	New ice fractional area
3619	Polar sea ice temperature
3620	Polar sea surface temperature
3621	Sea ice size distribution
3627	Lead size distribution

Version 1.0

December 1992

Team member: Dr. Ronald Welch[1]

[1]IAS, South Dakota School of Mines & Technology

TABLE OF CONTENTS

ALGORITHM THEORETICAL BASIS DOCUMENT OUTLINE

Date: 12/28/92

1.0 Introduction

This document describes the theoretical basis for algorithms to retrieve sea ice parameters such as sea ice fractional area, meltpond fractional area, lead fractional area, new ice fractional area, sea ice temperature, sea surface temperature, sea ice size distribution and lead size distribution.

The product numbers and levels are:

Level	EOS Product #	ATBD #	Product
2C2	3152	AT-06	Sea ice fractional area
2C2	3616	AT-06	Meltpond fractional area
2C2	3617	AT-06	Lead fractional area
2C2	3618	AT-06	New ice fractional area
2C2	3619	AT-06	Polar sea ice temperature
2C2	3620	AT-06	Polar sea surface temperature
2C2	3621	AT-06	Sea ice size distribution
2C2	3627	AT-06	Lead size distribution

This sea ice package retrieves sea ice parameters from satellite imageries for the polar region. It has four main phases:

(1) Image Preprocessing — use morphological operations (opening and closing) to remove small regions and smooth the imagery, then construct texture features (GLDV approach) for the image.

(2) Segmentation — use combinations of spectral and textural measures to classify and segment polar scenes into meaningful regions by region growing approach.

(3) Feature Identification — exam and identify each region into a possible feature (cloud, ice floes, meltpond, lead, open water, land.......) according to the difference of physical properties, textural characteristics, shape....etc..

(4) Computation of Sea Ice Parameters — pull out the feature of interest from the polar scene and compute the statistics (fractional area, temperature, size distribution) needed.

2.0 Overview and Background

2.1 Experimental Objectives

With the growing awareness of ozone depletion in the stratosphere and potential global climate change, the polar regions are receiving increased attention. Indeed, greenhouse forcing due to projected increases in co2 are expected to be amplified in the polar regions (Wetherald and Manabe 1986, Schlesinger and Mitchell 1987, Steffen and Lewis 1988). Furthermore, associated increases in atmospheric humidity can be expected to alter global cloud distribution. This sea ice package is designed for the purpose of providing an automated method to retrieve information such as sea ice fractional area, sea ice size distribution, new ice fractional area, meltpond fractional area, lead fractional area....etc. The outputs of this package therefore can be used to monitor changes in surface features at polar region.

2.2 Historical Perspective

Part of this package (image preprocessing and segmentation) has been used to obtain a intermedin result (segmented image) using LANDSAT TM imageries, and one paper titled with "Segmentation of Polar Scenes Using Multispectral Texture Measures and Morphological Filtering" has been submitted to journal.

2.3 Instrument Characteristics

Both visible and thermal channels are able to provide significant distinguish between polar surface features. For example, the meltpond regions can be identified from their lower albedos (VIS bands) and changes in temperature (IR bands) from that of surrounding regions. However, once the scene has been segmented into water, sea ice, meltpond, new ice, lead...etc, it is necessary to use thermal bands to determine sea ice temperature or sea surface temperature.

3.0 Algorithm Description

The following sections describe the sea ice parameter algorithms. The algorithms discussed here are of preliminary nature therefore are subjective to refinements and modifications. This section contains the following topics:

- 3.1 Theoretical Description
  - 3.1.1 Image Preprocessing
  - 3.1.2 Segmentation
  - 3.1.3 Feature Identification
  - 3.1.4 Computation of Sea Ice Parameters
  - 3.1.5 Uncertainties

3.1 Theoretical Description

In this section, A detail theoretical description about this algorithm is discussed. There are four main phases to retrieve sea ice parameters from satellite imageries as shown in Figure 1 and are discussed in the following subsections. Besides, an uncertainty analysis is also given at the end of this section.

3.1.1 Image Preprocessing

Image preprocessing step is first performed to prepare the image data for further processing. It contains three parts: (1) Apply morphological filtering to smooth the image. (2) Construct the texture features to gain textural information. (3) Perform correlation analysis to select features which provide best information for segmentation.

3.1.1.1 Morphological Filtering

Morphology refers to the form and structure in an image. The formal mathematical analysis of morphology is based upon Minkowski algebra (Serra 1982, Giardina and Dougherty 1988). The most useful morphological operations for image processing are: erosion, dilation, opening and closing.

The erosion operation is the Minkowski subtraction of the rotated structuring element B from a region A. The eroded image consists of all pixels in which the rotated structuring element fits inside the region. It is based upon the intersection of A and B. In contrast, the dilation operation is based upon Minkowski addition, or the union of A and B. Opening is defined as erosion of A by structuring element B followed by dilation of the eroded region by B. The net result of the opening operator is that small regions of size equal to or smaller than the structuring element are removed from the image. This allows us to eliminates small clouds and ice floes from the segmentation. Finally, the closing operation is the dilation of region A by structuring element B followed by erosion of the dilated region by B. This process joins neighboring regions such as those ragged edges found at the borders of large cloud masses.

Common structuring elements are 3x3 masks. In order to eliminate larger objects using the opening operator, a larger structuring element (5x5, 7x7...) may be needed. Good examples of these morphological operations were given by Schalkoff(1989).

A major limitation of the previous operations is they are based upon binary images. In order to retain the spectral information for segmentation, A grey-scale morphology must be applied (Serra 1982, Giardina and Dougherty 1988). In this case, 1 3x3x3 structuring element is needed: the x- and y- coordinates and grey level for the z- coordinate. However, these are complex and CPU intensive operations. We have found the following simplification produces equivalent results. For erosion, the 3x3 structuring element is moved over the image. The minimum grey level in the mask replaces the center element. For dilation, it is the maximum grey level in the mask that replaces the center element. These operations act as smoothing and edge enhancement procedures (Hsiao and Sawchuk 1989, Moran 1990) without the need for any form of thresholding.

3.1.1.2 Construction of Texture Features

Texture is often interpreted in the literature as a set of statistical measures of spatial distribution of grey levels in an image. Here, it is assumed that texture information is contained in the average spatial relationships that grey levels have with one another (Haralick et al. 1973). The GLDV (Grey Level Difference Vector) approach is based on the absolute differences between pairs of grey levels found at a distance d apart at angle ϕ with a fixed direction. The difference-vector probability density function $p(m)d,\phi$ is defined for $m = I - J$, where I and J are the corresponding grey levels, and is obtained by normalizing the grey level frequencies of occurrence by the total frequencies. From this density function, the following textural measures are computed:

mean

$$\mu_{d,\phi} = \sum_m m\, P(m)_{d,\phi}$$

standard deviation

$$\sigma_{d,\phi} = [\sum_m (m - \mu_{d,\phi})^2\, P(m)_{d,\phi}]^{1/2}$$

contrast

$$CON_{d,\phi} = \sum_m m^2\, P(m)_{d,\phi}$$

angular second moment

$$ASM_{d,\phi} = \sum_m [\, P(m)_{d,\phi}\,]^2$$

entropy

$$ENT_{d,\phi} = -\sum_m P(m)_{d,\phi} \log P(m)_{d,\phi}$$

local homogeneity

$$HOM_{d,\phi} = \sum_{m} [P(m)_{d,\phi}/(1 + m^{2)}]$$

3.1.1.3 Correlation Analysis

These texture measures are computed for each channel of an image. In order to eliminate redundant information from those texture measures and to reduce computation, a correlation analysis applied to several different polar scenes shows that ASM and HOM are correlated to each other with the correlation > 0.75 and others (σ, ENT and CON) are similarly correlated with the correlation > 0.75 (note that these analysis were applied to LANDSAT TM data). Anyway, the idea here is to eliminate highly correlated texture measures to reduce computation. A secondly correlation analysis may be applied to select best channels with selected texture measures if necessary. The correlation between 2 images (i and j) is computed as following:

$$CORR_{i,j} = \frac{COV_{i,j}}{\sigma_j \, \sigma_i}$$

where σ_i is the standard deviation for image i,

$$\sigma_i = \left\{ \frac{\sum_{k=1}^{N} (G_{i,k} - \mu_i)^2}{N - 1} \right\}^{1/2}$$

$COV_{i,j}$ is the covariance between image i and j,

$$COV_{i,j} = \frac{\sum_{k=1}^{N} (G_{i,k} - \mu_i) (G_{j,k} - \mu_j)}{N - 1}$$

and N is the total pixel number, $G_{i,k}$ is the grey level value for pixel k in image i and μ_i is the mean grey level value for image i.

3.1.2 Segmentation

The segmentation procedure attempts to find regions of distinct characteristics. This problem may be approached using a wide variety of methods (Keller el al. 1989, Taylor et al. 1989, Ohlander et al. 1978....). The most common segmentation approaches include region growing (Levine and Shaheen 1978), split and merge (Laprade 1988), and multiple resolution

(Bouman and Liu 1991)......and so on. Here, we use a modified region growing approach using combinations of spectral and textural measures. More different segmentation techniques might be added into this section later.

Meurle and Allen (1968) were the first to suggest region merging. They defined a region as an area of an image in which the statistical distribution of grey levels is reasonably uniform. Levine and Shaheen (1978) extended this approach by considering pixel merging in a "raster-scan" mode. Starting from the upper left-hand corner, pixel by pixel, row by row is processed until the bottom right-hand corner is reached. This one-pass segmentation process used a predicate 'P' based upon comparison of the given pixel with each of its neighboring regions (proximity) in the test for similarity. The test pixel was merged with the adjacent region to which it was most similar. If the pixel did not satisfy the predicate with any of the neighboring regions, then the pixel starts a new region. Once the pixel was merged with a region, the probability density function for the region was updated.

Levine and Shaheen suggested that the difference between the pixel intensity and the average intensity over the region be used as an adaptive threshold based method of similarity testing. In this way, as the region becomes less uniform, the growth of the region is limited.

We modified this region growing approach into a region-oriented segmentation. The main difference is that it is based upon the merging of the 3x3 pixel regions in a "region-based" mode. So only one region region is grown at a time. The subsequent region is not started until the previous region is completed. A region is grown by continuously appending to this region those neighboring 3x3 regions that have similar properties. The similarity criteria for merging are the same as Levine and Shaheen's suggestion.

At some stage in the process, let it be region k. For this region ,Rk ,there are q measures (spectral, textural measures), $T_k(q)$. For each measure q we defined the mean and standard deviations for this region k

$$\mu_k(q) = \frac{1}{n_k} \left(\Sigma\, T_k(q) \right)$$

$$\sigma_k(q) = \left\{ \frac{1}{n_k} \Sigma \left[T_k(q) - \mu_k(q) \right]^2 \right\}^{1/2}$$

where the region R_k contains N_k of the 3x3 pixel subregions, and $T_k(q)$ are these computed textures for that subregions.

For each 3x3 pixel subregion neighbored to the growing region k, if it is not labeled to any region yet, compute the update means and standard deviations for this region as if the 3x3 neighboring subregion was merged into this region k.

$$\mu'_k(q) = \frac{1}{n_k+1} \left[T_k(q) - n_k\mu_k(q) \right]$$

$$\sigma'_k(q) = \{\frac{1}{n_k+1} + \{ n_k\sigma_k^2 + (\frac{n_k}{n_k+1}) [T_k(q) - \mu_k(q)]^2 \} \}^{1/2}$$

Then, separate threshold values $\theta_k(q)$ are computed in order to determine weather or not to merge this 3x3 subregion to region k.

$$\theta_k(q) = [1 - \frac{\sigma'_k(q)}{\mu'_k(q)}] \theta_q$$

where θ_q is a constant threshold value selected for each textural measure, and $\theta_k(q)$ are the adaptive threshold values. In general, the larger the value chosen for θ_q, the fewer segmented regions result. Now, we compute the deviation $\Delta\mu_k(q)$

$$\Delta\mu_k(q) = | T_k(q) - \mu_k(q) |$$

if $\Delta\mu_k(q) \leq \theta_k(q)$ for each textural measures, then the 3x3 neighboring subregion is merged with the region k, and the values of $\mu_k(q)$ and $\sigma_k(q)$ are replaced with the updated values $\mu_k'(q)$ and $\sigma_k'(q)$, respectively. This testing-and-merge procedure is repeated until no more similar 3x3 subregion around this region.

After the segmentation of a scene is completed, a second merging is performed to combine small regions of similar characteristic into larger regions (classes).

3.1.3 Feature Identification

After all significant regions in a scene have been segmented and labeled, feature identification procedure are then applied to the segmented image. Each region is then examined and identified into a possible feature such as cloud, ice, lead, ice floes, meltpond.....etc base on their different physical properties, textural characteristics, shape...and so on.

More studies are needed for this section.

3.1.4 Computation of Sea Ice Parameters

Since all features in the scene have been properly segmented and identified, now we can easily pull out the feature of interest and compute the statistics needed. For example:

For meltpond fractional area:

$$\text{Meltpond Fractional area} = \frac{\text{number of pixels which are classified as meltpond}}{\text{total number of pixels in the scene}}$$

Sea ice fractional area, lead fractional area and new ice fractional area can be calculated in the same way.

For sea ice temperature and sea surface temperature:

Temperature can be determined directly from the thermal channel once the object (sea ice or sea surface) has been pulled out from the scene.

For ice floe size distribution:

The ice floe size distribution can be constructed by counting how many ice floes in the scene have the size between R to R+dR (size can be measured as pixel number or effective radius) and keep doing this by gradually increase R.

Lead size distribution can be obtain using the same method for ice floes except use the pixel number for measuring the size for a lead.

More investigation need to be done in this area in the future.

3.1.5 Uncertainties

(1) Different morphological operations, opening or closing, can result in different results for segmentation. The opening operator is effective in identifying ice floes and the closing operator is helpful for segmentation of cloud, cloud shadow and ice surface (including broken sea ice). Besides, what should the size of structuring element be? This problem is scene dependant also!

(2) Different constant threshold values, θ_q, for each textural measures can cause different segmentation results for the region growing process. These values vary from scene to scene Therefore, no automated segmentation procedure is possible for obtaining optimal segmentation results by region growing algorithm at present.

3.2 Practical Considerations

3.2.1 Programming/Procedural Considerations

The basic considerations for choosing certain approaches are the CPU usage and performance. Number of segmentation methods have been tested: probability relaxation technique, Mahalanobis classifier, Divide-and -Conquer technique as well as region growing segmentation. The region growing technique works the best (both in CPU and accuracy considerations) among those techniques for the LANDSAT TM testing data.

More test data will be used to test the algorithm, and there may be some other good techniques which perform the same task will be developed and added into this package later.

3.2.2 Validation

Since all the sea ice parameters can be easily retrieved once the scene has been properly segmented into meaningful regions, the key issue here becomes how to validate the segmentation algorithm? Haralick and Shapiro (1985) suggest that a segmentation should possess the following properties: 1) regions of a segmented image should be uniform and homogeneous with respect to the features; 2) adjacent regions should have significantly different features; 3) regions should be simple and without many small holes; and 4) boundaries of each region should be simple, not ragged, and be spatially accurate.

However, these are subjective measures and can not be automatized. So, besides these subjective measures we also develope a totally objective validation algorithm, we use scenes that have land and water in it and perform segmentation on them. The results are then overlapped with its geographical data (coastlines), therefore we know for sure where the land is and where the water is. Then we can compute the accuracy of the segmentation for land and water regions, so provide a automatic validation method for segmentation.

4.0 Constraints, Limitations, Assumptions

- Only daytime scenes may be used to provide information from visible channels.
- Input data has to be atmospherically corrected data in order to compute temperature parameters such as sea ice temperature.
- In region growing procedures, no optimal θq values can be determined. Therefore, no automated segmentation procedure is possible for obtaining optimal results at present by using region growing technique.
- To perform objective validation, it is necessary to use scenes that have land and water regions in it.

5.0 References

Bouman, C., and Liu, B., 1991, Multiple resolution segmentation of textural images. IEEE Trans. Patt. Anal. Mach. Intell., PAMI-13, 99-113.

Giardina, C. R., and Dougherty, E. R., 1988, Morpholo gical Methods in Image and Signal Processing, (Englewood Cliffs, N. J.: Prentic e Hall). 321 pp.

Haralick, R. M., and Shapiro, L. G., 1985, Image segmentation techniques. Comp. Vision Graphics Image Process, 29, 100-132.

Haralick, R. M., Shammugam, K. S., and Dinstein, I., 1973, Textural features for image classification. IEEE Trans. on Systems, Man, and Cybernetics, vol. SMC-3, N0. 6, 610-621.

Hsiao, J. Y., and Sawchuk, A. A., 1989, Unsupervised textural image segmentation using feature smoothing and probabilistic relaxation techniques. Comp. Vision, Graph. Image Proc., 48, 1-21.

Keller, J. M., Chen, S., and Crownover, R. M., 1989, Texture description and segmentation through fractural geometry. Comp. Vision, Graphics and Image Proc., 45, 150-166.

Levine, M. D., and Shaheen, S. I., 1978, A Modular Computer Vision System for Picture Segmentation and Interpretation. IEEE Trans. Patt. Anal. Mach . Intell., PAMI-3, 540-556.

Laprade, R. H., 1988, Split-and -merge segmentation of aerial photographs. Comp. Vis Graph Image Proc, 44, 77-86.

Meurle, J. L., and Allen, D. C., 1968, Experimental evaluation of thehniques for automatic segmentation of objects in a complex scene. G. C. Chang, R. S. Ladley, D. K. Pollock, and A. Rosenfeld, eds., Pictorial Pattern Recognition, (Washington, DC: Thompson), pp.3-13.

Moran, C. J., 1990, A morphological transformation for sharpening edges of features before segmentation. Comp. Graphics Image Proc., 49, 85-94.

Ohlander, R., Price, K., and Reddy, R., 1978, Picture segmentation by a recursive region spitting method. Comp. Graphics Image Proc., 8, 313-333.

Schalkoff, R. J., 1989, Digital Image Processing and Computer Visio, (New York: John Wiley and sons). 489 pp.

Schlesinger, M. E., and Mitchell, J. F. B., 1987, Climate model simulations of the equilibrium climatic response to increase carbon dioxide. Rev. Geophys., 25, 760-798.

Serra, J., 1982, Image Analysis and Mathematical Morpholog, (london: Academic Press). 610pp.

Steffen, K., and Lewis, J. E., 1988, Surface temperatures and sea ice typing for northern Baffin Bay. Intnl >J. Rem. Sens., 9, 409-422.

Taylor, R. W., Savini, M., and Reeves, A. P., 1989, FAst segmentation of range imagery into planar regions. Comp. Graphics Image Proc., 45, 42-60

Weszka, J. S. Dyer, C. R., and Rosenfeld, A., 1976, A Comparative Study of Texture Measures for Terrain Classification. IEEE Trans. Syst., Man, and Cybern., SMC-6, No. 4, 2269-1185.

Wetheerald, R. T., and Manabe, S., 1986, An investigation of cloud cover change in response to termal forcing. Clim. Change, 8, 5-23..

Algorithm Theoretical Document

for the ASTER products:

Product Number	Product
1391	Cloud base height
1427	Cloud top height
3625	Cloud thickness

Version 1.0

December 1992

Team member: Dr. Ronald Welch[1]

[1]IAS, South Dakota School of Mines & Technology

Table of Contents

1.0 Introduction

This document describes the theoretical basis for the cloud base height, cloud top height, and cloud thickness algorithms. The EOS product numbers and levels are:

EOS Product #	Level	Product
1391	2C1	Cloud Base Height
1427	2C1	Cloud Top Height
3625	2C1	Cloud Thickness

All of the algorithms and methods currently being considered for inclusion in the cloud base height and cloud top height algorithms are described. The algorithms described in this document are level zero and are under development. Some parts of the algorithms may be modified or deleted, and new ones may be added to the final product.

The cloud base height algorithm (CBH) is based upon the geometric relationship between a cloud and its shadow. Various image processing methods are used to preprocess the image. Then a pattern matching algorithm is applied to match cloud and shadow edges. The separation distance is determined and used along with the solar elevation angle and pixel resolution to compute the cloud base height. The cloud edges chosen for pattern matching are those which are are nearly parallel to the solar azimuth angle. By choosing only those edges, the effect of the cloud's vertical extent is minimized.

The cloud top height algorithm (CTH) uses the 3-D thermal map of cloud and cloud geometry to determine the average lapse rate of the cloud. This average lapse rate can then be used along with the CBH to determine the height of the coldest (highest) pixel in the cloud.

Cloud thickness is determined by computing the difference between the cloud base and top heights.

2.0 Background and Overview

Cloud base height is an important variable governing surface energy budgets. Cloud top height affects the amount of radiation emitted from the top of the atmosphere. Uncertainties in the cloud base height or cloud top height can lead to errors in energy balance computations.

The purpose of this algorithm is to provide an automated method for estimation of cloud base and cloud top height from high resolution satellite data. Visible data is used for the cloud base height algorithm because it provides distinct clouds and cloud shadows for pattern matching. The cloud top height algorithm also uses a thermal channel to map the cloud temperature. The specific ASTER channels to be used will have to be determined when test data is available.

The results of this algorithm will provide a cloud climatology data set which may be used by other scientists to more accurately model the surface energy budget.

A variation of this algorithm has been used to estimate cloud base height from LANDSAT MSS, LANDSAT TM, and AVIRIS data. Several papers based upon this

algorithm have been published. Much of the basis for this algorithm is described in the Berendes et. al. paper listed in the references.

LANDSAT TM images have been used as test data for the development of this algorithm.

3.0 Algorithm Description

The following sections describe the cloud base height (CBH) and cloud top height (CTH) algorithms. The algorithms discussed here are of a preliminary nature. Although the details may change somewhat, the basic algorithm should remain essentially the same throughout development. This section will describe the following topics:

3.1 Cloud Height Geometry
3.2 Cloud Base Height Theory
3.3 Cloud Top Height Theory
3.4 Cloud Base Height Algorithm Implementation
3.5 Cloud Top Height Algorithm Implementation
3.6 Cloud Thickness
3.7 Uncertainties
3.8 Practical Considerations
3.9 Validation
3.10 Quality Control and Diagnostics and Exception Handling

3.1 Cloud Height Geometry

The basis behind the height algorithm is the trigonometric relationship between a cloud and its shadow. Figure 1 shows the relationship between a point (1) on the cloud and its corresponding point (2) on the shadow.

Since α is a known quantity, only the separation distance d is needed to compute the height h.

In practice, it is difficult to match an arbitrary point on the cloud edge to its corresponding point on the shadow edge. Instead, we match sections of the cloud and shadow edges.

3.2 Cloud Base Height Theory

Since clouds have a vertical extent, cloud edges used for CBH estimation are chosen to minimize any effects of vertical development. We assume that the cloud thicknesses taper toward their edges and that the bottom of the cloud is relatively flat. This is approximated by a hemispherical model. Figure 2 shows a side view of a hemispherical cloud and its shadow. The view is perpendicular to the solar azimutal angle. θ_o is the solar zenith angle. Point A and D mark the extent of the shadow cast by the cloud on a flat surface. Note that point A represents a shadow cast by point a which is not at the cloud

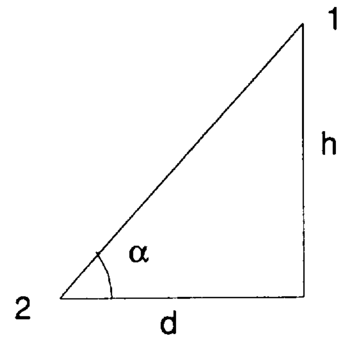

where d is the horizontal distance
α is the solar elevation angle
h is the height

$$h = d \tan \alpha$$

Figure 1. Cloud height geometry.

base, but somewhere between the base and the top. This causes the shadow to be elongated by a distance AB. The elongation of the shadow would give erroneous cloud base height calculations. Therefore, the leading edge of the cloud toward the shadow must be avoided when choosing cloud edges for pattern matching.

The trailing edge would be ideal for pattern matching since there could be no elongation effect. However, this edge is not always visible from the satellite. In Fig. 2, a nadir viewing satellite will not see point D, which corresponds to the trailing edge of the cloud, because it is obscured by the cloud.

Therefore, we choose the two side edges of the cloud for pattern matching. Since the cloud thickness tapers toward the base, the effects of vertical development at these edges is minimal. Fig. 3 shows the selection of cloud edges. β represents the solar azimuthal angle. The dotted line passes through the centroid of the cloud in the direction of

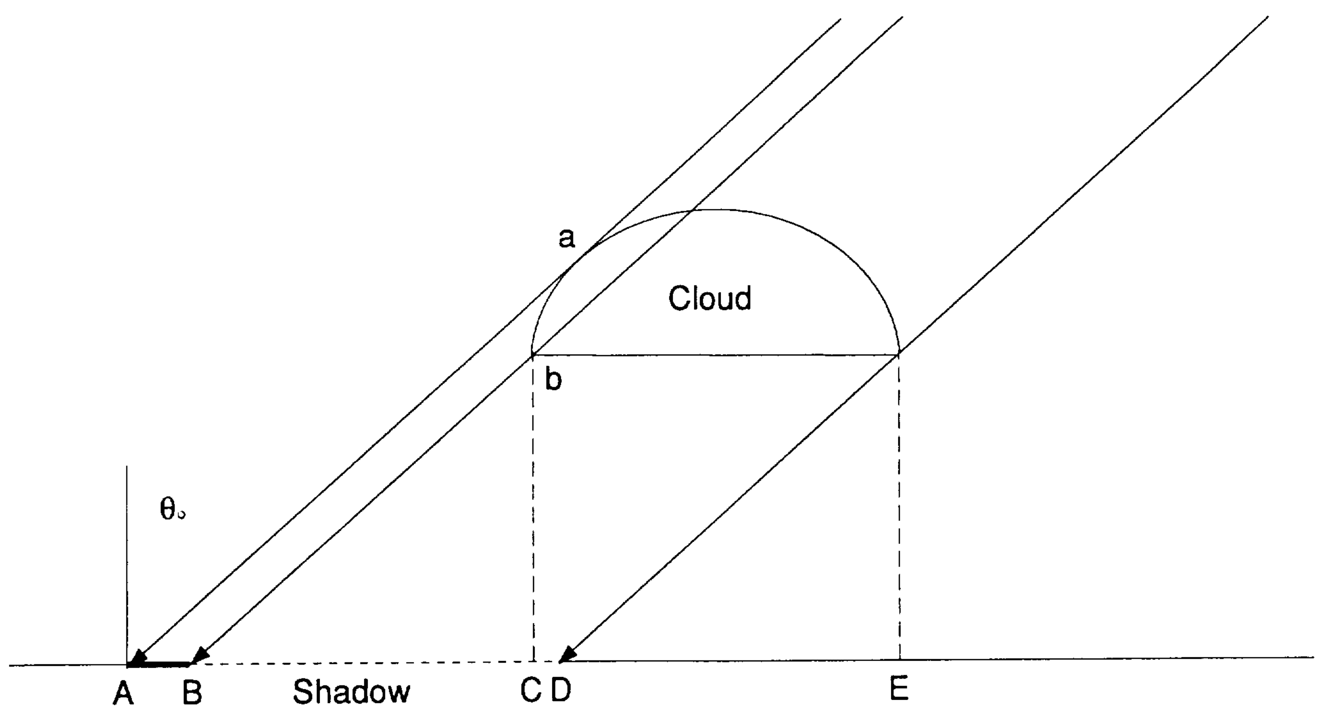

Figure 2. Side view of cloud and shadow

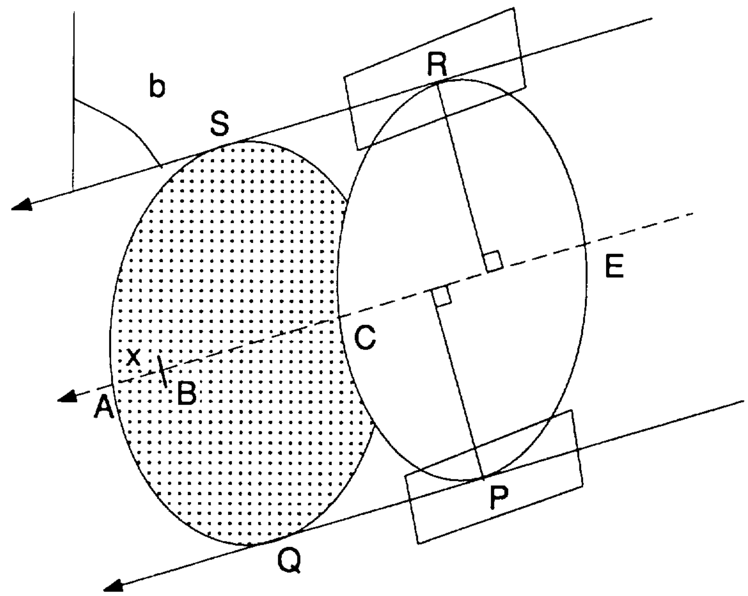

Figure 3. Top view of cloud and shadow. The boxed areas around R and P indicate cloud edges used for CBH.

the azimuth. Points P and R are the edge points farthest from the dotted center line. The boxed areas surrounding P and R represent the edges chosen for CBH pattern matching.

3.3 Cloud Top Height Theory

The CTH algorithm is based upon the 3-D thermal mapping of the cloud top. Cloud temperature decreases with height in the atmosphere. By using the average lapse rate within the cloud and the cloud base height, we can estimate the height of any point within the cloud. The height of the coldest point will give us the cloud top height.

Fig 4 shows a 3-D mapping of a cloud based upon its temperature profile assuming a moist adiabatic lapse rate of 6.5°C/Km. Although the lapse rate may be incorrect, the mapping provides us with the shape of the cloud top.

Now, we look at the leading edge of the shadow. This is the edge near point A in Fig 3. The edge of the shadow in this region is cast by sections of the cloud above the base. For example, in Fig 2, we project a line from point A along both the solar azimuth and zenith angles. This line intersects the cloud at point a, the cloud point which cast the shadow.

Finding the cloud point which creates a specific point on the shadow is accomplished by using the 3-D mapping. By varying the lapse rate in the mapping, we adjust the height of the cloud top. We project the shadow point along the solar azimuth and zenith line throughout the cloud. When the line intersects a single point on the cloud, we have found the point casting the shadow. The lapse rate which produces a single intersection is determined by this process.

The procedure is applied to several shadow points and the average lapse rate for

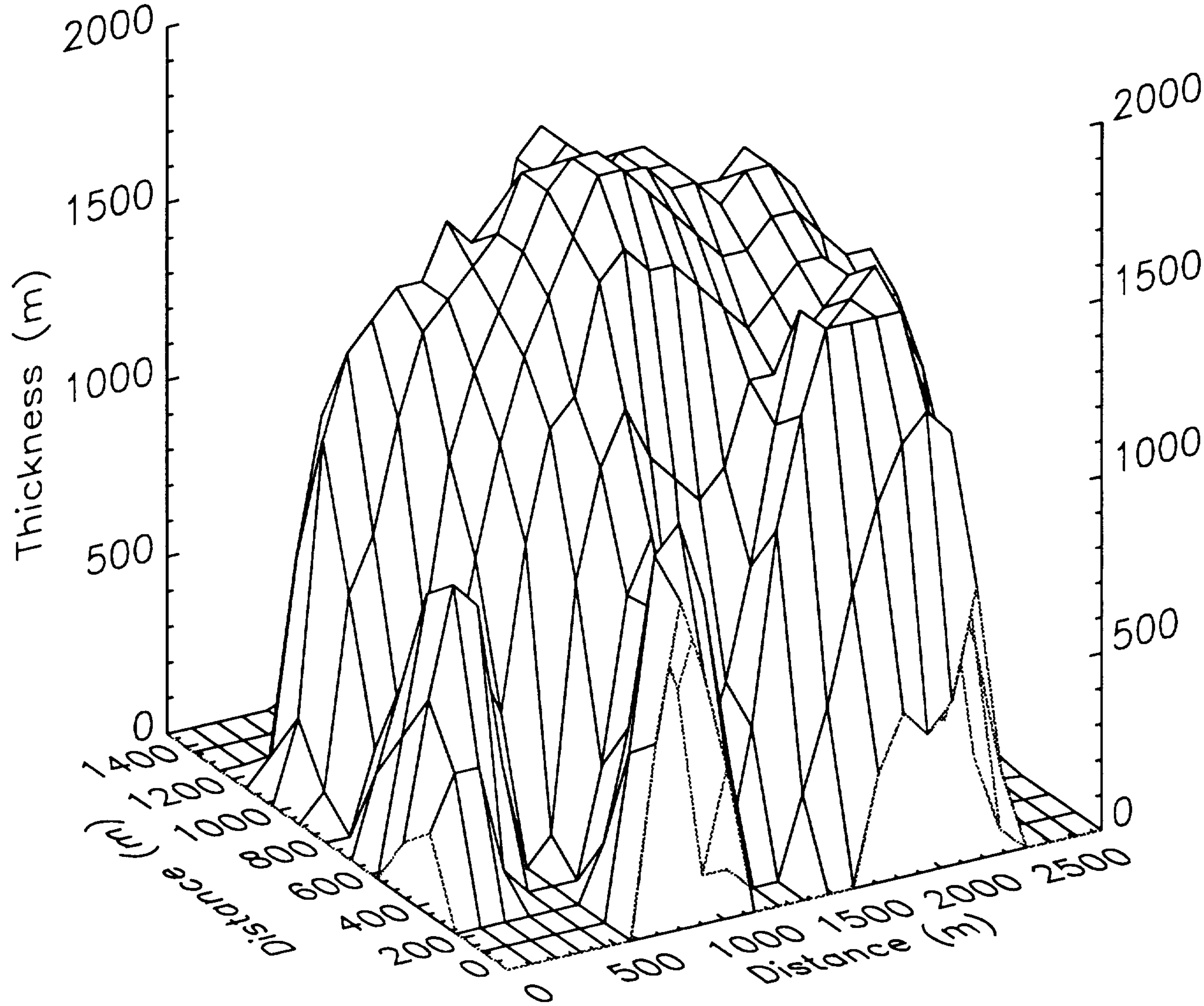

Figure 4. 3-D wireframe mapping of a cloud based upon its temperature profile assuming a cloud lapse rate of 6.5°C/Km.

the cloud is determined. Since the CBH is already calculated using the previously described algorithm, the CTH is determined by applying the average lapse rate to the coldest point on the cloud. Indeed, the height of any point on the cloud can now be determined.

3.4 CBH Algorithm Implementation

The CBH algorithm consists of the following steps:

1. Preprocess the image
2. Find cloud sizes and locations and select cloud edges for pattern matching

3. Pattern match cloud edges with shadow edges
4. Find CBH

3.4.1 Preprocessing

The goal of preprocessing is to reduce the image to only clouds, shadows, and background. Since cloud and shadow edges will be matched, we further reduce the image to edge components only.

The preprocessing algorithm is composed of the following steps:

1. Histogram specification
2. Noise reduction
3. Image segmentation, edge detection and classification

3.4.1.1 Histogram Specification

The histogram of a satellite image can be thought of as a composite of the individual distributions of classes within the image. The underlying distributions are usually gaussian in nature. However, there is often a large overlap of classes which blends the distributions together.

Our goal is to segment the clouds, shadows, and background. In order to properly segment the image, proper thresholds must be chosen. Choosing proper thresholds is a very difficult and often subjective problem. Figure 5 shows a histogram which is very easy

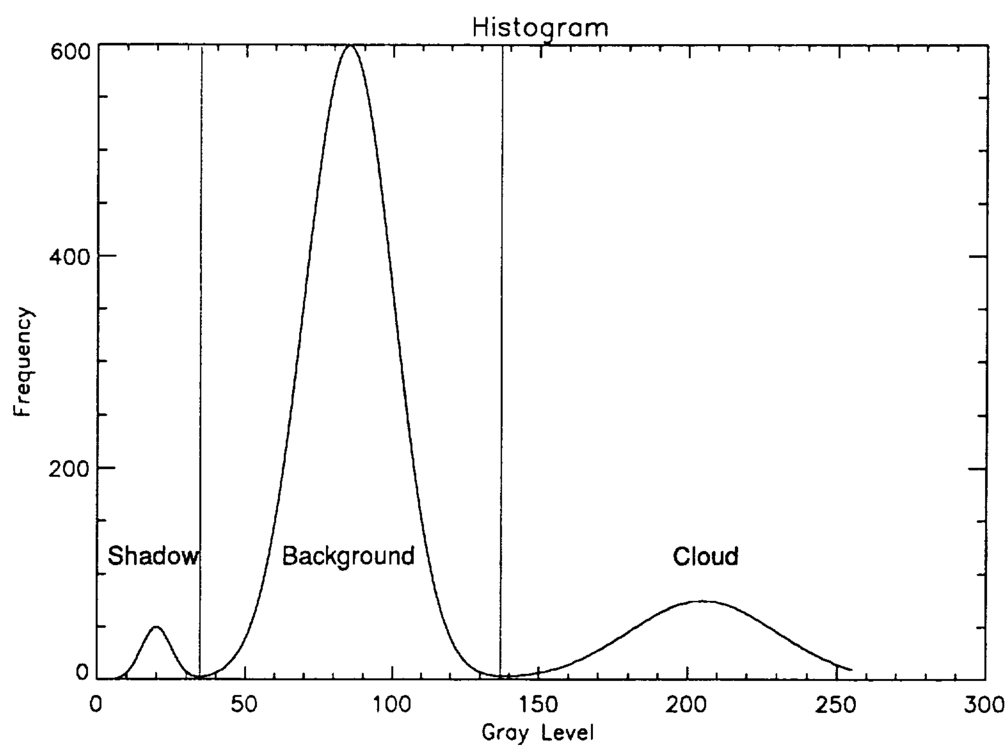

Figure 5. Ideal 3 mode histogram

to threshold. The three distributions are easily separable. The cloud and shadow thresholds of this histogram are at the minimum points between distributions.

The Histogram specification method is used to force the histogram of the image to an easily separable histogram like that in Fig. 5.

First, the peak value A is determined. Next, $f(\sigma)$ is calculated based upon the equation given in Fig. 6. We determine σ by finding the grey level of the histogram value on either side of μ which most closely matches $f(\sigma)$. We now know the height and approximate width of the background distribution. This provides μ_b and σ_b, the mean and standard deviation of the background distribution for the specified histogram. The cloud and shadow distributions are constructed by fixing choosing the following values for μ and σ:

Cloud:	$\mu_c = 215$;	$\sigma_c = 25$
Shadow:	$\mu_s = 20$;	$\sigma_s = 5$

The peak value for the shadow distribution is chosen by finding the average frequency of all grey level values below $\mu_b - \sigma_b$ in the original histogram and multiplying by 2. Similarly, for the cloud we average the frequency of all grey level values above $\mu_b + \sigma_b$ and multiply by 3/2. These values seem to provide distributions which are clearly separated and realistically weighted.

Fig 7A shows the histogram of a Landsat TM scene containing ocean, clouds, and shadows. The ocean distribution dominates the histogram and merges with the shadow and part of the cloud distribution. Fig 7B shows the specified histogram constructed based upon the procedure described above.

$$f(x) = A \exp \frac{-(x - \mu)^2}{2\sigma^2}$$

Where: A is the peak value
x is the grey level
μ is the mean
σ is the standard deviation

Therefore: $f(\mu)=A$ and $f(\sigma)= A \exp(-1/2)$

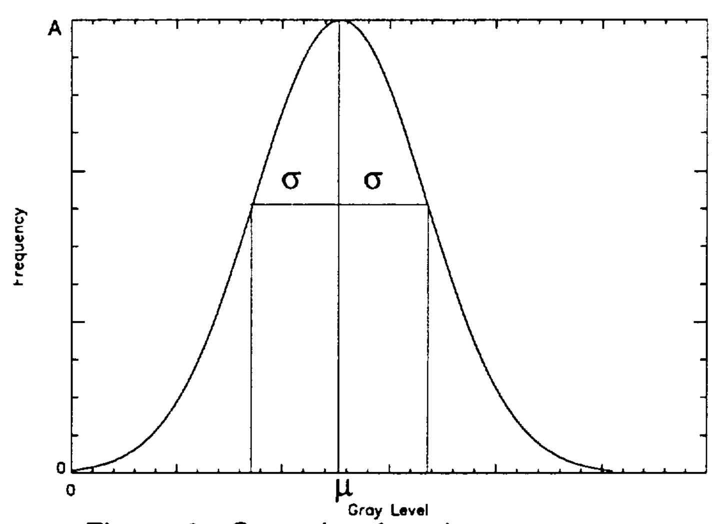

Figure 6. Gaussian function

Now, the histogram specification method is employed (Gonzales & Wintz, 1987). Histogram specification applies the histogram equalization method to obtain and equalized histogram mapping. Both the original and specified histogram are equalized. Then, the reverse mapping of the specified histogram is applied to the equalized original histogram. This has the affect of fitting the original histogram to the shape of the specified histogram.

A

B

C

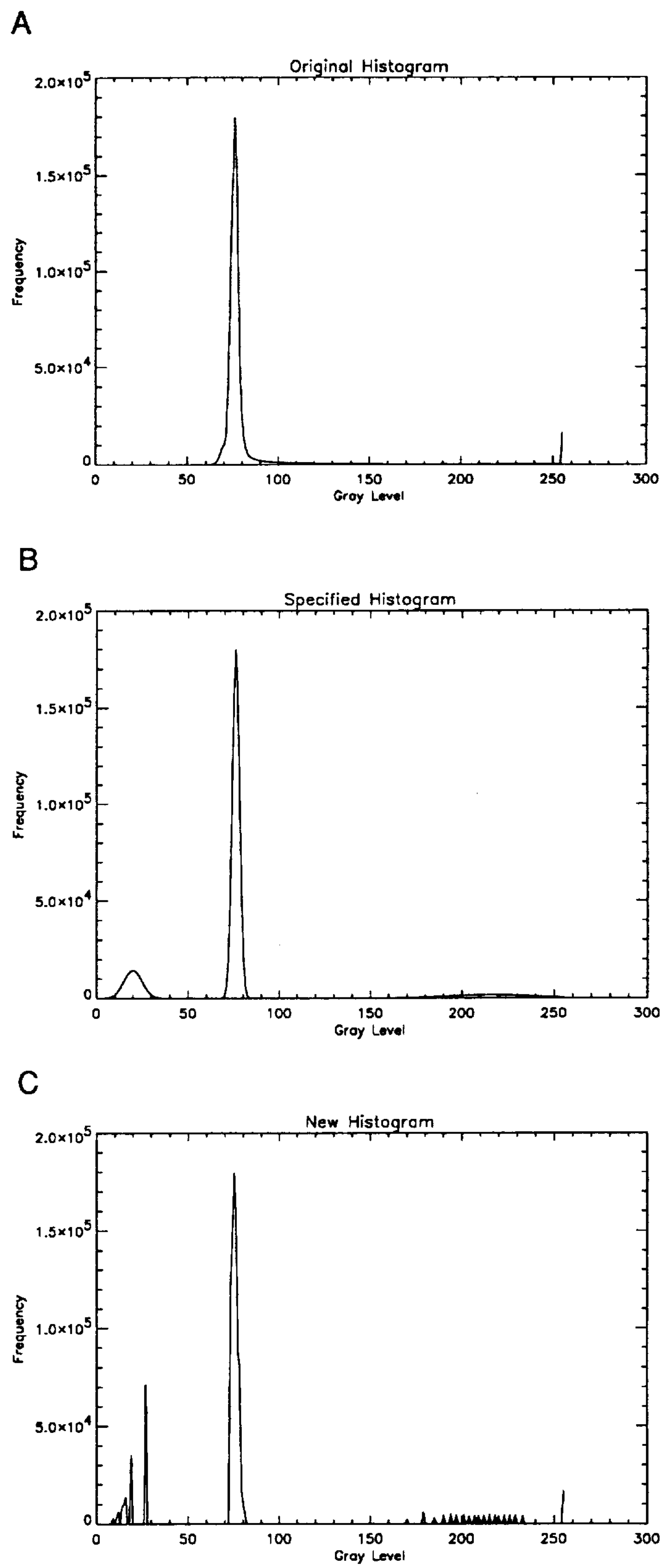

Figure 7. Histograms of a LANDSAT TM scene. A shows the original histogam, B shows the specified histogram and C shows the new histogram resulting from histogram specification.

Figure 7C shows the original histogram after it has been fitted to the specified histogram. Three distinct distributions are now visible, and thresholds between them are easily chosen.

3.4.1.2 Noise Reduction

The standard technique of median filtering (Richards, 1986)with a 3 x 3 kernel is applied to the preprocessed image to eliminate noise. Median filtering finds the median of the 3 x 3 kernel area and replaces the center pixel with the median.

Median filtering is a good choice for noise removal because it eliminates speckle noise without distorting edge transitions. It also preserves the grey level range of the original image.

Median filtering is applied at various stages in the algorithm whenever noise removal is a benefit.

3.4.1.3 Image Segmentation, Edge Detection and Classification

Image segmentation is performed by using the thresholds found in section 3.4.1.1. The image is reduced to three gray levels, one for each of cloud, shadow, and background.

After the image is segmented, the clouds are found and their optical center is computed. A table is constructed which contains the center location and size of each cloud in the image. This table is used in later phases of the algorithm.

After the image is segmented, a Roberts operator is applied to the image (Gonzales & Wintz, 1987). This creates a new image with only the edge transitions remaining as single pixel wide lines.

By checking the type of transition occurring at an edge pixel, the edge is classified as either cloud or shadow. Three transitions are possible:

cloud → shadow
cloud → background
shadow → background

The transitions are determined at each edge pixel, and the pixel is classified. This produces an image containing only cloud and shadow edges with all cloud edges of the same gray level and all shadow edges of the same gray level. This is the image used for pattern matching.

3.4.2 Edge Selection

Edge selection for pattern matching is based upon the algorithm described in Section 3.2. The dotted line in Fig 3 passes through the optical center of the cloud in the direction of the solar azimuth angle. Points R and P are at a maximum distance

perpendicular to the center line. An area is enclosed around points R and P which will be used in the next section for pattern matching.

3.4.3 Pattern Matching

The Generalized Hough Transform (Ballard, 1981) is used to match the cloud and shadow edges. The Generalized Hough Transform (GHT) is a technique which allows parameterization and matching of arbitrary shapes.

The cloud edge is parameterized with respect to an arbitrary reference point, in this case, the optical center of the cloud. A search area is then computed along the solar azimuth. The GHT pattern matching algorithm is applied to find the most likely position of the reference point within the search area. After pattern matching, we know the locations of the cloud reference point and its match in the shadow. For a detailed discussion into the workings of the GHT algorithm refer to Berendes et. al. 1992.

3.4.4 Cloud Base Height Estimation

From the previous step, the positions of the cloud and shadow reference points are known. First, the separation distance is determined. This corresponds to d in Fig 1. The equation shown in figure 1 is applied to calculate the cloud base height.

The calculated height must be adjusted for terrain by using a digital elevation model. Also, if the viewing angle of the satellite is off nadir, an adjustment may be necessary.

3.5 CTH Algorithm Implementation

The CTH algorithm consists of the following steps:

1. Run the CBH algorithm
2. Run the CTH algorithm
3. Calculate CTH

As with the CBH, The CTH may have to be adjusted for terrain and viewing angle.

3.6 Cloud Thickness

The cloud thickness is simply the difference between the cloud base height and the cloud top height. Also, by using the average lapse rate from the CTH algorithm, the thickness at any point in the cloud can be determined.

3.7 Uncertainties

The CBH algorithm is not significantly affected by uncertainties in the input image.

The algorithm has been designed to find the optimal threshold for the preprocessing phase. Errors in individual pixels should not be a problem since the pattern matching is performed on a section of the cloud edge, not a single point.

Errors in the digital elevation model could significantly affect both height calculations. Variations in elevation below the resolution of the DEM could also affect both height calculations.

The CTH algorithm is sensitive to the accuracy of the thermal channel data. Errors could cause incorrect lapse rate and height calculations.

The degree to which height calculations are affected by these errors has not yet been studied.

3.8 Practical Considerations

There are several practical considerations regarding the algorithm. Every effort has been made to minimize computational expense of the algorithm. The most expensive part of the CBH algorithm is the pattern matching. The Hough transform method has been used successfully in the past, but there may be other less expensive options. In the past, scaling was used with the Hough transform. This proved to be fairly expensive and provide little improvement in the accuracy of the matching. Therefore, in the current version, scaling is not implemented.

The preprocessing phase of the algorithm may need to be adjusted for different scene types. Land images may require different preprocessing than ocean scenes. More test data is needed to adjust the algorithm.

Presently, Landsat TM and MSS data has been used for development of the algorithm. Better test data is needed to more closely approximate the type of data the algorithm will encounter in actual use.

3.9 Validation

Independent validation of the algorithm is needed during the design phase. Ceilometer, lidar, aircraft, radiosonde, or pibal observations can be used to validate our calculated retrievals. These observations must be coordinated with an overpass of the satellite. Plans are underway to obtain this type of data for validation.

Cloud top height may be validated by aircraft or radiosonde.

3.10 Quality Control and Diagnostics and Exception Handling

Internal performance monitoring and analysis may be performed at various phases of the algorithm.

During the preprocessing phase, a check is applied to the histogram specification algorithm to determine if a proper specification has occurred. This check will examine the basic distributions in the histogram. If the cloud, shadow, or background distributions are too large, small, or unidentifiable, then the algorithm will reject the image or flag it for further analysis.

After histogram specification, thresholding, and cloud location, the cloud field will be examined. Clouds which are too large or small will be eliminated from consideration. Usable cloud sizes are yet to be determined.

The Generalized Hough Transform pattern matching algorithm allows us to check its performance. The ratio of matching edge points can be determined and used as a measure of the fit. Correlation can be used as an independent validation of the pattern match.

Since two edges of the cloud are being matched with their shadows, the heights obtained at each edge can be compared to check for consistency. If the heights are inconsistent, the previously mentioned tests may be applied to find the incorrect height.

Statistical outlier tests can be applied to the results of the CBH and CTH algorithms. Outliers may be eliminated or flagged for further investigation.

4.0 Constraints, Limitations, Assumptions

As with any algorithm, certain conditions must be met for normal operation of these algorithms.

Since visible data is needed, only daytime scenes may be used. A corresponding thermal channel must be present for the CTH algorithm. The lapse rate within clouds is initially assumed to be constant. Images containing snow or ice may cause difficulties with the thresholding procedure. Further study using more test data is needed to assess the algorithm's performance over difficult backgrounds.

Obviously, clouds and shadows must be present in the visible image. Cumulus clouds or the edges of stratocumulus decks provide the best candidate clouds.

Assumptions about cloud geometry are made. Clouds are assumed to taper toward the base at the edges. The heights calculated at the edges described in sect. 3 are assumed to be at the cloud base. Thin cloud edges can cast a shadow on the ground yet not differ significantly from the background albedo. This effect can be seen in smaller clouds. Their shadows sometimes appear wider than the actual cloud. Therefore, the cloud edge seen by the satellite may actually be at a slightly higher(thicker) level in the cloud. This effect may bias the height measurements toward slightly higher base and top heights. More study is needed in this area.

References

Ballard, D. H., 1981: Generalizing the Hough Transform to detect arbitrary shapes. *Pattern Recognition*, **13**, pp. 111-122.

Berendes, T., S. K. Sengupta, R. M. Welch, B. A. Wielicki, M. Navar, 1992: Cumulus cloud base height estimation from high resolution LANDSAT data: a Hough Transform approach. *IEEE Trans. on Geosci. and Remote Sensing*, **30**, p. 430-443.

Gonzales, R. C, and Paul Wintz, 1987, *Digital Image Processing. Second Ed.*, Addison-Wesley, Reading, MA, 503 pp.

Richards, J. A., 1986: *Remotes Sensing Digital Image Analysis.* Springer-Verlag, New York, NY, 281 pp.

Algorithm Theoretical Document

for the ASTER product:

Product Number	Product
1409	Cloud 3-D Structure

Version 1.0

December 1992

Team member: Dr. Ronald Welch†

†Institute of Atmospheric Sciences, South Dakota School of Mines and Technology, Rapid City, South Dakota, U.S.A.

Table of Contents

1.0 Introduction

This document describes the theoretical basis for cloud three-dimensional (3-D) structure algorithm. The EOS product number, product level, and version number are:

EOS Product #	Level	Version	Product
1409	2C1	1.0	Cloud 3-D Structure

This is a special product which is produced upon request. The infrared window channel images (ASTER band 13 [10.6 μm] and 14 [11.3 μm]) are used to produce this product. First the image has to contain clouds. The following steps then are taken to extract the 3-D structure from clouds: (1) thresholding of the image to distinguish clouds from background, (2) segmenting individual clouds in the thresholded image, (3) recognizing individual cells in a cloud, and (4) approximating the cell's overall shape with a quadric surface. (Hereinafter the method used in each step will be called a 'method' to distinguish form the main 'algorithm' which encompasses all four 'methods'.) Other statistics then can be generated using the output, for example, the number of cells in a cloud as a function of the effective cloud diameter, the mean distance between the nearest cells in a cloud, the variation of the real cloud height from the approximation, and so on.

This document describes each aforementioned method in detail. In the current version, the knowledge of the environment lapse rate is assumed and no emissivity correction is implemented. Therefore, no use of other ASTER product is necessary to generate the present product. In the future, the information of cloud emissivity and environment lapse rate derived from other ASTER product can and will be incorporated.

All the methods currently being used for determining the cloud 3-D structure are described. The methods described in this document are still evolving and being improved upon. Better methods will replace the current ones when they become available.

2.0 Overview and Background Information

One of the most important environmental challenges facing mankind is the problem of climate change. A thorough description and understanding of processes at the earth's surface and in the atmosphere is necessary before realistic climate prediction can be realized. In particular, climate change and climate stability are strongly related to the earth's radiative energy balance

which is modulated by cloud cover (Ramanathan, 1987, 1988). On the other hand, cloud properties are a function of regional weather and climatic variables (Roeckner et al., 1987; Ramanathan and Collins, 1991).

Accurate predictions of climate change require a detailed understanding of the radiative impact of broken cloudiness. The goal is the development of radiative transfer parameterizations accurate to within $10 Wm^{-2}$ in the solar spectrum. However, in order to accurately estimate and model radiative fluxes at the top of the atmosphere, first it is necessary to determine cloud cover, cloud type, and cloud field morphology. Unfortunately, while there is a wealth of information concerning cloud microphysics, there is little information in the literature concerning cloud macrophysical properties. Indeed, cloud shape, mutual shadowing, cloud-cloud interactions, spatial inhomogeneities, and surface albedo have been shown to be important variables. Radiative fluxes for horizontally inhomogeneous clouds differ from those for plane parallel clouds because photons enter and exit the cloud sides.

One of the critical components of global cloud climatology studies is the retrieval of cloud optical thickness and effective particle size. However, all algorithms now in use are based upon plane-parallel radiative transfer calculations. For broken cloudiness, these retrievals particularly sensitive to 3-D cloud effects, both to photons entering and exiting cloud sides and to mutual cloud shadowing.

Studies by Nakajima et al. (1991) show that while optical thickness can be somewhat accurately retrieved, the remotely sensed effective particle radius usually exceeds in situ measurement by about 3 μm. Some researchers attribute this disagreement to anomalous absorption. Yet, 3-D effects may play a more important role. In addition to the complex phenomenon of photons leaking from cloud sides and to cloud-cloud interactions, the change of solar illumination and satellite viewing angles from sloping cloud sides may strongly influence satellite measured radiances.

2.1 Experimental Objective and Historical Perspective

This product is intended for (1) illumination and viewing geometry correction and for (2) more realistic modelling of clouds.

Since for all cloud property retrieval studies a plane-parallel radiative transfer model is employed and none has investigated the influence of the shape (e.g. the sloping

boundaries) of the clouds to the retrieval, this product will provide the necessary information for the illumination and viewing geometry correction. The influence of cloud shape can therefore be estimated.

This product will also aid the Monte Carlo radiative transfer study in creating more realistic clouds and cloud fields. In previous studies only simple geometric shapes (e.g. cubes, cylinders, hemispheres, and so on) are used to simulate cloud. In reality clouds have much more complicated shapes. This product will provide not only a quadric surface fit to the individual cells in clouds, but also a statistical measure on how the real cloud surface differ from the fit.

2.2 Instrument Characteristics

The bands in the infrared atmospheric window (band 13, 10.25-10.95 μm; and band 14, 10.95-11.65 μm) are to be used to generate this product. In these bands the radiometric resolution is $\leq$ 0.3K and the spatial resolution is 90 m. If the moist adiabatic lapse rate (6.5°C/km) is assumed, a temperature difference of 0.3 K corresponds to ~46 m in height.

3.0 Algorithm Description

The algorithm used to analyze the images consists of the following four steps: (1) thresholding of the image to distinguish cloud from background; (2) segmenting individual clouds; (3) finding cells in each cloud; and (4) modeling the shape of the cells in clouds. Each step is described in more detail below.

3.1 Thresholding

Digital counts of the thermal band images are first calibrated and converted to brightness temperatures. The histogram then is examined, and the background temperature is determined as the temperature of the warm maximum of the histogram. In accord with the International Satellite Cloud Climatology Project (ISCCP) algorithm (Rossow et al., 1985; Rossow et al., 1991), the threshold distinguishing cloud from background is chosen as 2.5°C below the background temperature over open ocean or 3.5°C over coastal ocean.

In general, an emissivity correction should be applied to obtain the real cloud temperature from the brightness temperature, especially in the optically thin parts of the clouds. However, the emissivity correction is not implemented in the current version of

this algorithm. According to Wielicki and Parker (1992) the ISCCP thermal threshold tends to underestimate cloud cover by eliminating the optically thinner parts of the clouds. By using this threshold, only relatively thick parts of the clouds are analyzed, where the effect of emissivity is relatively minor.

More elaborate thresholding method may be used in the future. For example, the cloud cover product may be utilized to determine the threshold temperature so that the cloud fraction of the image is the same.

3.2 Segmentation

In order to model cells in individual clouds, the image first needs to be segmented. The objective of segmentation is to distinguish between the background and clouds, and to label different clouds as unique entities. Clouds can be segmented according to 4-connectedness or 8-connectedness. For 4-connectedness, two cloudy pixels are said to be connected, hence belonging to the same cloud, if they are immediate neighbors either vertically or horizontally, but not diagonally, while for 8-connectedness diagonal neighbors are also considered connected.

For segmentation using 4-connectedness, a cloudy pixel is selected. Then its four neighbors are checked in the clockwise direction, from the neighbor above to the neighbor to the left. The first of its cloudy neighbors that has not been previously visited is the next stop. The remainder of the unvisited cloudy pixels are placed into a first-in-first-out (FIFO) waiting queue. The visited pixels are assigned with a unique number associated with the current cloud. This process continues until a pixel is reached in which no unvisited cloudy neighbor can be found. Then a cloudy pixel is fetched from the FIFO waiting queue and the process is resumed until every cloud pixel is flagged. The process is repeated until all the clouds in the scene are segmented.

This algorithm is illustrated in Figure 1 where the stippled area represents the background while the white squares represent cloudy pixels. The pixel indices, i and j, give the column and line numbers respectively. A pixel at column i and line j is referenced as (i, j).

As cloud pixels are examined from left to right (i=1 to i=12) and from top down (j=1 to j=12), the first one encountered is pixel (6,2) (labelled trace 1). Its four neighbors are subsequently checked. Pixel (6,3) is its only cloudy neighbor and is therefore the next

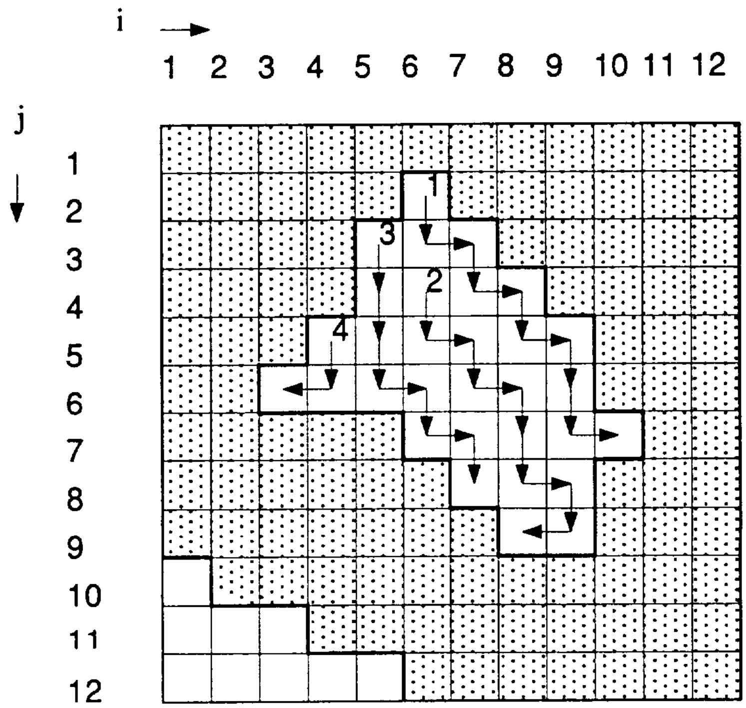

Figure 1: An illustration of the 4-connected cloud segmentation method.

stop, as indicated by the short arrow pointed from (6, 2) to (6, 3). Pixel (6,3), however, has four cloudy neighbors among which pixels (7,3), (6,4), and (5, 3) previously have not been visited. Applying the clockwise algorithm, pixel (7, 3) becomes the next stop and pixels (6, 4) and (5, 3) are placed in the FIFO waiting queue for later use. This process is repeated until pixel (10, 7) is reached; here no unvisited cloudy pixel is available, and trace 1 is terminated. Pixel (6, 4) is next in the FIFO waiting queue, and the process resumes from there (labelled trace 2). As it is shown, 4 traces are required to segment this cloud. The algorithm for 8-connectedness is similar, except that all 8 neighboring pixels are checked.

3.3 Cell Recognition

Progressive thresholding is used for cell recognition. Each individual cloud is processed according to the following procedure and criteria:

C-2

(1) Threshold is decreased in 0.3°C steps, progressively.

(2) As the temperature threshold decreases, the original cloud may split into objects which are cell candidates If a cell candidate has more than 4 pixels (an equivalent effective diameter of ~203 m), it is further traced in the same manner, i.e. decrease threshold and see if it splits. Otherwise it is ignored as a small-scale natural temperature variation.

(3) If a cell candidate with a size of 16 pixels or larger remains as an object until it diminishes under progressive thresholding, and the difference of the maximum and minimum temperatures in it exceeds 1.5 °C, it is considered a qualified cell for the shape analysis.

The cell size constraint is to guarantee enough samples for the least-squares fit used in shape analysis. As it is described in the next section, the equation used for the least-squares fit has 9 unknown coefficients. Sixteen pixels are required to give an accurate fit to the data. This yields an effective cell diameter of at least 406 m.

The minimum temperature difference criterion is applied to guarantee sufficient vertical development. Assuming a moist adiabatic lapse rate, a temperature difference of 1.5°C is equivalent to a difference of about 230 m in height. This corresponds to a height to diameter ratio of, $H/D_{eff} \approx 0.57$, assuming $D_{eff} = 406$ m. For morning Florida cumulus clouds, similar to those examined in this study (note that LANDSAT satellites have morning overpasses), Plank (1969) reports an average H/D_{eff} ratio of about 0.9. Therefore, with a value of $H/D_{eff} \approx 0.57$, virtually all of the important cloud vertical structure is captured in the cloud field.

Figure 2 schematically illustrate the procedure. The solid line gives the outline of the cross section of a cloud. The horizontal dashed lines represent temperature differences measured from the cloud-background threshold in 1°C intervals, while the vertical ones represent pixel boundaries. The capital letters A, B, C, D, and E denote individual cell candidates. The areal coverage of a cell in the figure is assumed to be the square of the length of its base.

As the temperature threshold is decreased, cell candidate E separates from the cloud when the temperature threshold reaches 3°C below the cloud-background threshold (i.e. cloud base). However, region E does not have enough vertical development (1.5°C) or areal coverage (16 pixels) to satisfy the cell criteria; therefore it is discarded. The next cell candidate that emerges is A, which has sufficient areal extent but not enough vertical

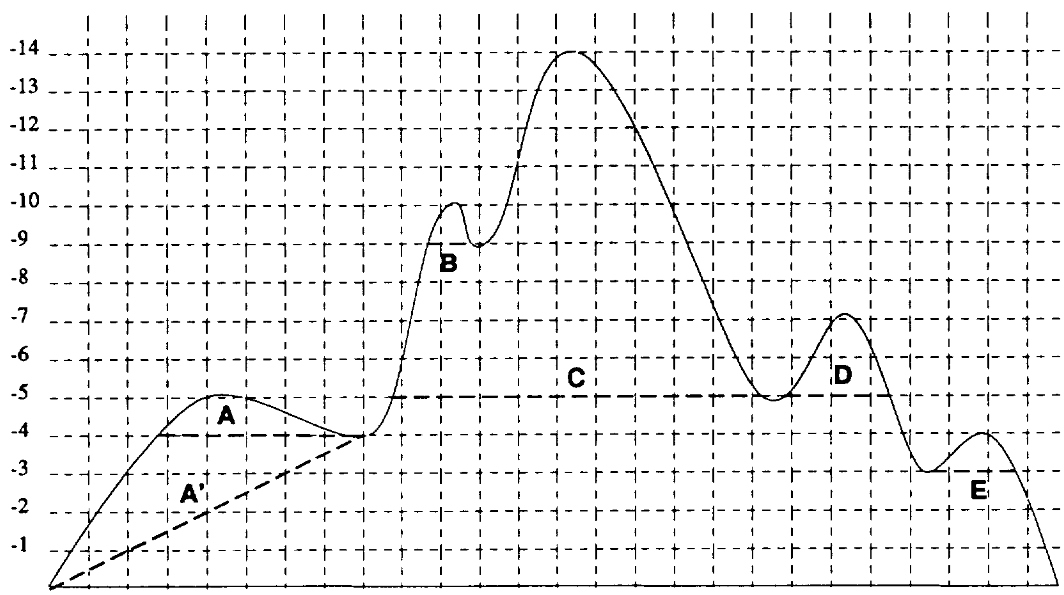

Figure 2: A one-dimensional schematic illustration of the cloud cell recognition process.

development. It is discarded also. As the temperature threshold continues to decrease, cell candidate D emerges. Candidate D has sufficient vertical development but not enough areal extent; therefore D is discarded. As the process continues, cell candidate B is found. Because of its small areal extent (< (2^2 = 4) pixels) it is considered as part of C. Cell C starts its base at a temperature 5 °C below the cloud-background threshold and has an areal extent of more than 9^2 pixels. At the end of this process, C is the only qualified cell found in this hypothetical cloud.

As it is shown above, the present cell recognition algorithm has some limitations. In particular the cells found must have homogeneous base temperatures, which is a rather strong constraint. For example, cell A's base is at 4 °C below the cloud-background threshold. A more realistic base for cell A perhaps is that denoted by the line A'. This cell base is relatively easy for our human eye to recognize, but it is very difficult for a computer algorithm to distinguish, especially in three dimensional analysis. Therefore, the present study represents a conservative definition of cloud cell structure.

Figure 3 shows three-dimensional representations of six unicellular cumulus clouds

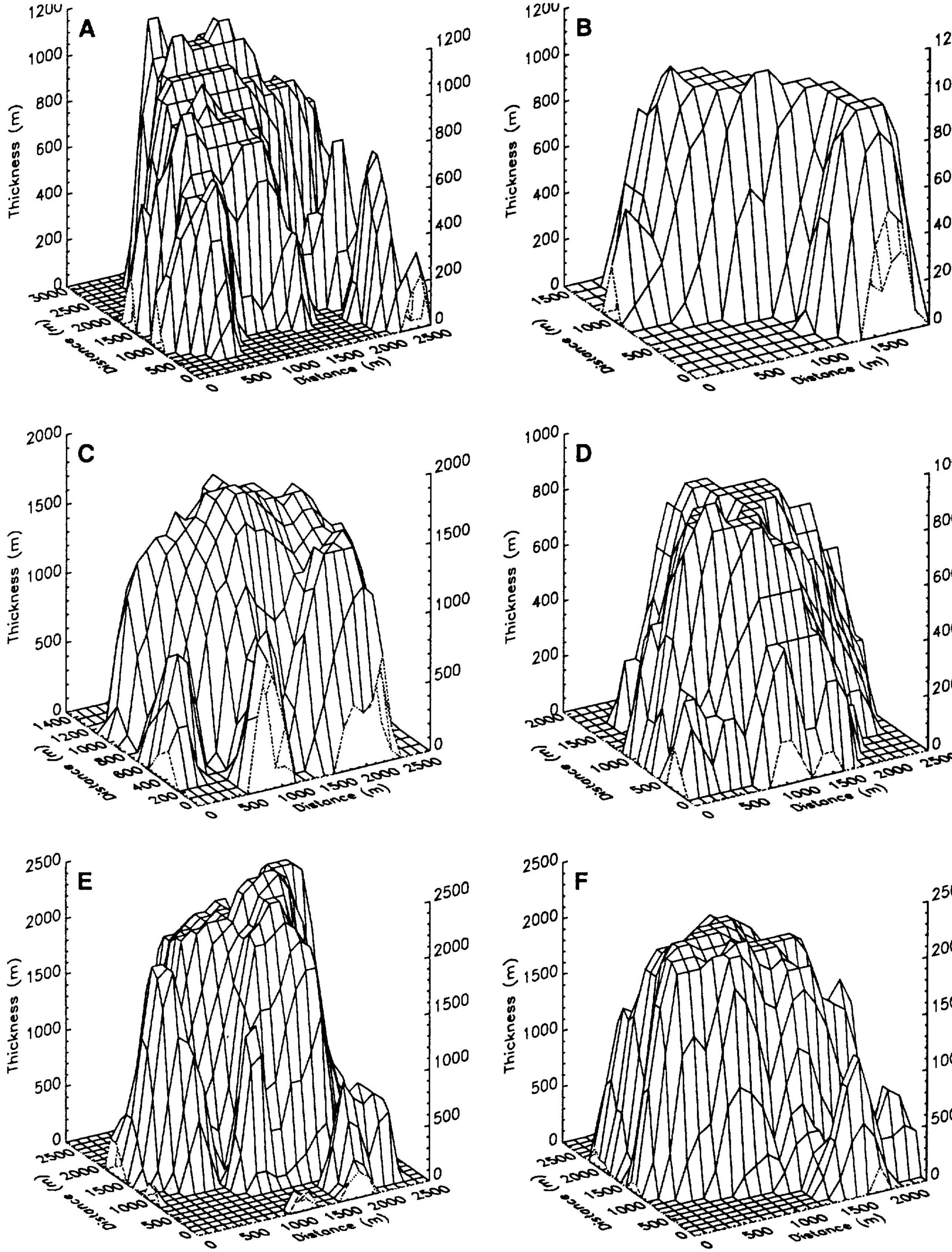

Figure 3: 3-D representations of six unicellular cumulus clouds.

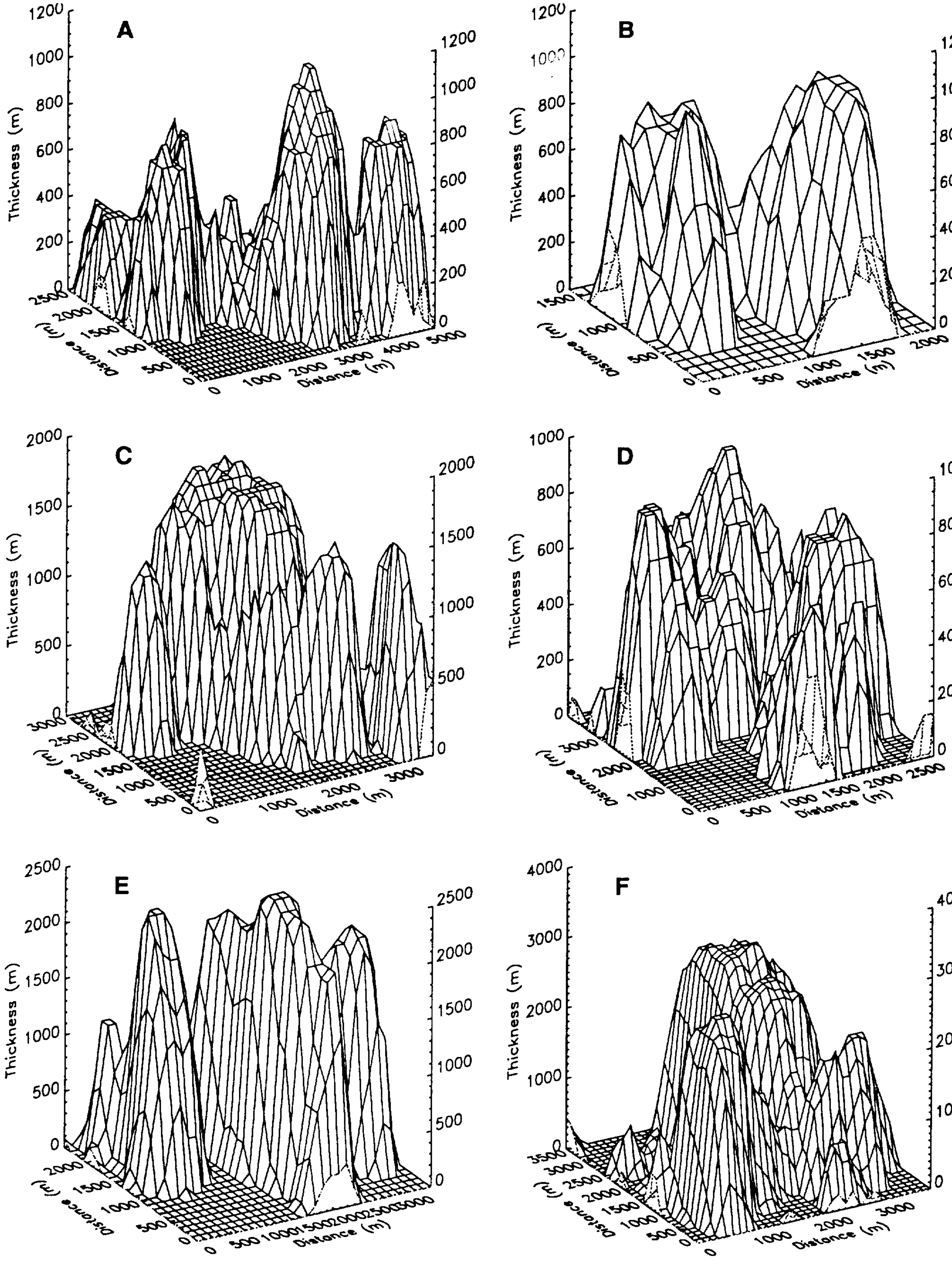

Figure 4: 3-D representations of six multicellular clouds.

as defined by the algorithm. Note in particular that numerous small peaks either do not have sufficient vertical or horizontal extent to be considered as individual cells. Cloud height has been computed assuming the moist adiabatic lapse rate. Figure 4 shows three-dimensional representation of six multicellular cumulus clouds. In each case there are cells that satisfy the criteria for vertical and horizontal extent.

3.4 Shape Analysis

The approximation of the cell's shape is accomplished by supplying the program with the environment lapse rate. Under the assumption of a moist adiabatic lapse rate (6.5 °C/km), a decrease of 0.5 °C in temperature translates to ~77 m increase in height. The brightness temperatures of the pixels in qualified cells are converted to height differences, z. Then the height-weighted centroid is found for the cell. The general equation that describes a quadratic surface has the following form,

$$0 = a_0 + a_1x + a_2y + a_3z + a_4xy + a_5yz + a_6zx + a_7x^2 + a_8y^2 + a_9z^2, \tag{1}$$

where x and y are distances from the centroid in the cross-track and along-track directions respectively. There are several ways that Eq. (1) can be utilized for the least-squares fit. The following is chosen for its consistency in giving good results:

$$1 = c_0x + c_1y + c_2z + c_3xy + c_4yz + c_5zx + c_6x^2 + c_7y^2 + c_8z^2. \tag{2}$$

Eq. (2) is obtained by dividing Eq. (1) by a_0, assuming that a_0 is never 0.

Since the coefficients (c's) are retrieved, Eq. (2) is expressed in the form of Eq. (1) and is transformed to its principal axes. Since the eigenvectors of the following matrix give the directions of the principal axes in the original coordinate system,

$$\begin{matrix} a_7 & a_4/2 & a_6/2 \\ a_4/2 & a_8 & a_5/2 \\ a_6/2 & a_5/2 & a_9 \end{matrix} \tag{3}$$

one can then easily perform the rotational transformation. Once Eq. (1) is rotated into the principal coordinate system, (x', y', z'), the resulting equation has no cross-product terms, x'y', y'z', and z'x':

$$a'_0 + a'_1x' + a'_2y' + a'_3z' + a'_4x'^2 + a'_5y'^2 + a'_6z'^2 = 0. \tag{4}$$

A final translational transformation (by completing the squares) also eliminates the linear terms: x', y', and z'.

The above procedure results in an equation of the following form:

$$\alpha_1u^2 + \alpha_2v^2 + \alpha_3w^2 = 1, \tag{5}$$

where (u, v, ,w) are the transformed coordinates. The shape of the cell is determined by examining the signs of the coefficients, α_1,α_2 and α_3. The equation describes and ellipsoid when all three coefficients are positive. If one coefficient is negative, the equation describes a hyperboloid of one sheet. The equation of hyperboloid of two sheet has two negative the coefficients.

Once the coefficients of Eq. (1) are found, knowing the pixel position, i.e. (x, y), Eq. (1) can be expressed as a quadratic equation of z. The modeled surface can then be found by solving z at all cloudy pixels. Figure 5 shows six examples of the original surface (dashed lines) overlaid on the model surface (solid lines).

4.0 Constraints, Limitations, Assumptions

As mentioned earlier in this document, the environment lapse rate has to be supplied to the program, otherwise the moist adiabatic lapse rate is assumed. Furthermore, the cell recognition method is somewhat primitive.

References

Nakajima, T., M. D. King, J. D. Spinhirne and L. F. Radke, 1991: Determination of the optical thickness and effective particle radius of clouds from reflected solar radiation measurements. Part II: Marine stratocumulus observations. *J. Atmos. Sci.*, 48, 728-750.

Ramanathan, V., 1987: The role of the earth radiation budget studies on climate and general circulation research. *J. Geophys. Res.*, 92, 4075-4095.

—, 1988: The greenhouse theory of climate change: A test by an inadvertent global experiment. *Science*, 240, 293-299.

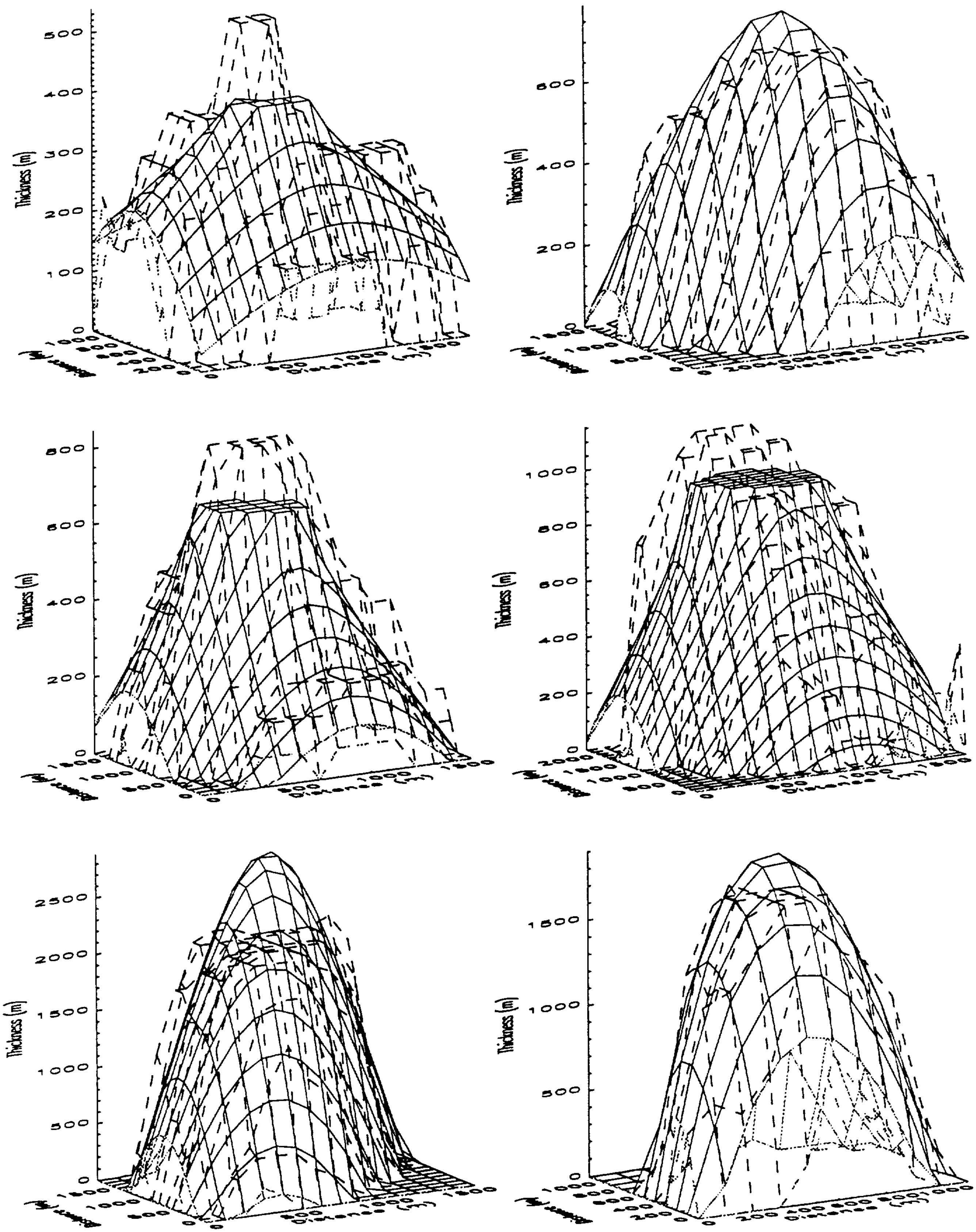

Figure 5: 3-D representations of six modeled cells.

—, and W. Collins, 1991: Thermodynamic regulation of oceanwarming by cirrus cloud deduced from observations of the 1987 El Nino. *Nature*, 351, 27-32.

Roeckner, E., U. Schlese, J. Biercamp and P. Loewe, 1987: Cloud optical depth feedbacks and climate modeling. *Nature*, 329, 138-140.

Rossow, W. B., L. C. Garder, P. J. Lu, and A. Walker, 1991: International Satellite Cloud Climatology Project (ISCCP) documentation of cloud data. *WMO/TD-266*, 76 pp., World Meteorol. Organ., Geneva.

Rossow, W. B. et al., 1985: ISCCP cloud algorithm intercomparison. *J. Clim. Appl. Meteor.*, **24**, 877-903.

—, and L. Parker, 1992: On the determination of cloud cover from satellite sensors: The effect of sensor spatial resolution. *J. Geophys. Res.*, 97, 12799-12823.

REPORT DOCUMENTATION PAGE

Form Approved
OMB No 0704-0188

1. AGENCY USE ONLY (Leave blank)

2. REPORT DATE

3. REPORT TYPE AND DATES COVERED
Semi-annual, 1 Jul 92- 31 Dec 92

4. TITLE AND SUBTITLE
The Effect of Cloud Inhomogeneities Upon Radiative Fluxes, and the Supply of a Cloud Truth Validation Dataset

5. FUNDING NUMBERS
C - NAS5-31718

6. AUTHOR(S)
Ronald M. Welch

7. PERFORMING ORGANIZATION NAME(S) AND ADDRESS(ES)
Institute of Atmospheric Sciences
S.D. School of Mines and Technology
501 E. St. Joseph Street
Rapid City, SD 57701-3995

8. PERFORMING ORGANIZATION REPORT NUMBER
SA-2

9. SPONSORING/MONITORING AGENCY NAME(S) AND ADDRESS(ES)
National Aeronautics and Space Administration
Goddard Space Flight Center
Greenbelt Road
Greenbelt, MD 20771

10. SPONSORING/MONITORING AGENCY REPORT NUMBER

11. SUPPLEMENTARY NOTES

12a. DISTRIBUTION/AVAILABILITY STATEMENT
Unlimited

12b. DISTRIBUTION CODE

13. ABSTRACT (Maximum 200 words)

A series of cloud and sea ice retrieval algorithms are being developed in support of ASTER Science Team objectives. These retrievals include: cloud fractional area, cloud optical thickness, cloud phase (water or ice), cloud particle effective radius, cloud top height, cloud base height, cloud top temperature, cloud emissivity, cloud 3-D structure, cloud field scales of organization, sea ice fractional area, sea ice temperature, sea ice albedo, and sea surface temperature. Due to the problems of accurately retrieving cloud properties over bright surfaces, an advanced cloud classification method has been developed which is based upon spectral and textural features and artificial intelligence classifiers.

14. SUBJECT TERMS
ASTER, cloud product retrievals, sea ice retrievals, expert system

15. NUMBER OF PAGES
104

16. PRICE CODE

17. SECURITY CLASSIFICATION OF REPORT	18. SECURITY CLASSIFICATION OF THIS PAGE	19. SECURITY CLASSIFICATION OF ABSTRACT	20. LIMITATION OF ABSTRACT
Unclassified	Unclassified	Unclassified	